Monte Carlo simulation of intraoperative photodynamic therapy for glioblastoma: investigating dosimetric parameters and treatment efficacy

Louise Ann Finlayson

A thesis submitted for the degree of PhD
at the
University of St Andrews

2024

Candidate's declaration

I, Louise Ann Finlayson, do hereby certify that this thesis, submitted for the degree of PhD, which is approximately 41,000 words in length, has been written by me, and that it is the record of work carried out by me, or principally by myself in collaboration with others as acknowledged, and that it has not been submitted in any previous application for any degree. I confirm that any appendices included in my thesis contain only material permitted by the 'Assessment of Postgraduate Research Students' policy.

I was admitted as a research student at the University of St Andrews in September 2019.

I received funding from an organisation or institution and have acknowledged the funder(s) in the full text of my thesis.

Date   25/7/24   Signature of candidate

Supervisor's declaration

I hereby certify that the candidate has fulfilled the conditions of the Resolution and Regulations appropriate for the degree of PhD in the University of St Andrews and that the candidate is qualified to submit this thesis in application for that degree. I confirm that any appendices included in the thesis contain only material permitted by the 'Assessment of Postgraduate Research Students' policy.

Date   25/7/2024   Signature of supervisor

Permission for publication

In submitting this thesis to the University of St Andrews we understand that we are giving permission for it to be made available for use in accordance with the regulations of the University Library for the time being in force, subject to any copyright vested in the work not being affected thereby. We also understand, unless exempt by an award of an embargo as requested below, that the title and the abstract will be published, and that a copy of the work may be made and supplied to any bona fide library or research worker, that this thesis will be electronically accessible for personal or research use and that the library has the right to migrate this thesis into new electronic forms as required to ensure continued access to the thesis.

I, Louise Ann Finlayson, confirm that my thesis does not contain any third-party material that requires copyright clearance.

The following is an agreed request by candidate and supervisor regarding the publication of this thesis:

Printed copy

No embargo on print copy.

Electronic copy

No embargo on electronic copy.

Date   25/7/24   Signature of candidate

Date   25/7/2024   Signature of supervisor

Underpinning Research Data or Digital Outputs

Candidate's declaration

I, Louise Ann Finlayson, understand that by declaring that I have original research data or digital outputs, I should make every effort in meeting the University's and research funders' requirements on the deposit and sharing of research data or research digital outputs.

Date   25/7/24   Signature of candidate

Permission for publication of underpinning research data or digital outputs

We understand that for any original research data or digital outputs which are deposited, we are giving permission for them to be made available for use in accordance with the requirements of the University and research funders, for the time being in force.

We also understand that the title and the description will be published, and that the underpinning research data or digital outputs will be electronically accessible for use in accordance with the license specified at the point of deposit, unless exempt by award of an embargo as requested below.

The following is an agreed request by candidate and supervisor regarding the publication of underpinning research data or digital outputs:

No embargo on underpinning research data or digital outputs.

Date   25/7/24   Signature of candidate

Date   25/7/2024   Signature of supervisor

Publications, presentations, posters and awards

Publications

1. E. Eadie, P. O'Mahoney, L. Finlayson, I. Barnard, S. H. Ibbotson, K. Wood, Computer Modeling Indicates Dramatically Less DNA Damage from Far-UVC Krypton Chloride Lamps (222 nm) than from Sunlight Exposure, Photochem Photobiol, 97(5), 1150-1154, 2021

2. L. Finlayson, I. Barnard, L. McMillan, E. Eadie, S. H. Ibbotson, C. T. A. Brown, K. Wood, Depth Penetration of Light into Skin as a Function of Wavelength from 200 to 1000 nm, Photochem Photobiol, 98(4), 974-981, 2022

3. L. Finlayson, L. McMillan, S. Suveges, D. Steele, R. Eftimie, D. Trucu, C.Tom A. Brown, E. Eadie, K. Hossain-Ibrahim, K. Wood, Simulating photodynamic therapy for the treatment of glioblastoma using Monte Carlo radiative transport, J. Biomed. Opt. 29(2) 025001, 2024

Presentations

1. L. Finlayson, I. Barnard, L. McMillan, E. Eadie, S. H. Ibbotson, C. T. A. Brown, K. Wood, Simulated Penetration Depth of Ultraviolet Radiation in Skin with Varying Stratum Corneum Thicknesses as an Aid for Phototherapy, Presented at 19th Congress of the European Society for Photobiology, Virtual, Sept 2021

2. L. Finlayson, I. Barnard, L. McMillan, E. Eadie, S. H. Ibbotson, C. T. A. Brown, K. Wood, Production of a Dataset Containing Penetration Depth of Light into Skin from 200–1000 nm, Presented at 2022 Annual Conference of the British Medical Laser Association, Edinburgh, May 2022

3. L. Finlayson, L. McMillan, S. Suveges, D. Steele, R. Eftimie, D. Trucu, T. Brown, E. Eadie, K. Hossain-Ibrahim, K. Wood, Simulation of Intraoperative PDT of Glioblastoma using Monte Carlo Radiative Transport, Presented at 2022 Update PDT-PDD, Nancy, France, October 2022

4. L. Finlayson, L. McMillan, S. Suveges, D. Steele, R. Eftimie, D. Trucu, T. Brown, E. Eadie, K. Hossain-Ibrahim, K. Wood, Simulation of Intraoperative PDT of Glioblastoma using Monte Carlo Radiative Transport, Presented at 2023 Annual Conference of the British Medical Laser Association, Cardiff, May 2023

5. L. Finlayson, L. McMillan, S. Suveges, D. Steele, R. Eftimie, D. Trucu, C. T. A. Brown, E. Eadie, K. Hossain-Ibrahim and K. Wood, Simulation of Intraoperative PDT for Glioblastoma using Monte Carlo Radiative Transport, Talk presented at 18th International Photodynamic Association World Congress, Tampere, Finland, July 2023

Posters

1. L. Finlayson, I. Barnard, L. McMillan, E. Eadie, S. H. Ibbotson, C. T. A. Brown, K. Wood, Light penetration into a 6-layer skin model, Presented at British Association of Dermatologists 101st Annual Meeting, Virtual, July 2021

2. L. Finlayson, I. Barnard, L. McMillan, E. Eadie, S. H. Ibbotson, C. T. A. Brown, K. Wood, Penetration of Light into a 6-Layer Skin Model for 200-1000nm, Presented at SUSSP 76 Photonic Imaging, Sensing & Analysis, June 2021.

3. E. Eadie, P. O'Mahoney, L. Finlayson, S. H. Ibbotson, K. Wood, Characterising 'Far-UVC' KrCl excimer lamps for safety and inactivation of viruses, Presented at 19th Congress of the European Society for Photobiology, Virtual, Sep 2021

4. L. Finlayson, L. McMillan, S. Suveges, D. Steele, R. Eftimie, D. Trucu, T. Brown, E. Eadie, K. Hossain-Ibrahim, K. Wood, Simulation of Intraoperative PDT of Glioblastoma using Monte Carlo Radiative Transport, Presented at CDTAP Conference, June 2022

5. L. Finlayson, L. McMillan, S. Suveges, D. Steele, R. Eftimie, D. Trucu, T. Brown, E. Eadie, K. Hossain-Ibrahim, K. Wood, Simulation of Intraoperative PDT of Glioblastoma using Monte Carlo Radiative Transport, Presented (via proxy) at Inaugural Collaborative Research and Innovation Symposium, Glenrothes, October 2022

6. L. Finlayson, L. McMillan, S. Suveges, D. Steele, R. Eftimie, D. Trucu, T. Brown, E. Eadie, K. Hossain-Ibrahim, K. Wood, Killing Cancer with Light: Simulation and Optimisation of Photodynamic Therapy for Glioblastoma, presented at the STEM for Britain finals, House of Commons, London, March 2023

Awards

1. L. Finlayson, L. McMillan, S. Suveges, D. Steele, R. Eftimie, D. Trucu, T. Brown, E. Eadie, K. Hossain-Ibrahim, K. Wood, Simulation of Intraoperative PDT of Glioblastoma using Monte Carlo Radiative Transport, Presented (via proxy) at Inaugural Collaborative Research and Innovation Symposium, Glenrothes, October 2022.

   Category: 'Best Poster, Clinical Research'

Abstract

This thesis looks at using Monte Carlo radiative transfer (MCRT) to simulate the path and effect of light as it travels through biological tissue.

The increase in light-based skin treatments and medical technology has resulted in a need for detailed information on the penetration depth of light into skin. A 6-layer skin model is developed to simulate the propagation of light from 200 nm - 1000 nm into skin with Fitzpatrick photo-type I. The effect of varying stratum corneum thickness and light incident angle is investigated before looking at the lateral spread of a laser beam incident on the skins surface.

Photodynamic therapy (PDT) is a light based therapy currently used or being investigated to treat many different forms of cancer. The combination of treatment light, a photosensitising drug and oxygen result in a localised toxic effect that specifically targets cancer cells. The MCRT code is used to develop a time dependant simulation of PDT, considering the treatment light fluence rate and local concentrations of photosensitiser and oxygen. This allows different PDT protocols to be simulated and compared.

Glioblastoma (GBM) is an aggressive and difficult to treat form of brain tumour. It has a low survival rate due to the tumours highly diffusive nature, resulting in a high rate of recurrence. A recent clinical trial aimed to increase this survival time by intraoperatively treating the resection cavity with PDT at the end of resection surgery to increase the extent of resection. The MCRT/PDT simulation is used to model this protocol and investigate the effect on tumour cell kill when varying several treatment parameters such as treatment time, light power and photosensitiser concentration. Finally, a heat transport simulation is also used to investigate the effect of intraoperative PDT treatment on the temperature of the surrounding brain tissues.

Acknowledgements

First and foremost, every piece of work within this thesis would not have been possible without my supervisors Kenny Wood, Ewan Eadie, Kismet Hossain-Ibrahim and Tom Brown. Thank you for all your time, encouragement and support. I have immensely enjoyed learning from you all and you have made working on this PhD a genuine pleasure.

Thank you to Lewis and Isla for your collaboration and help finding my feet with the MCRT code. An extra thanks to Lewis who was always happy to answer my questions and help when the code just wouldn't work!

Thank you to the team at Ninewells for your office and conference company, and for letting me observe how PDT happens in the non-simulated world.

Thank you to the INDYGO team for your time and feedback on the work simulating your trial protocol. An extra thanks to Clément for patiently answering any questions I had.

Thank you to the CDTAP team for all the support and learning opportunities you have organised. Thanks also to my CDT cohort for providing much needed peer support. Special thanks to Alex for your friendship and check-ins that got us through some stressful deadlines and exams!

Thank you to my diving friends for all the weekend dive trips and socials that got my head out of work and kept me sane.

Thank you to Nathan for all of your coursework help and words of encouragement which have kept my head above the water these last few months. Also thank you for your typo finding skills and for agreeing to read over this thesis!

Thank you to Torsten for always being there, letting me bounce ideas off of you and putting up with me through the highs and lows of the past 4 years. Thank you for all of your company, cooking, cups of tea, homemade cakes and for generally keeping me sane throughout all of the covid lock-downs and social isolations. You made a difficult time a lot less difficult.

Finally, thank you to my family; Mum, Ash, Sonya, Natasha, Philip and Ella. Thank you for being a constant source of support and love and for reminding me of what's really important in life.

Funding

Research Data / Digital Outputs

Final versions of all codes developed as part of this thesis can be found at `https://gitlab.com/Loufin101`

Research data for chapter 2 can be found at : `https://doi.org/10.5281/zenodo.10644181`
Research data for chapter 3 can be found at : `https://doi.org/10.5281/zenodo.10646328`
Research data for chapter 4 can be found at : `https://doi.org/10.5281/zenodo.10646375`
Research data for chapter 5 can be found at : `https://doi.org/10.5281/zenodo.10646476`

Contents

Acronyms

5-ALA 5-Aminolevulinic Acid.

BBB Blood Brain Barrier.

CDF Cumulative Distribution Function.

CNS Central Nervous System.

CPD Cyclobutane Pyrimidine Dimers.

DOSINDYGO DOSe finding for INtraoperative photoDYnamic therapy of GliOblastoma.

DRS Diffuse Reflectance Spectroscopy.

FDM Finite Difference Method.

FECH Ferrochelatase.

FEM Finite Element Method.

FGS Fluorescence-Guided Surgery.

GBM Glioblastoma.

GSC Glioma Stem Cells.

HpD Hematoporphyrin Derivative.

INDYGO INtraoperative photoDYnamic therapy for GliOblastoma.

IR Infrared.

MCRT Monte Carlo Radiative Transfer.

NIR Near Infrared.

PD Photodynamic Dose.

PDF Probability Density Function.

PDT Photodynamic Therapy.

PpIX Protoporphyrin IX.

PS Photosensitiser.

ROS Reactive Oxygen Species.

RTE Radiative Transfer Equation.

UV Ultra Violet.

Glossary

A Area (cm^2).

C Photosensitiser concentration (μg/ml).

D Photobleaching dose constant (Jcm^{-2}).

E Energy (J).

F_{mel} Melanin fraction.

L Irradiance (Wcm^{-2}sr^{-1}.

P Power (W).

Q Energy absorbed (Jcm^{-3}).

R Fraction of light reflected.

R_c Capillary radius (μm).

R_d Fraction of light reflected.

R_t Radius of Krogh tissue cylinder (Half the distance between two capillaries) (μm).

T Fraction of light transmitted through a distance z.

T Temperature (K).

T_d Fraction of light transmitted through a distance z.

V Volume (cm^{-3}).

$[^1O_2]_{rx}$ Apparent reacted singlet oxygen concentration (μM).

Γ Photobleaching time constant (s).

Ω Solid angle (sr).

Φ Fluorescence quantum yield.

Φ_0 Maximum rate of oxygen perfusion (μMs^{-1}).

β Ratio of rate of decay of photosensitiser triplet state and rate of triplet state photosensitiser quenching by $^1O_2$ (μM).

δ Low oxygen concentration correction (μM).

ϵ Excitation coefficient ($\text{cm}^{-1}(\mu\text{g/ml})^{-1}$).

$\hat{s}$ Direction vector.

κ Thermal conductivity ($\text{Wm}^{-1}\text{K}^{-1}$).

λ Wavelength (nm).

μ_a Absorption coefficient (cm^{-1}).

μ_s Scattering coefficient (cm^{-1}).

μ_t Extinction coefficient $= \mu_a + \mu_s$ (cm^{-1}).

ν Frequency (Hz).

ϕ Azimuthal angle.

ψ Fluence rate.

ρ Density (kgm^{-3}).

σ Ratio of rate of $^1O_2$ reaction with ground state photosensitiser and rate of $^1O_2$ reaction with biological substrate, multiplied with concentration of biological substrate (μM^{-1}).

τ Optical depth (cm).

θ Polar angle.

υ_z Blood flow velocity (μms^{-1}).

ϱ Ratio of proportional constant between photochemical oxygen consumption rate and fluence rate and photosensitiser concentration ($\text{cm}^2\text{mW}^{-1}\text{s}^{-1}$).

ξ Random number.

ζ Phase function.

ζ_θ Probability density function of the scattering angles of light at a scattering location.

c Speed of light within a vacuum (ms^{-1}).

c_p Specific heat capacity (JK^{-1}).

f Collection efficiency.

g Anisotropy coefficient.

h Plancks constant (JHz^{-1}).

l_z Length of capillary (μm).

n refractive index.

q_0 Maximum metabolic consumption rate (μMs^{-1}).

$^3O_2$ Triplet oxygen concentration (μM).

List of Figures

List of Tables

Chapter 1

Introduction

1.1 Thesis motivation

As medicine and medical sciences evolve, the motivation and need to use computers and computational techniques as research, planning and treatment aids has increased significantly[1, 2]. By providing detailed and precise simulations of radiation transport and interactions within biological tissue, Monte Carlo radiative transfer (MCRT) simulations are a prime example of how modern technology can be used to gain valuable insights that would otherwise have been impossible. The main focus of this thesis is to use MCRT simulations to simulate the distribution of light into the brain for the treatment of glioblastoma tumours via Photodynamic Therapy (PDT).

PDT uses a combination of light, oxygen and a photosensitising drug to target and kill diseased tissue. Currently, the majority of conditions that PDT is used to treat clinically are in skin[3]. However as the use of PDT expands into more areas such as neurosurgery, being able to plan and deliver optimal, precise and accurate treatment is paramount to ensuring eloquent brain tissue is not damaged during the treatment. MCRT simulations can provide the level of accuracy needed and have the potential to empower clinicians with a tool that can plan treatments for different tissues and body sites with the optimal level of efficacy and safety. Simulations could also be used pre-clinical trial to test and refine treatments before any permissions or test subjects are needed, saving time and money and ultimately making trials safer for patients.

MCRT has already been used for treatment planning and dose finding in several areas such as phototherapy, nuclear medicine (eg. PET imaging) and radiographic imaging (eg. x-ray investigations)[4, 5, 6]. It has also been used many times to model PDT. Some examples are simulations of standard and daylight PDT with 5-ALA for skin cancer[7, 8], and simulations of interstitial PDT treatment for gliomas[9, 10].

It's becoming clear that medicine is heading in a direction where, to provide the best care possible, treatments are expected to be targeted and fully personalised to the patient[2, 11] and this is a goal that MCRT is well suited for. Patient scans could be used to provide MCRT models that incorporate their unique geometries and optical properties, allowing a fully tailored simulation and treatment plan to be produced.

This thesis looks at developing an MCRT code to simulate light transport within tissue for two clinical applications. The first application was to look at the penetration depth of light into skin over a wide wavelength range and to present these data in a way that is both accessible and easily applicable to a specific scenario or light source. The second application was to use MCRT to simulate intraoperative PDT for the treatment of glioblastoma brain tumours. It is hoped that this work forms an initial step towards developing a treatment planning system to align with the goals discussed above

1.2   Light propagation into tissue

1.2.1   Electromagnetic spectrum

The light used in photo-treatments forms a small section of the electromagnetic spectrum (see figure 1.1). The wavelengths used within this thesis are displayed in more detail in figure 1.1. They are within the range 200 nm (Ultra violet radiation (UV)) to 1000 nm (Near infrared radiation (NIR)).

Ultraviolet radiation

Ultra violet (UV) radiation is all of the electromagnetic radiation within the range 100 nm - 400 nm. It can be further broken down into three separate bands UVC (100 nm - 280 nm), UVB (280 nm - 315 nm) and UVA (315 nm - 400 nm).

With the shortest wavelength, UVC radiation has the highest level of energy. However, due to it's high absorption rate in the atmosphere and resultant low levels of natural occurrence, the risk to health is low[12]. This high level of energy but low risk factor makes UVC especially useful for germicidal purposes such as lowering the risk of airborne viruses and effectively killing surface bacteria[13, 14].

Although UVB and UVA radiation have less energy than UVC, they are considered more harmful due to their ability to penetrate further into materials and tissue such as skin. UVB and UVA radiation can interact with the DNA in the basal layer, causing changes to occur. Large numbers of these interactions caused by high UV exposure can lead to mutations and cancer forming[15]. When exposed to UV radiation, DNA produces photo-products called
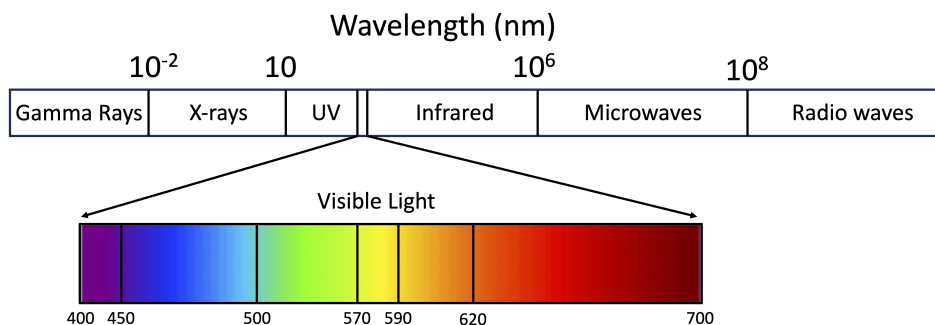
Figure 1.1: The wavelength ranges in nanometres (nm) of different radiation groups within the electromagnetic spectrum. Wavelengths within range of 200 nm - 1000 nm are of interest within the field of photo medicine and photo protection.

cyclobutane pyrimidine dimers (CPDs) which can be used to quantify damage level. As it is more energetic, UVB radiation generally causes CPDs to be produced at a larger rate than UVA, indicating more damage[16]. However, UV radiation can also benefit health by using it for purposes such as treating various skin conditions and skin cancer and reducing symptoms of multiple sclerosis (MS)[17].

Visible light

The visible light spectrum ranges from around 400 nm to 700 nm, going from blue light to red. As these wavelengths are longer, visible light has less energy than UV, making exposure to it less harmful, but it is able to penetrate more deeply into tissue.

Although less energetic than UV radiation, visible light is heavily used in the medical and cosmetic fields for several areas from imaging and diagnosis to therapy and surgery. There are a range of mechanisms that can take place when using visible light for medical treatment, and these depend both on the power and wavelength of the light and can include photothermal, photochemical and photomechanical processes[18].

Near infrared radiation

Near infrared radiation (NIR) has a wavelength range of around 700 nm - 1800 nm. A lot of therapies using NIR are still in the development stage, with mixed results in treatments such as photobiomodulation and thermal neuromodulation. Nd:YAG lasers with 1064 nm wavelengths have been used with some success for photothermal therapy, for example in the removal of deeper port wine stains[19]. Due to its deeper tissue penetration depth, NIR has a lot of potential in the field of PDT and so developing compatible photosensitisers is a current area of research[18].

1.2.2 Optical properties

The optical properties of a medium form the foundation of radiation-matter interaction modelling. The main properties that are used to describe the path of light through a medium are the absorption (μ_a), scattering (μ_s) and anisotropy coefficients (g), as well as the refractive index (n).

Absorption

The absorption coefficient $(\mu_a)(\mathrm{m}^{-1})$ describes the probability of energy absorption within a medium per unit distance of the path-length (z) that light travels within it[20]. Equation 1.1 describes the fraction of light transmitted (T) when the light travels a distance z though a medium with absorption coefficient μ_a.

$$T = e^{-\mu_a z} \tag{1.1}$$

The level of absorption within a tissue is dependent on the chromophores present. The main chromophores present in tissue, for example, are haemoglobin, water, melanin,lipids and collagen[21, 22], with their absorption contribution levels dependent on their concentration as well as the wavelength of light.

Scattering

The scattering coefficient $(\mu_s)(m^{-1})$ describes the probability of a photon interacting with the medium in a way that causes a change in its direction of travel. Scattering within a medium can be caused by changes to the refractive index[20]. Biological tissue causes light to scatter as it is a complex, heterogeneous medium made from cells which contain many elements with different refractive incidences[22]. Similar to the absorption coefficient, the fraction of light travelling a distance z into a medium with scattering coefficient μ_s is described by equation 1.2.

$$T = e^{-\mu_s z} \tag{1.2}$$

Often the reduced scattering coefficient, defined as:

$$\mu'_s = \mu_s(1 - g) \tag{1.3}$$

is given in literature due to the fact that it is simpler to measure[20]. Here g is the anisotropy factor discussed below.

Anisotropy

The anisotropy coefficient (g) is defined as the average of $\cos\theta$, where θ is the angle between the direction of initial travel of a photon and the direction after it is scattered (equation 1.4).

$$g = \langle\cos\theta\rangle \tag{1.4}$$

The value of g can range from -1 to 1 depending on the dominant scattering direction. A value of $g = 0$ corresponds to isotropic scattering (or scattering that is forward-backward symmetric) while $g = -1$ and $g = 1$ correspond to complete backward and forward scattering respectively[23].

The value of g can be modelled within biological tissue using a phase function (ζ_θ) defined as the probability density function of the scattering angles of light at a scattering location[24].

Measurement methods

The measurement of tissue optical properties can be done via different methods, each with their own advantages and disadvantages. Ex vivo measurements can be done either directly or indirectly. Direct methods, such as the measurement of collimated light transmission through a thin slab of tissue are combined with double or single-integrating sphere measurements in many studies[25, 26]. Optical properties, such as μ_a, μ_s and g discussed above, can be obtained from these measurements with the use of simple analytic expressions and rules such as the Bouguer-Beer-Lambert law (equation 1.1) and the single scattering phase function. However, to obtain accurate properties using these simple expressions, great care needs to be taken to produce specific experimental conditions such as making the tissue sample thin enough to allow only single scattering to take place. Other factors such how the samples are prepared (how they are sliced and mounted), their water content and the potentially significant light loss during the measurement can also affect the validity of the optical properties measured this way[26].

Indirect methods offer the advantage of being able to obtain optical properties from thicker

samples. Theoretical models of light propagation through a material are used to deduce optical properties from diffuse reflection, diffuse transmission, total reflection, total transmission and collimated transmission measurements. These include the Kubelka-Munk model, inverse adding and doubling and inverse Monte Carlo methods[26, 27]. An alternative to measuring the optical properties is to model them mathematically instead. Generally, these methods predict the optical properties using the base level scattering and absorption properties inherent to the biological content of the tissue[20].

While *in vitro* measurement techniques do have the advantage of being able to measure individual components of a tissue separately (eg. skin layers), the results can be heavily affected by the sample preparation technique, causing artificial variability in the results. In vivo measurement techniques might therefore provide more accurate results[25]. An example of an *in vivo* measurement method is diffuse reflectance spectroscopy (DRS). While integrating sphere methods use light transmitted through a sample to determine its optical properties, Diffuse Reflectance Spectroscopy (DRS) uses light that has been reflected, making *in vivo* measurements possible[28, 26].

Kubelka-Munk model

To obtain absorption and scattering coefficients from transmission T_d and reflection R_d measurements using the Kubelka-Munk model, the absorption and scattering parameters K and S are first calculated using equations 1.5 and 1.6 where d is the thickness of the sample[27].

$$S = \frac{1}{bd}ln[\frac{1 - R_d(a - b)}{T_d}]$$ (1.5)

$$K = S(a - 1)$$ (1.6)

a and b are given by equations 1.7 and 1.8.

$$a = \frac{1 - T_d^2 + R_d^2}{2R_d}$$ (1.7)

$$b = \sqrt{a^2 - 1}$$ (1.8)

To obtain the scattering and absorption coefficients, equations 1.9 and 1.10 can be used where g is the anisotropy factor and the values for coefficients η and χ are presented by Klier et al.[29] as a function of $\frac{K}{S}$.

$$\mu_a = \eta K$$ (1.9)

$$\mu_s(1 - g) = \chi S$$ (1.10)
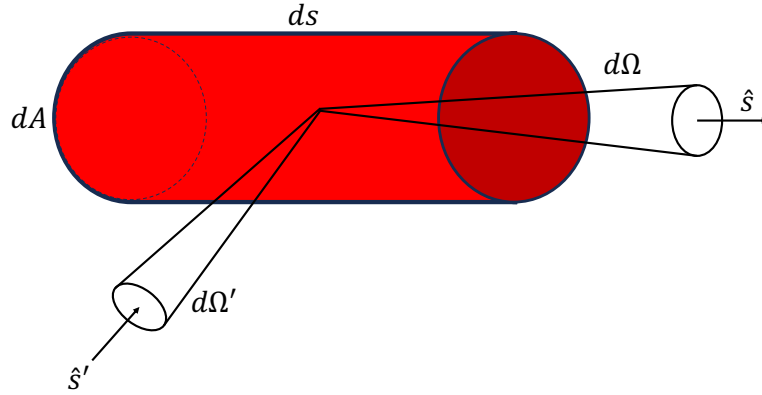
Figure 1.2: Diagram of a cylindrical volume element with volume $dsdA$ that is used to derive the RTE by modelling the energy flowing through it through solid angles $d\Omega'$ and $d\Omega$ in directions $\hat{s}'$ and $\hat{s}$ respectively.

1.2.3   Radiative transfer equation

The Radiative Transfer Equation (RTE) can be used to model the propagation of electromagnetic radiation such as light through turbid media such as biological tissue. It is derived using the principles of energy conservation when looking at the flow of energy through a stationary cylindrical volume element, shown in figure 1.2[30].

The energy conservation equation (equation 1.11) forms the basis of the derivation where dP is the net change in energy per unit time within the cylinder, dP_{src} is the energy produced by the radiation source, dP_{sca} is the energy incident on the cylinder due to scattering from other directions, dP_{div} is the energy loss due to photon beam divergence and dP_{ext} is the energy loss from photon absorption and scattering.

$$dP = dP_{\mathrm{src}} + dP_{\mathrm{sca}} - dP_{\mathrm{div}} - dP_{\mathrm{ext}} \tag{1.11}$$

Each of the elements from equation 1.11 are now discussed in more detail before pulling them together to derive the full RTE.

dP

dP is the net change in energy per unit time within the cylindrical volume element and is described using equation 1.12.
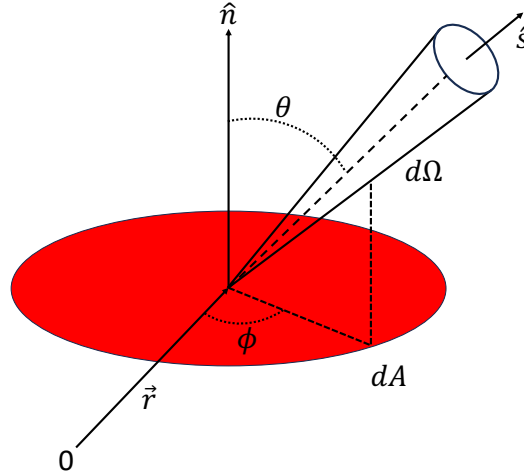
Figure 1.3: Diagram showing the flow of energy through an area dA within solid angle $d\Omega$ and in the direction $\hat{s}$.

$$dP = \frac{1}{c}\frac{\partial L(\vec{r}, \hat{s}, t)}{\partial t}dV d\Omega \tag{1.12}$$

Here, c is the speed of light, V is the cylinder volume and L is the irradiance, defined as the spectral irradiance (L_v) over the small frequency range of $[v, v + \Delta v]$. Spectral irradiance is the energy flow at position $\vec{r}$, in the $\hat{s}$ direction per unit normal area (A), per unit solid angle $(d\Omega)$, per unit time (t), per unit frequency bandwidth (Δv). L can be described by equation 1.13.

$$L(\vec{r}, \hat{s}, t) = L_v(\vec{r}, \hat{s}, t)\Delta v \tag{1.13}$$

The units of L are $\text{Wm}^{-2}\text{sr}^{-1}$. Generally, when solving the RTE, the main goal is to obtain the irradiance which can be used to calculate both the energy (dE) flowing across an area dA within solid angle $d\Omega$ and time dt (figure 1.3), and the fluence rate ψ.

dE (J) is calculated using equation 1.14 where $\cos\theta$ is the angle between $\hat{n}$, the unit normal to area dA and $\hat{s}$, the direction of energy flow.

$$dE = L(\vec{r}, \hat{s}, t) \cdot \cos\theta dAd\Omega dt \tag{1.14}$$

The fluence rate ψ (Wm^{-2}) is defined as the energy flow per unit area, per unit time, independent of direction and is calculated using equation 1.15.

$$\psi(\vec{r}, t) = \int_{4\pi} L(\vec{r}, \hat{s}, t) d\Omega \tag{1.15}$$

$\mathbf{dP_{src}}$

The first of two contributions to the energy flowing through the cylinder is the energy produced by the source (dP_{src}) per unit time. This is described by equation 1.16 where $S(\vec{r}, \hat{s}, t)$ ($\mathrm{Wm^{-3}sr^{-1}}$) is the source emission in the cylinder within the solid angle $d\Omega$.

$$dP_{src} = S(\vec{r}, \hat{s}, t)dV\, d\Omega \tag{1.16}$$

$\mathbf{dP_{sca}}$

The second contribution to the energy (P_{sca}) is due to scattering within the solid angle $d\Omega$ from any direction $\hat{s}'$ to direction $\hat{s}$. This is described by equation 1.17 where N_s ($\mathrm{m^{-3}}$) is the number density of scatterers, $\zeta(\hat{s}', \hat{s})$ is the scattering phase function (section 1.2.2), σ_s ($\mathrm{m^2}$) is the scattering cross section and μ_s ($\mathrm{m^{-1}}$) is the scattering coefficient ($\mu_s = N_s\sigma_s$).

$$dP_{sca} = N_s dV \left(\int_{4\pi} L(\vec{r}, \hat{s}, t)\zeta(\hat{s}', \hat{s})\sigma_s d\Omega' \right) d\Omega = \mu_s dV \left(\int_{4\pi} L(\vec{r}, \hat{s}, t)\zeta(\hat{s}', \hat{s})d\Omega' \right) d\Omega \tag{1.17}$$

$\mathbf{dP_{div}}$

The energy loss from the cylindrical volume element due to radiation beam divergence (P_{div}) is the first of two energy loss term and is described by equation 1.18.

$$dP_{div} = \frac{\partial L(\vec{r}, \hat{s}, t)}{\partial s}d\Omega dV \tag{1.18}$$

$\mathbf{dP_{ext}}$

Finally, the second loss term P_{ext} is the energy loss within solid angle $d\Omega$ due to scattering and absorption. This is described using equation 1.19 where μ_t ($\mathrm{m^{-1}}$) is the extinction coefficient defined as the sum of the scattering and absorption coefficients ($\mu_t = \mu_a + \mu_s$).

$$dP_{ext} = \mu_t ds L(\vec{r}, \hat{s}, t)dA d\Omega \tag{1.19}$$

RTE

The final RTE is obtained by replacing each term in equation 1.11 with the relevant term defined above. This yields equation 1.20.

$$\underbrace{\frac{1}{c}\frac{\partial L(\vec{r},\hat{s},t)}{\partial t}}_{dP} = \underbrace{S(\vec{r},\hat{s},t)}_{dP_{\text{src}}} + \underbrace{\mu_s\int_{4\pi}L(\vec{r},\hat{s}',t)\zeta(\hat{s}',\hat{s})d\Omega'}_{dP_{\text{sca}}} - \underbrace{\mu_t L(\vec{r},\hat{s},t)}_{dP_{\text{ext}}} - \underbrace{\frac{\partial L(\vec{r},\hat{s}',t)}{\partial s}}_{dP_{\text{div}}} \quad (1.20)$$

1.2.4   Solving the RTE

The RTE is difficult to solve analytically, especially in 3D heterogeneous, highly scattering mediums. These cause each photon to have multiple interactions with the tissue, each with variable outcomes, resulting in a very complex set of equations needed to model them accurately. Approximations or numerical methods can be used instead. A few of these are discussed in the sections below.

Diffusion Approximation

The diffusion approximation can be used to solve the RTE within a medium where scattering is dominant over absorption. The approximation uses the first two terms of the Legendre polynomial expansion to describe the phase function $\zeta(\hat{s}',\hat{s})$ within the RTE. While this is a simple and convenient way to describe light transport within tissue, several assumptions within the approximation make it unsuitable for every circumstance. If the medium does not have negligible absorption for example, the approximation will underestimate the calculated fluence rate. The boundary and surface fluence rates are also underestimated, making the approximation unsuitable for many models such as those simulating photodynamic therapy (see chapter 4), where accurate modelling light interactions at or near the surface is very important[31]. The diffuse approximation also struggle's to accurately model sharp gradients in fluence rate, such as from a point source within the medium or variations in the absorption and scattering coefficients, making it only suitable for homogeneous mediums.

MCRT

The Monte Carlo Radiative Transfer (MCRT) method numerically solves the RTE through simulation. It uses the probabilistic nature of photon interactions with matter to follow the path of photons, grouped into 'power packets', through the medium. Interaction events (scattering or absorption) are tracked and the power packets path ends either when it has been absorbed or when it leaves the simulation region. This is repeated for many power packets and, provided the optical properties entered for the medium are correct, an accurate description of the light or energy distribution in the region is built. MCRT can model both absorption and scattering (isotropic and anisotropic) in the same simulation and can also include numerous materials with varying properties such as a tumour which makes it convenient for modelling PDT. Although it is computationally expensive, this

problem is being alleviated with solutions such as computer parallelising and mesh grid systems[32, 33]. MCRT is discussed in more detail in section 1.4.

1.3 Random number sampling

One of the main concepts of MCRT is the use of random sampling of Probability Density Functions (PDF) to realistically model an overall fluence rate based on the results of many complex photon interactions with many possible outcomes. For example, when modelling the random walk of a power packet through a medium, every decision such as the distance travelled before interacting, the type of interaction that occurs (absorption or scattering) and the direction of travel after scattering is made by randomly sampling a unique PDF for each process. The two types of random sampling used within this work are the inverse transform method and the rejection method, discussed in more detail below.

1.3.1 Random number generation

For random sampling to be possible, random numbers must be generated. Many computing languages, including FORTRAN 90, have inbuilt random number generators that, when called upon, generate a number within the range 0 to 1. However, due to the fact that computers can only work by following set algorithms, a computer generated random number can never be truly random. Instead, computers algorithmically produce pseudo-random numbers from a seed number given within the code. Long lists of numbers are produced which makes it possible to run full simulations without repetition[34]. To make code debugging easier, the code within this work used the random number generator (ran2) described in *Numerical Recipes*[35], which allows the initial starting seed to be chosen, allowing results to be fully predictable if needed.

1.3.2 Inverse transform method

PDFs are functions ($f(x)$) that define the probability of a variable being equal to a given value (x). The inverse transform sampling method is used to sample PDFs to obtain random values for different variables. To use inverse transform sampling, the cumulative distribution function (CDF) of the PDF needs to be obtained. If a PDF has possible x values in the range $[x_{min}, x_{max}]$, then the CDF is the probability of the value being less than or equal to a specific value x, or:

$$CDF(x) = \int_{x'_{min}}^{x} f(x')dx' \tag{1.21}$$

where the function $f(x)$ is normalised within the range $[x_{min}, x_{max}]$. When sampling from a continuous distribution, the inverse transform method starts by setting the CDF, evaluated
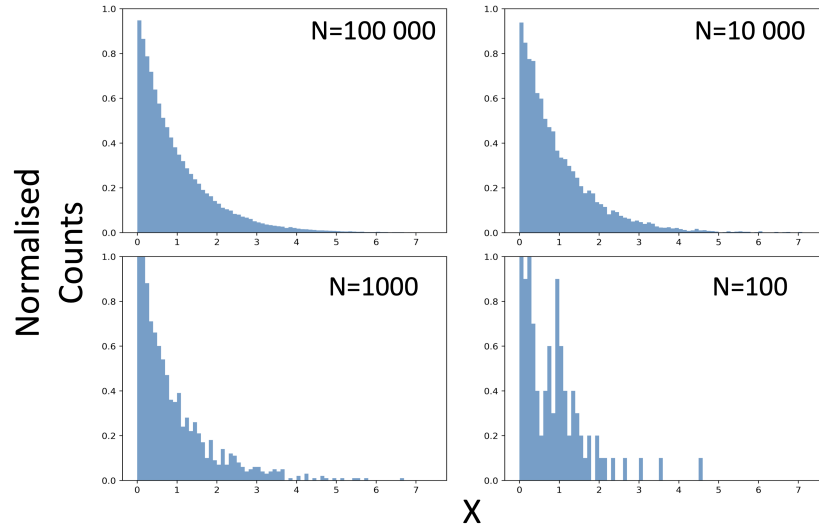
Figure 1.4: Histograms showing the number of each X value obtained when sampling the function e^{-X} using the inverse transform sampling method. The plots show the resulting histograms when taking 100,000, 10,000, 1000 and 100 random samples. We can see that the function is more accurately reproduced as the number of samples increases.

at a sample value X (denoted $F(X)$), equal to a generated random number (ξ) between 0 and 1. $F(X)$ is inverted to obtain the sample value X as shown in equation 1.22.

$$\xi = F(X) \Rightarrow X = F^{-1}(\xi) \tag{1.22}$$

If enough random samples are taken, then plotting them should reproduce the PDF as demonstrated in figure 1.4 where the function $f(X) = e^{-X}$ is sampled.

1.3.3 Rejection method

In cases where a PDF doesn't exist or the CDF cannot be inverted, the rejection method can be used instead. This starts by producing a random number ξ between 0 and 1 and assigning values obtained within a specific range to each possible outcome of the process that is being sampled. For example, if the process being sampled only has two possible outcomes, with outcome 1 occurring with a probability of 90 % and outcome 2 a probability of 10 %, using the rejection method, the outcome will be chosen as shown in equation 1.23.

$$\text{outcome} = \begin{cases} 1 & \text{if } 0 < \xi \leq 0.9 \\ 2 & \text{if } \xi > 0.9 \end{cases} \tag{1.23}$$

Within this works MCRT simulation, the rejection method is used when choosing between an absorption or scattering event.

1.4 MCRT

Background and history

The first instance of the Monte Carlo method is believed to be in the 18th century when french scientist Georges Louis LeClerc, Comte de Buffon estimated the probability of a needle landing on a gap between two floorboards in an experiment now named 'Buffons needles'. The experiment assumes that all floor boards are the same width (W) and are wider than the length of the needles (l). If several needles are thrown randomly onto the floor boards as shown in figure 1.5, the probability of a needle crossing a gap between two floorboards (indicated by the green needles) can be calculated.
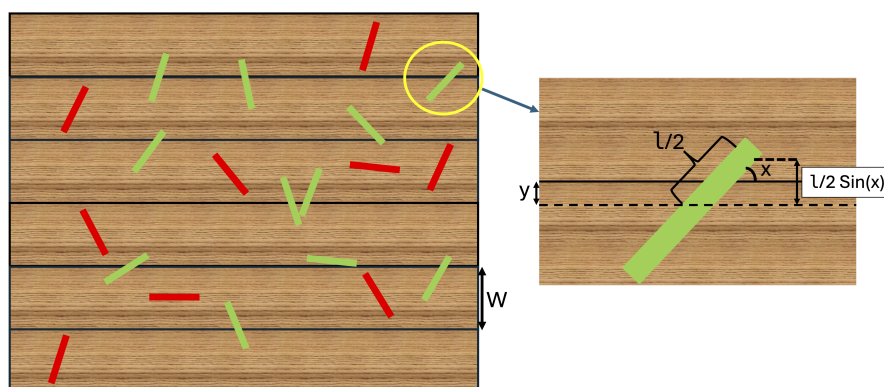
Figure 1.5: Image depicting Buffons needles experiment. The green lines indicate the needles that land on a gap in the floorboards while the red lines indicate needles that land between the gaps. The subplot on the right hand side shows how the conclusion that a needle will cross a gap if $y < \frac{l}{2} \sin x$ is derived.

From figure 1.5 we can see that a needle will cross the gap if:

$$y < \frac{l}{2} \sin x \tag{1.24}$$

Here y can be anywhere within the range $[0, \frac{W}{2}]$ and x can be anywhere in the range $[0, \frac{\pi}{2}]$, giving them PDFs of $\frac{2}{W}$ and $\frac{2}{\pi}$ respectively. This means the probability of obtaining a

specific value of x and y is:

$$p(y,x) = \frac{4}{W\pi} \tag{1.25}$$

The probability of a thrown needle crossing a gap is:

$$P = \frac{H}{N_{\text{needles}}} = \int_0^{\frac{\pi}{2}} \int_0^{\frac{l}{2}\sin x} \frac{4}{W\pi} dy dx = \frac{2l}{W\pi} \tag{1.26}$$

where H is the number of needles crossing a gap and $N_{needles}$ the total number of needles thrown[36]. This can be rearranged to estimate π.

$$\pi = \frac{2l N_{\text{needles}}}{WH} \tag{1.27}$$

We can see that as more needles are thrown, the accuracy of the estimation of π increases[37].

A modern Monte Carlo simulation inverts this process by using a known PDF to model or solve a problem probabilistically. This Monte Carlo method was first used during WWII to develop nuclear weapons as part of the Manhattan Project[37].

Monte Carlo simulations can be grouped into two main types; sequential and Markov-chain. Sequential Monte Carlo is used to simulate processes where the probability of each event occurring is dependent on the event that occurred previously. Markov-chain Monte Carlo probabilities however, don't depend on other events but on pre-defined probability distributions that may be functions of location and time[38]. Monte Carlo radiative transfer (MCRT) is a form of Markov-chain Monte Carlo where the probabilities of radiation absorption and scattering depend on the optical properties at each location.

MCRT is now considered the 'gold standard' of radiation transport modelling. Although it originated as a tool for nuclear physics, it is now commonly used in the medical field to model radiation based treatments using the optical properties of the target tissue[39].

1.4.1 MCRT model

The MCRT model used throughout this work was an adapted version of one developed originally for research in astronomy[40, 41]. A flow chart showing the basic decision making processes of the MCRT code is shown in figure 1.6, with each component discussed in more detail below.

1.4.2 Grid setup

At the beginning of the simulation, a 3D voxel grid containing i x j x k voxels, each with dimensions x cm x y cm x z cm is defined (figure 1.7). By assigning appropriate optical
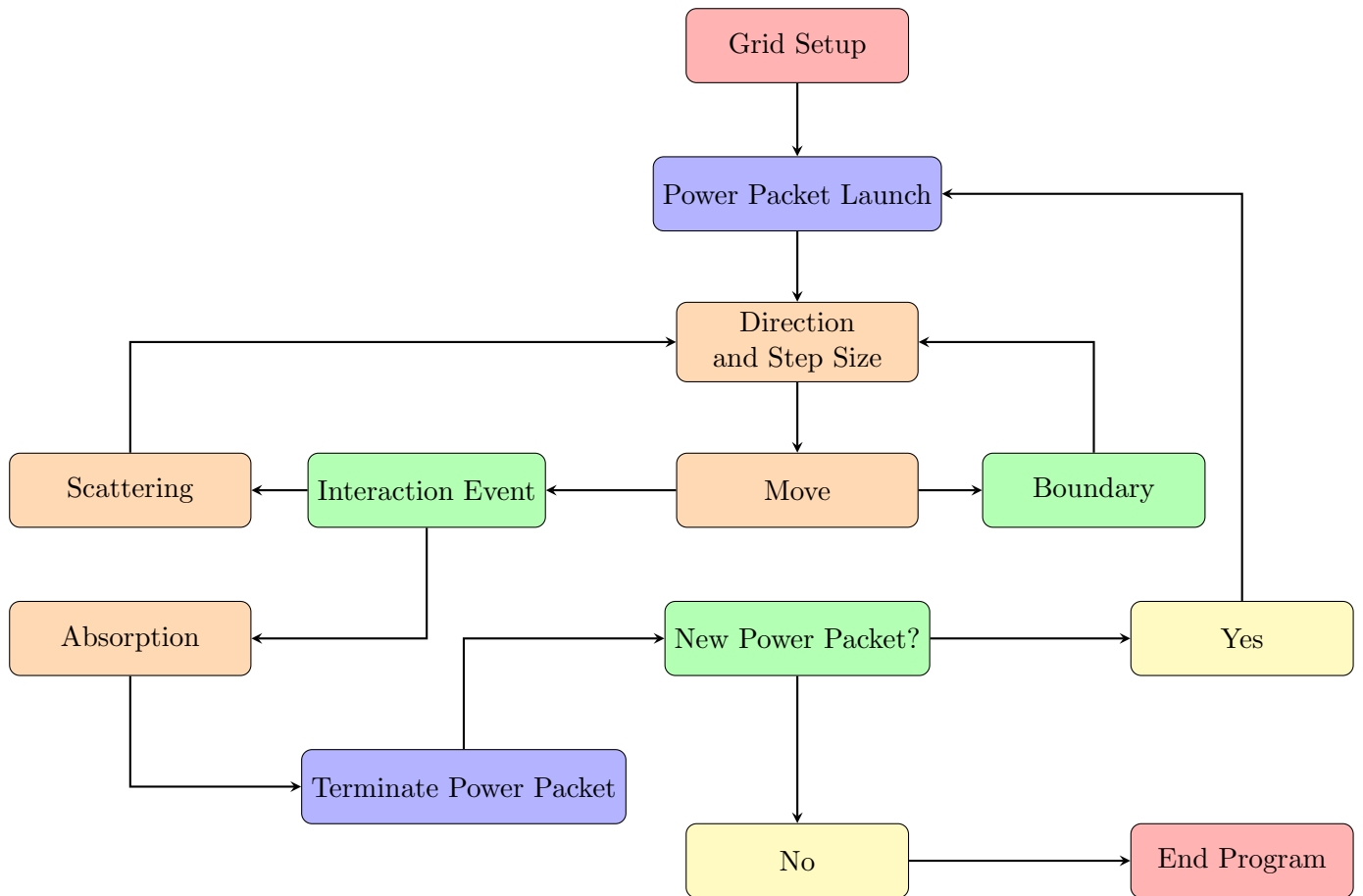
Figure 1.6: Flow chart showing the decision making process for the MCRT simulation.
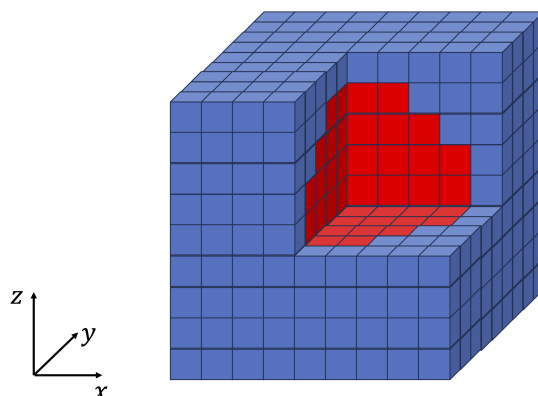
Figure 1.7: Diagram showing a low resolution 3D voxel grid, containing a discretised sphere (red voxels) at the centre.

properties to each individual voxel, a computational model of the biological medium that the light is to travel through is created. For example, figure 1.7 demonstrates how a model of a sphere is formed within the voxel grid.

Using a voxel grid comes with several advantages and disadvantages. Voxel grids are useful as they are simple to implement and its easy to adapt their resolution to the most suitable value. They also lend themselves well to parallel processing which helps to reduce simulation time. However, if the resolution of the grid is very high, large amounts of memory and computational power are needed. Due to their inability to produce truly curved surfaces, voxel grids can also cause artefacts in the photon paths at the edges of curved objects. These are caused by the difference in the way light refracts and diffracts at curved and flat edges.

1.4.3   Power packet setup

Power packet definition

To reduce the computational time and power needed for the simulation, photons are bundled together into power packets which are propagated through the model instead of individual photons. Each power packet contains ($N_{photons}$) which can be calculated using equation 1.28 where λ is the wavelength of the incident light (nm), E is the energy of the power packet (J), h is Planck's constant (JHz^{-1}) and c is the speed of light in a vacuum

(ms^{-1}).

$$N_{\text{photons}} = \frac{E\lambda}{hc} \tag{1.28}$$

The power packet's energy can be calculated using equation 1.29 where L is the light source irradiance, A is the area of illumination and $N_{packets}$ is the number of power packets simulated within the simulation time t.

$$E = \frac{ALt}{N_{\text{packets}}} \tag{1.29}$$

Power packet position and direction setup

Before launching the power packet into the medium, its initial position and direction needs to be decided. Both will depend on the type of light source being used. As an example, when launching power packets from an isotropic point source placed at the centre of a sphere (position $= [x_p, y_p, z_p] = [0, 0, 0]$), the initial direction vector is set as $[n_x, n_y, n_z]$ where:

$$\begin{aligned} n_x &= \sin\theta \cdot \cos\phi \\ n_y &= \sin\theta \cdot \sin\phi \\ n_z &= \cos\theta \end{aligned} \tag{1.30}$$

Assuming emission is isotropic, where the power packet can be emitted in any direction, $\cos\theta$ can have any value within the range -1 to 1 and ϕ any value in the range 0 to 2π. Using the inverse transform sampling method described above, these are calculated using equations 1.31 and 1.32, where ξ is a random number between 0 and 1.

$$\theta = \cos^{-1}(2\xi - 1) \tag{1.31}$$

$$\phi = 2\pi\xi \tag{1.32}$$

1.4.4 Moving

Step size calculation

Once the initial position and direction of the power packet has been calculated, the distance it will travel before interacting with the medium (the step size) will be decided. The probability of an interaction event occurring is dependant on the optical properties, or, more specifically, the extinction coefficient (μ_t), of the medium. The probability that a

power packet will interact with the medium while travelling a distance dl is equal to $\mu_t dl$. So the probability that the power packet will travel a distance l without interacting is:

$$P(l) = e^{-\mu_t l} = e^{-\tau} = P(\tau) \tag{1.33}$$

where the optical depth (τ) is defined as the mean free path. This is the average distance a power packet will travel before it interacts. $P(\tau)$ is the probability density function (PDF) of τ. The optical depth is converted to a physical distance l using the equation:

$$\tau = \int_0^l \mu_t dl \tag{1.34}$$

The step size for the power packet can be selected by randomly sampling from the normalised PDF (the cumulative distribution function (CDF)) of the optical depth. This is given by:

$$CDF = \int_0^\tau P(\tau)d\tau = \int_0^\tau e^{-\tau'}d\tau \tag{1.35}$$

and is equivalent to the probability of the selected step size (τ_{sample}) taking a value of τ or less. τ_{sample} is extracted from the CDF by taking a random number between 0 and 1 (ξ), sampled from a uniform distribution. ξ is equivalent to:

$$\xi = \int_0^{\tau_{\text{sample}}} e^{-\tau}d\tau \tag{1.36}$$

and τ_{sample} is found by solving equation 1.36 to get:

$$\tau_{\text{sample}} = -ln(1-\xi) \tag{1.37}$$

τ_{sample} is the the chosen step size and is converted to a physical distance l using equation 1.34. Once moved, the power packet's position vector can be updated using equations 1.38a to 1.38c.

$$x_p = x_p + l \cdot n_x \tag{1.38a}$$

$$y_p = y_p + l \cdot n_y \tag{1.38b}$$

$$z_p = z_p + l \cdot n_z \tag{1.38c}$$

It should be noted here that for more complex models where μ_t varies between each voxel, τ must be recalculated each time the power packet enters a new voxel. The total distance travelled l over the step size is described by equation 1.39 and illustrated in figure 1.8.

$$l = \sum_i \Delta l_i = \frac{\tau_{\text{sample}}}{\sum_i \mu_{t,i}} \tag{1.39}$$
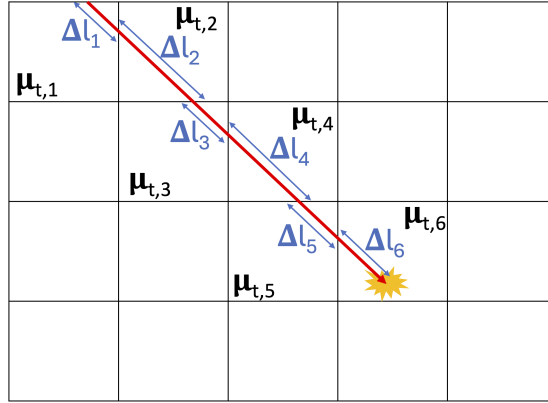
Figure 1.8: Diagram showing the path of a power packet through the voxel grid along a single step until an interaction point is reached. The optical properties $(\mu_{t,i})$ can vary between each voxel, but are uniform within the voxel.

Path length estimators and fluence rate calculation

When the power packet passes through a voxel, it deposits some energy into the voxel, dependant on its path length through the voxel (figure 1.8). The total energy deposited into a voxel at position (i,j,k) is calculated using equation 1.40 while the fluence rate within each voxel at the end of the simulation is calculated using equation 1.41.

$$E_{abs}(i,j,k) = \frac{P}{VN} \sum l(i,j,k)\mu_a(i,j,k) \tag{1.40}$$

$$\Psi(i,j,k) = \frac{P}{VN} \sum l(i,j,k) \tag{1.41}$$

Here:
P = power of the light source (W)
V = voxel volume (cm^3)
N = total number of emitted power packets
$\sum l(i,j,k)$ = sum of path lengths of all the power packets to pass through voxel (i,j,k) (cm)
$\mu_a(i,j,k)$ is the total absorption coefficient within voxel (i,j,k) (cm^{-1})
$\Psi(i,j,k)$ = fluence rate in voxel (i,j,k) (Wcm^{-2})

In other MCRT models, it is not always the case that path length estimators are used to calculate absorbed energy and fluence rate. Often, a combination of weighted photon packets and a survival roulette are used instead. When using weighted photon packets, each packet is launched with the same weight which is reduced gradually at each integration. The amount that is it reduced by is dependant on the optical properties of the medium at the position of interaction and the current weight of the photon. The weight reduction also determines the amount of energy absorbed by the medium at the interaction point. Once the weight of the photon packet gets below a specified threshold value, it undergoes a survival roulette at each interaction point. This is when a the photon packets weight and a generated random number are used to decide if the photon carries on or is terminated via the rejection method. Using this method can be more efficient, especially in mediums that are highly scattering. However, using path length estimators reduces the complexity of the simulations and allows the energy absorbed along a photon packets path to be calculated directly.

1.4.5 Boundary behaviour

If the power packet encounters a boundary, such as a change in refractive index or tissue type, before it has travelled the full step size distance, it will be either reflected or refracted, resulting in a change of direction. Both Snell's law and Fresnel equations are used within the model to implement this. The power packet's probability of reflecting at a boundary $(R(\theta_i, \theta_f))$ is determined by equation 1.42 where n_i and n_f are the refractive indices of the first and second mediums respectively and θ_i and θ_f are the incident and refractive angles respectively (see figure 1.9).

$$R(\theta_i, \theta_f) = \frac{1}{2}\left[\left|\frac{n_i \cos\theta_i - n_f \cos\theta_f}{n_i \cos\theta_i + n_f \cos\theta_f}\right|^2 + \left|\frac{n_i \cos\theta_f - n_f \cos\theta_i}{n_i \cos\theta_f + n_f \cos\theta_i}\right|^2\right] \tag{1.42}$$

The refractive angle (θ_f) is found using Snell's law:

$$\theta_f = \sin^{-1}\left(\frac{n_i \sin\theta_i}{n_f}\right) \tag{1.43}$$

Whether reflection or refraction occurs is decided by selecting a random number ξ. If $\xi < R(\theta_i, \theta_f)$ then the power packet is reflected, making the probability of refraction $1 - R(\theta_i, \theta_f)$.

Repeating boundaries

If the power packet leaves the voxel grid at any point within the simulation, it is terminated and either a new power packet is launched or the simulation ends. However, if the illuminated area from the light source is larger than the voxel grid area, such as when
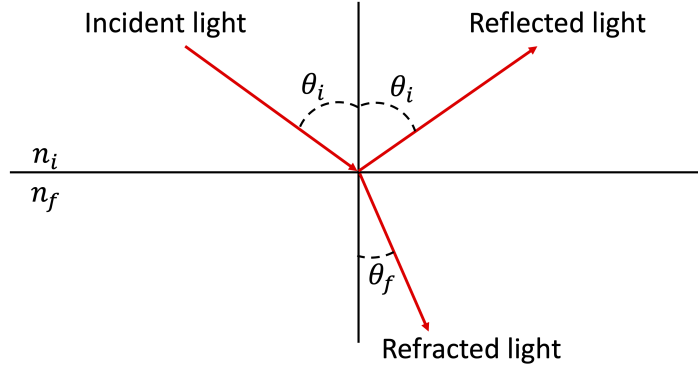
Figure 1.9: Diagram showing the angle of incident light (θ_i) and the resulting angles of reflection (equal to θ_i) and refraction (θ_f) across a boundary with refractive indices n_i and n_f according to Snell's law (equation 1.43).

simulating the irradiation of skin with a phototherapy lamp, repeating boundaries may be implemented. If this is the case, power packets leaving either through the top or bottom of the grid (z-faces) will still be terminated, but packets leaving through the sides of the grid (x or y faces) will be re-entered into the grid through the opposite face and in the same direction of travel as demonstrated in figure 1.10. This results in a 'semi-infinite' slab of tissue, allowing the fluence rate values obtained to correspond to a larger area of skin without dramatically increasing the computational resources needed.

1.4.6 Interaction event

Albedo

Once the power packet has travelled the full step size distance, an interaction event will take place where the packet will either be scattered or absorbed. The probability that the power packet will be scattered is determined by the albedo (a) which depends on the optical properties and is described by equation 1.44.

$$a = \frac{\mu_s}{\mu_a + \mu_s} = \frac{\mu_s}{\mu_t} \tag{1.44}$$

The type of event that occurs is again determined by selecting a random number ξ between 0 and 1 from a uniform distribution. If the number selected is more than the albedo, the
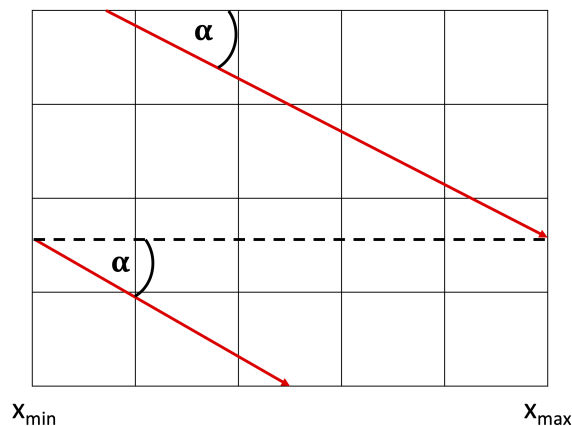
Figure 1.10: Diagram demonstrating repeating boundary conditions within the MCRT code. If a power packet exits the grid out of an x or y face, it will re-enter the grid through the opposite side along the same direction of travel. In this way, a grid with semi-infinite boundaries is produced.

packet is absorbed. Otherwise, the power packet is scattered and a new direction of travel determined.

Absorption

In the case of absorption, the power packet is usually terminated and either a new packet is launched or the simulation ends. However, if fluorescence is being simulated, the packet may be isotropically re-emitted from the absorption location with the appropriate fluorescence wavelength.

Scattering

In the case of scattering, a new step size and direction needs to be selected. Both the polar angle θ and the azimuthal angle ϕ need to be decided within the ranges $0 \leq \theta \leq \pi$ and $0 \leq \phi \leq 2\pi$. The azimuthal angle has an isotropic distribution and is simply given by equation 1.32. Polar scattering however is not isotropic and in biological tissue, its probability density function can be described using the Henyey-Greenstein phase function defined in equation 1.45, where θ is the angle between directions before and after scattering

and g is the anisotropy factor.

$$\zeta_{HG}(\theta) = \frac{1 - g^2}{4\pi(1 + g^2 - 2g\cos(\theta))^{\frac{3}{2}}} \tag{1.45}$$

In the same way as optical depth was selected, the new polar angle is found by sampling the CDF of equation 1.45 and solving to get:

$$\cos(\theta) = \begin{cases} \frac{1}{2g}(1 + g^2 - (\frac{1-g^2}{1-g+2g\xi})^2) & \text{for} \quad g \neq 0 \\ 2\xi - 1 & \text{for} \quad g = 0 \end{cases} \tag{1.46}$$

As this new angle will only be in relation to the previous angle, it must be converted to Cartesian coordinates. This is done using equations 1.47a to 1.47c, where (n_x, n_y, n_z) is the initial direction vector and (n'_x, n'_y, n'_z) is the new direction vector.

$$n'_x = \frac{\sin(\theta)(n_x n_z \cos(\phi) - n_y \sin(\phi))}{\sqrt{1 - n_z^2}} + n_x \cos(\theta) \tag{1.47a}$$

$$n'_y = \frac{\sin(\theta)(n_y n_z \cos(\phi) + n_x \sin(\phi))}{\sqrt{1 - n_z^2}} + n_y \cos(\theta) \tag{1.47b}$$

$$n'_z = -\sqrt{1 - n_z^2}\sin(\theta)\cos(\phi) + n_z \cos(\theta) \tag{1.47c}$$

1.4.7 Simulation output

Once complete, the simulation outputs a 3D array containing the final value of fluence rate within each voxel. This can be used for further analysis and calculation. Examples include working out the penetration depth of the light into the tissue or, in the case of PDT, the fluence rate can be used to estimate the photodynamic dose by calculating the energy absorbed by the photosensitiser. Both of these examples are discussed in more detail in later chapters.

1.5 Thesis synopsis

Within this work, MCRT is used to model the path of light within biological tissue. The penetration depth of light within the wavelength range 200 nm - 1000 nm into a 6-layer skin model is first simulated. The MCRT code is adapted to model PDT, accounting for light fluence, photosensitiser concentration and oxygen concentration as a function of time and location before being used to model intraoperative PDT treatment for glioblastoma brain tumours. Finally, the effect of intraoperative PDT on the temperature of brain tissue is explored.

Chapter 2

Penetration depth of light into skin

2.1 Summary

The MCRT code is used to model the penetration depth of light into skin with Fitzpatrick skin photo-type I using a 6-layer skin model. The results are compared for direct and diffuse light sources as well as various stratum corneum thicknesses and light incident angles. The lateral spread of light into skin from a laser beam at several different wavelengths is also explored. The majority of work within this chapter was published in *Photochemistry and Photobiology* in 2021[42].

2.2 Introduction and background

The diagnosis rate of skin cancer, as well as other skin conditions such as psoriasis, is currently increasing[43, 44]. With the advancement of medical technology, there is also a growing expectation and demand for low toxicity and non-invasive treatments[45, 46, 47, 48]. Due to the low penetration depth required, as well as their ease of access, it is becoming more common for skin conditions to be treated using non-invasive light based therapies. It is therefore important to be able to fully understand the occurring interactions between light and skin. A detailed picture of the wavelength dependent penetration depth of light into skin can help with this.

A current challenge faced by clinicians using treatments such as psoralen-UVA (PUVA) photochemotherapy, UV-phototherapies or photodynamic therapy (PDT) is finding the optimal PDT dose. This is the light energy and photosensitiser concentration that achieves the best balance between maximal therapeutic effect minimal damage. It is difficult to predict what the fluence rate distribution will be in each circumstance as this depends both on the light source used, as well as characteristics of the individuals skin, such as melanin content and layer thickness[49, 4, 50]. Knowing how much light is getting into skin is

also vital for monitoring the safety of UV light devices such as sunbeds and germicidal UV lamps[16, 51, 52]. An accessible and clear way to access this information is therefore needed.

This work uses the MCRT code described in chapter 1 to model the penetration depth of light into a 6-layer skin model of Fitzpatrick skin type I for the wavelength range 200 nm - 1 μm. Such simulations have been used previously [48, 53, 54], however the large wavelength range and skin-model resolution makes this simulation unique. Often in literature, the penetration depth of full wavelength range categories such as UV, visible light and IR is represented using a single depth value or solid arrow ending suddenly at a specific depth[47, 55]. This is very unrealistic as the wavelengths within each category do not travel the same distance into skin and can have very different penetration depths, making such representations misleading. It is also the case that light doesn't just stop suddenly, but instead its intensity attenuates slowly as it is scattered and absorbed by the medium. A method of presenting results that also represents the light intensity at each depth would be much more informative and is something this work aims to provide.

2.2.1 Skin

The skin is the largest organ in the body and makes up a total of 15 % of an average adults body weight. It provides many function such as helping with temperature control, moisture retention and protection against harm from threats like pathogens and UV radiation. There are 3 main layers to the skin which consists of the epidermis, dermis and subcutaneous fat or hypodermis as shown in figure 2.1[56, 57].

Epidermis

The epidermis is split into 5 layers and contains cells called keratinocytes which produce keratin, a protein which gives skin its protective functions. From the surface down, the 5 layers are:

- Stratum corneum, made of horny cells and dead keratinocytes

- Stratum lucidum, only present in the thicker skin on palms and sole of the feet

- Stratum granulosum, containing keratinocytes migrating upwards

- Stratum spinosum, containing tufts of keratin and desmosomes which bond them together

- Stratum basale (basal layer), containing melanin producing melanocytes and proliferating cells[57]

Keratinocytes are produced in the basal layer and migrate upwards over time. When they reach the top of the skin, they die and form the stratum corneum[58].

Dermis

The dermis is formed of 2 main layers:

- Papillary layer, made of connective tissue (collagen) that attaches to the epidermis and give the layer an undulating shape (figure 2.1)

- Reticular layer, also contains connective tissue as well as other structures such as sweat glands, hair follicles and blood vessels[57]

Subcutaneous fat

Contains mainly fat cells called lipocytes which help insulate the body[56].

2.2.2 Light and skin interaction

It is possible for skin to interact and react to specific wavelengths of light due to the fact that it contains chromophores. These are molecules that change as a result of absorbing light[59]. The main chromophores present in skin are melanin, haemoglobin, water and DNA[16]. Skin and light interactions can be both positive and negative. An example of a positive interaction is the synthesis of vitamin D via epidermal absorption of sunlight in the UV range[60]. However, too much UV absorption can also have negative effects such as erythema (skin reddening due to inflammation) and the development of skin cancer when the DNA in the basal layer is damaged[57].

Phototherapy

Phototherapy is a branch of medicine that takes advantage of the interactions between light and skin to treat various skin conditions. Treatment using light in the UV range is the most established and is commonly used in dermatology to treat conditions such as psoriasis, atopic dermatitis, vitiligo and skin cancer[61, 62]. Visible light is also widely used, especially in the form of lasers which can be used for both cosmetic and medical treatments[63].

Skin photo-types

An important consideration when looking at interactions between light and skin is the specific photo-type of the skin. This is dependant on melanin concentration and can be described using the Fitzpatrick scale. Table 2.1 presents descriptions of each Fitzpatrick skin type.

The scale was originally developed to classify white skin in order to find the correct dose of UVA light to treat psoriasis. Its main parameter is the tanning reaction of skin when it is
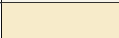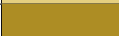
Fitzpatrick Type	Burning/Tanning Likelihood	Colour
I	Easily burns, no tan	
II	Often burns, slight tan	
III	Occasional burns, occasionally tan	
IV	Rare burns, usually tans	
V	Very rare burns, easily tans	
VI	No burns, always tans	

Table 2.1: Table presenting descriptions of the 6 Fitzpatrick skin photo-types[64].

exposed to UV light. Although it is still widely used in dermatology, the scale has several downsides, one of which is the fact that skin pigmentation does not correlate linearly with UV damage risk. It is also the case that in reality there is a much more extensive range in skin pigmentation types than the Fitzpatrick scale describes and so using only it to plan photo-treatments and asses risk is not ideal[64]. The concentration of melanin in skin has a big impact on the effectiveness and safety of phototherapy treatments, and so more comprehensive classification and treatment planning is needed.

2.3   Methods

2.3.1   Skin model

The skin model used within the simulation was based on the 5-layer model developed by Barnard et al.[16], with an additional layer added to the bottom to form a 6-layer model. A diagram showing the layers within the model and their corresponding thicknesses can be seen in figure 2.1.

2.3.2   Selected optical properties

Appropriate optical properties for each model layer needed to be found for every wavelength from 200 nm - 1 μm. The properties used consisted of absorption and scattering coefficients (μ_a and μ_s), the anisotropy factor (g) and the refractive index (n). Throughout the literature search for the required optical properties, it was found that the reported properties varied significantly between literature sources, and so focus was placed on finding properties that fit well together across the range (minimal jumps between data sets) and contained expected peaks given the biological content and structure of the relevant tissue. Scattering in the skin is mainly caused by proteins or lipids situated in fluids between the skin cells. The stratum corneum contains mostly lipid scatterers while the deeper layers contain mostly protein scatterers like keratin in the lower epidermal layers and collagen and elastin in the dermis. The main absorbsers present in the skin, within the relevant wavelength region, are blood, melanin and keratin. Keratin forms a main component of
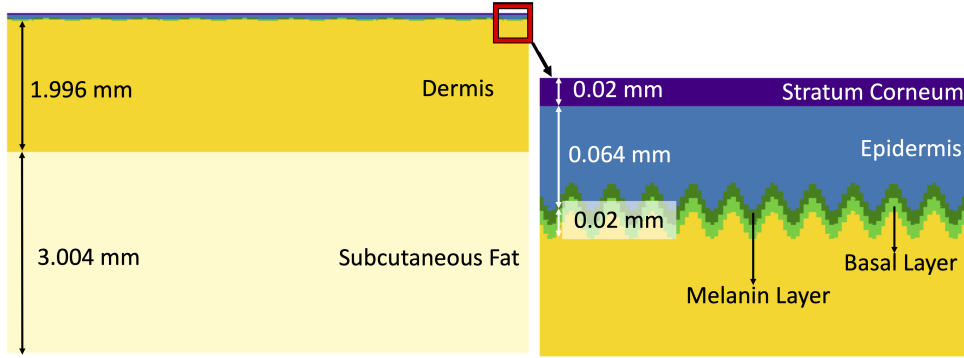
Figure 2.1: Image showing the developed skin model layers with corresponding thicknesses. The layer thicknesses were chosen from published values by Iglesias-Guitian et al. and Barnard et al.[65, 16]. The epidermal thickness is from the bottom of the stratum corneum to the trough of the undulations in the melanin and basal layers, caused by the protruding dermal papillae. The melanin and basal layer thicknesses are 0.01 mm each, totalling the labelled 0.02 mm. The figure is adapted from Finlayson et al.[42].

the stratum corneum and the epidermis. Within this model, melanin is concentrated into a single layer just below the epidermis and blood is only present in the dermis[21, 66].

The refractive index was chosen to be a constant value of 1.38 for all wavelengths and all skin layers. The value of g was also assumed to be equal for all layers but varying with wavelength according to equation 2.1[67].

$$g(\lambda_{\mathrm{nm}}) = 0.62 + 0.29\lambda_{\mathrm{nm}} \times 10^{-3} \tag{2.1}$$

Figure 2.2 presents the chosen absorption and scattering coefficients for each of the layers.

Stratum Corneum

The scattering and absorption coefficients used for the stratum corneum (layer 1), for the wavelength range 200-400 nm, were taken from work presented by Van Gemert et al.[68]. Using reflectance and transmission measurements taken by Everett et al.[69] through a slab of skin, Van Gemert derived the coefficients using the Kubelka-Munk formalism described in chapter 1. In order to extend this range to 700 nm, Everett's original reflection and transmission data was obtained using a graphical data extraction tool and the Kubelka-Munk formalism used to convert these to absorption and scattering coefficients. To extend the data further to 1 μm, the assumption was made that the coefficients remained roughly constant from 700 nm - 1 μm, due to the fact that both the transmission and reflection data
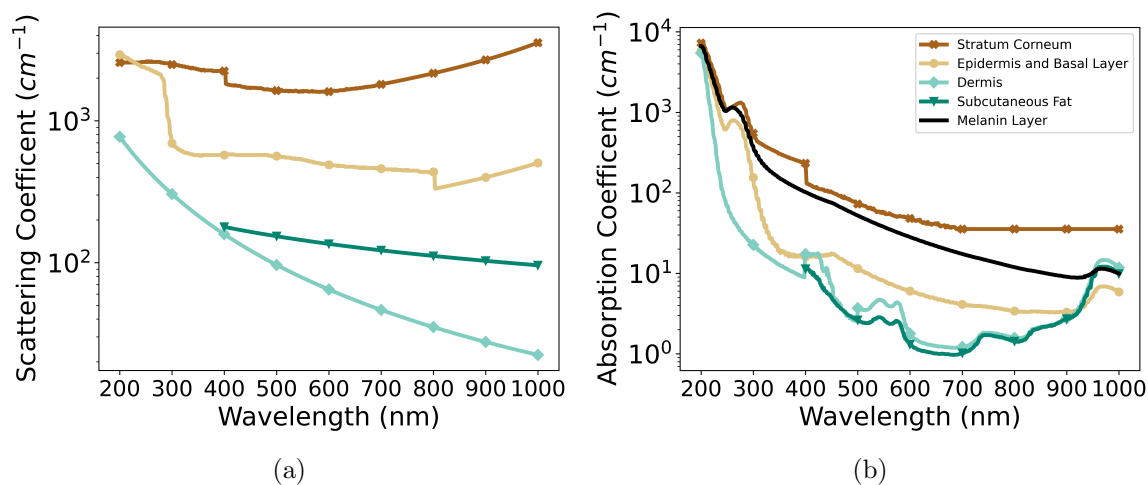
Figure 2.2: Plots presenting the chosen a) scattering and b) absorption coefficients as a function of wavelength[42]. Each line colour represents a different skin layer. Stratum corneum data is taken from a combination of Van Gemert et al. and Everett[68, 69]. The absorption data for the epidermis, basal and melanin layers was also taken from Van Gemert et al.[68] as well as Meglinski et al.[70]. The melanin absorption, calculated using equation 2.2 is subtracted from the epidermis absorption to form data for the melanin-less epidermal layer. The scattering data for the epidermis, basal and melanin layers was taken from a combination of Van Gemert et al. and Everett[68, 69]. The absorption data for the dermis was taken from a combination of Van Gemert et al. and Meglinski et al.[68, 70] while the scattering data was calculated using equation 2.4[71]. Finally, the absorption data for the subcutaneous fat layer was taken from Meglinski et al. while the scattering data was calculated using equations 2.5 and 1.3[70, 72].

were flattening off. However, it is possible that a slight increase in the stratum corneum absorption coefficient would occur at these wavelengths, due to water present in the layer.

Epidermis

Absorption and scattering coefficients for the epidermis were again obtained from the data presented by Van Gemert[68] from 200nm-800nm. The scattering coefficients were extended to 1 μm using the Kubelka-Munk formalism and data from Wan et al.[73], again with the assumption that the flattening of reflection and transmission coefficients were constant beyond 700 nm. The absorption coefficients for the range 200-450 nm were also taken from van Gemert while the coefficients for the range 451-1000 nm presented by Meglinski et al.[70]. To comply with the assumption that melanin in Fitzpatrick skin type I and II is only present in the melanin layer[16, 74], the absorption coefficient of melanin was subtracted from the epidermis absorption.

Melanin's absorption coefficient is calculated using equation 2.2, where λ is the wavelength of the light and F_{mel} is the melanin fraction within the skin, something that varies between Fitzpatrick skin types.

$$\mu_{a,\text{melanin}}(\lambda_{\text{nm}}) = 6.6 \times 10^{11} \lambda_{\text{nm}}^{-3.33} F_{\text{mel}} \qquad (2.2)$$

The fraction of melanin in the skin measured by Wan and Meglinski was assumed to be 0.04[73, 70].

Melanin layer

As discussed above, it is assumed that the melanin in Fitzpatrick skin types I and II can be represented as a single, concentrated layer at the bottom of the epidermis. The model used was chosen to be skin type I which has a melanin fraction of 2 %[16, 65, 75]. However, this value represents the melanin fraction of the full epidermis, and so needs to be adjusted for the model where the full amount of melanin is concentrated into the melanin later. This adapted value is calculated using equation 2.3 where N_{epi} and N_{mel} are the total number of voxels that make up the models epidermis and melanin layer.

$$F_{\text{mel,adapted}} = F_{\text{mel}} \frac{N_{\text{mel}} + N_{\text{epi}}}{N_{\text{mel}}} \qquad (2.3)$$

The scattering coefficient of the melanin layer was assumed to be equal to that of the epidermis.

Basal layer

As the basal layer in skin is part of the epidermis, the optical properties were assumed to be equal to those of the melanin-removed epidermis.

Dermis

The absorption coefficients for the dermis in the range 200 - 449 nm were taken from Van Gemert et al.[68] while the remaining data from 450 nm - 1 μm was obtained from data presented by Meglinski et al.[70]. While Van Gemert did present the data up to 800 nm for the dermis, the values given by Meglinski were chosen due to the fact that they, unlike the Van Gemert data, contain peaks at 420 nm, 540 nm and 970 nm. At these points, boosts in absorption from haemoglobin and water are expected, and so it was assumed that these data are more accurate.

The scattering coefficients for the dermis were calculated using the equation 2.4, produced by Jacques[71].

$$\mu_{s,\mathrm{derm}}(\lambda_{\mathrm{nm}}) = (1.752 \times 10^8)\lambda_{\mathrm{nm}}^{-2.33} + 134.67\lambda_{\mathrm{nm}}^{-0.494} \tag{2.4}$$

Subcutaneous fat

The absorption coefficient for the subcutaneous fat layer was taken from the data presented by Meglinski et al.[70].

The reduced scattering coefficient was calculated using equation 2.5[72].

$$\mu'_{s,\mathrm{sub}} = 1050.60\lambda_{\mathrm{nm}}^{-0.68} \tag{2.5}$$

The scattering coefficient could be calculated using equation 1.3.

2.3.3 Implementation into code

A voxel grid with dimensions 1 mm x 1 mm x 5 mm and containing 100 x 100 x 800 voxels was used as a base for the skin model within the code. Due to the stark differences in the thicknesses of the layers (see table 2.2), 5 different voxel volumes were used. This allowed higher resolution data to be obtained in the thin upper layers, where the penetration depth of light in the UV range, for example, is of great interest. It also allowed the number of voxels in the deeper, thicker layers, where high resolution data is less of a priority, to be kept low. This kept the required computational time and power needed to run the MCRT simulation within reasonable limits. The stratum corneum is the thinnest layer in the model at 20 μm, but due to its importance in protecting/preventing some wavelengths of light from reaching the lower layers, it was given the highest resolution with 200 layers of voxels, each with a z-depth of 0.1 μm.

The penetration of light through the epidermis is also of great interest, especially when looking at the transport of potentially harmful UVA and UVB wavelengths which may penetrate the stratum corneum. It was given a slightly lower, but still high resolution of

Layer	Thickness (mm)	Average Depth (mm)	Resolution (μm)
Stratum corneum	0.02	0.02	0.1
Epidermis	0.064(*)	0.084	0.53
Melanin layer	0.01	0.094	0.32
Basal layer	0.01	0.104	0.32
Dermis	1.996	2.1	13.0
Subcutaneous fat	3.004	5.0	20.0

Table 2.2: Skin layers contained within the model along with their corresponding thicknesses, average depths from the skins surface and voxel resolutions[65, 16]. *From the top of the epidermis to the trough of the undulation wave.

0.53 μm. To model the undulating dermal papillae that protrude into the lower epidermal layers, the voxel positions at the bottom of the epidermis, as well as the melanin and basal layers, were adapted using equation 2.6, where *depth* is the average depth presented in table 2.2, to approximate the undulations as a sine wave.

$$z(x,y) = 0.03\text{mm} \times \sin \frac{\text{x}}{0.015\text{mm}} \times \cos \frac{\text{y}}{0.015\text{mm}} + \text{depth(mm)} \qquad (2.6)$$

The maximum thickness of the epidermis, from the top of the layer to the trough of the wave is 64 μm. The melanin and basal layers were given the same resolution of 0.32 μm and thickness of 10 μm.

Both the dermis and subcutaneous fat layers are much thicker than the epidermal layers and therefore less resolution was required. The dermis was given a resolution of 13 μm with a thickness of 1996 μm and the subcutaneous fat was given a resolution of 20 μm and a thickness of 3004 μm.

Finally, to allow the model to simulate a semi-infinite slab of skin, repeating boundary conditions, as described in section 1.4.5 were implemented.

2.3.4   Parameters explored

Once complete, the skin model was used to test the effect of several parameters on the effect of light penetration into skin.

Direct light vs diffuse light

First, the difference in light penetration depth when using either a direct or diffuse light source was explored. In both cases, the light source was set to be evenly distributed across the top of the grid. Due to reflection, refraction and scattering effects, a large portion of

the light either did not enter the grid or quickly escaped through the top. The direct source was set so that each power packet enters the grid at an angle normal to the surface. This was achieved by setting the polar angle $\theta = 1$ in equation 1.31, resulting in the n_x and n_y direction vectors being set to 0. For the diffuse light source, the polar and azimuthal angles were selected using equations 1.31 and 1.32. Each simulation was run for the full wavelength range of 200 - 1000 nm in 1 nm steps and the fluence rates down a central column of the resulting fluence rate grid was extracted to obtain the penetration depth results. Producing data for each nm resulted in a very large dataset, but it was believed that this level of detail would increase the usefulness and adaptability of the data. For example, it could be used to study the contribution that each wavelength within a very narrow bandwidth source makes to the fluence rate in skin. Then it could also show the difference that filtering out certain wavelengths could make.

Stratum corneum thickness

Next, the effect of stratum corneum thickness on the penetration of light in the 200 - 400 nm (UV) range was tested. We can see from figure 2.2, that for wavelengths within this region, the stratum corneum is optically much thicker than those beyond it. This results in the stratum corneum providing its protective function against UV rays. However, the thickness of the stratum corneum is known to vary, both between people and different body sites. Certain skin conditions can also result in the stratum corneum being compromised or fully removed[76]. It is therefore important to investigate how these changes may effect the level of UV energy reaching the lower epidermal layers. Simulations were run using an evenly distributed, direct light source. Stratum corneum thicknesses of 0 μm, 10 μm, 14.8 μm, 20 μm and 30 μm were chosen to represent the compromised case as well as common thicknesses found in the shoulder, buttock, forearm and face[77, 78].

Incident angle of light

The penetration depth effect of the angle of the incident light was tested. A direct, evenly distributed light source was used and simulations run for incident angles of 0°, 45° and 65° from the normal. The simulations were run for 6 different wavelengths of interest within either light-based therapy or radiation safety studies. These wavelengths were chosen to be 222 nm, 300 nm, 350 nm, 400 nm, 630 nm and 800 nm.

Lateral spread of laser light

Finally, the lateral spread of different wavelengths of laser sources within the skin were investigated. A uniform laser beam of diameter 0.1 mm was simulated and positioned at the centre of the top of the grid, with all power packets entering the grid at the normal angle. The same 6 wavelengths chosen for the incident angle investigation (section 2.3.4)

were also used here. For this investigation, the repeating boundary conditions were removed to allow the results to show the lateral spread from a single laser beam.

2.4   Results

Direct light vs diffuse light

Figure 2.3 shows the depth into the skin model reached by each wavelength of light as percentage of the incident irradiance. Percentages of 90 %, 50 %, 37 %, 10 %, 1 % and 0.1 % are shown for both the direct and diffuse light source. To view the attenuation of the UV range within the epidermal layers in more detail, the data is plotted separately in figures 2.3a and 2.3c on a log depth scale. The results show the expected increase in penetration depth with increasing wavelength until the infrared (IR) region is reached. At this point water absorption starts to take effect and the penetration depth decreases. By comparing figures 2.3a and 2.3b with figures 2.3c and 2.3d, we can see that for all wavelengths, direct incident light travels deeper into the skin than diffuse incident light.

Stratum corneum thickness

Figure 2.4 compares the penetration depth of direct light into skin for the 5 tested thicknesses of stratum corneum. Each figure plots on a log scale the depth at which the incident irradiance is attenuated to 90 %, 10 % and 1 % for the wavelength range of 200 nm - 400 nm. We can see that as the thickness of the stratum corneum is increased, the total depth of penetration into the lower epidermal layers is decreased, especially at the shorter wavelengths. The plots also show the protective function of the lower epidermal layers against light in the UVC range. Even when there is no stratum corneum present, the fluence rate within this range is attenuated to less than 1 % of the incident irradiation. Although, the intensity is still larger at this point than it is in models with a stratum corneum, so there may still be some risk to the cells in the basal layer from UVC radiation if not stratum corneum is present.

Incident angle of light

Figure 2.5 shows the normalised fluence rate as a function of depth for each incident angle tested. We can see that the larger incident angles, further away from the normal, result in an increase in fluence rate at the skins surface, but a decrease at larger depths.

The points at which the data sets in figure 2.5 intersect can be seen in table 2.3.

We can see from figure 2.5 that the normalised fluence rate goes above 1 near the top of the grid. The values are normalised against the incident irradiation and so a value above 1 suggests that the fluence rate in the upper layers of the skin are larger than the inputted
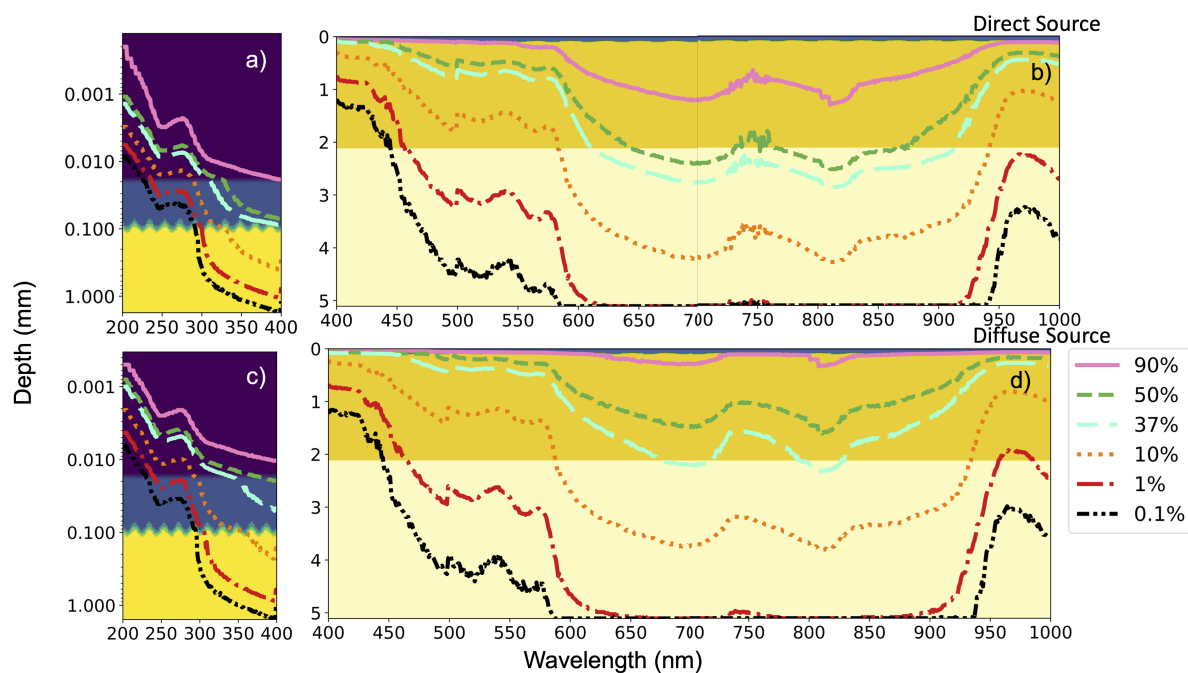
Figure 2.3: Plot comparing the penetration depth of light into skin for direct and diffuse incident light[42]. The fluence rate values are taken from a central column of voxels and the colour coded data lines on each plot indicate where the incident power has been attenuated to 90 %, 50 %, 37 %, 10 %, 1 % and 0.1 %. The plot background colouring indicates the skin layer, with the same colour scheme as figure 2.1. Figures a) and c) show the direct and diffuse results respectively for the wavelength range of 200 nm - 400 nm, plotted on a log depth scale to enhance the level of detail seen in the stratum corneum and epidermal layers. Figures b) and d) plot the direct and diffuse data for the wavelength range of 401 nm - 1000 nm on a standard depth scale. The data shows that for all wavelengths, direct light penetrates further into skin than diffuse light.
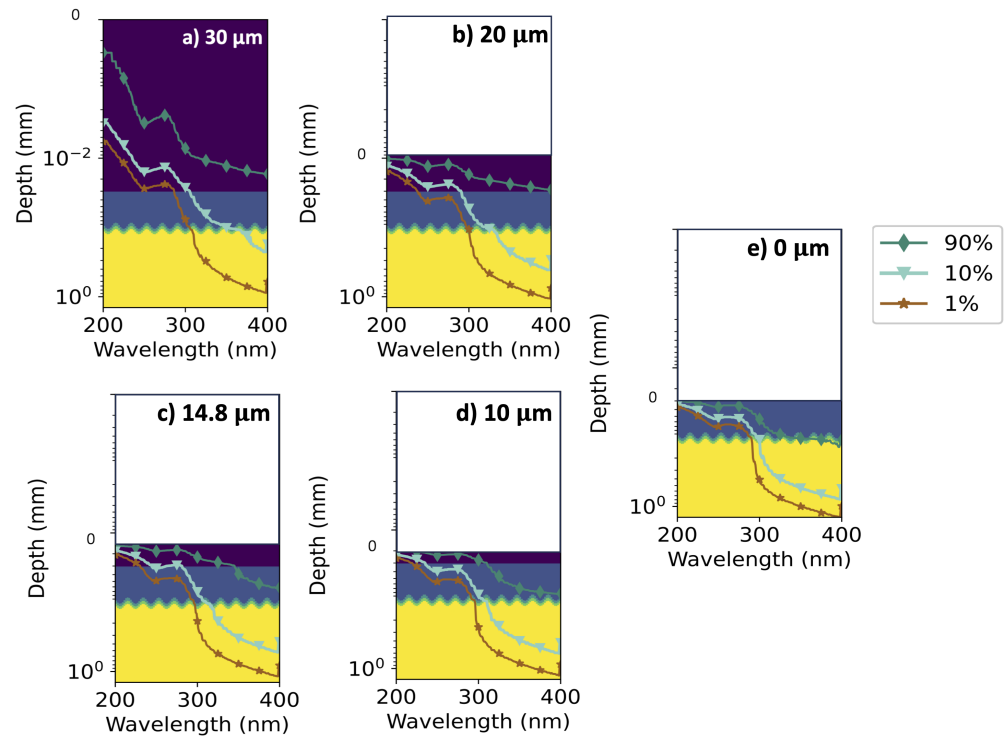
Figure 2.4: Plots comparing the penetration depth of light into skin with different thicknesses of stratum corneum[42]. Data is shown for thicknesses of a) 30 μm b) 20 μm c) 14.8 μm d) 10 μm and e) 0 μm. The lines of data indicate the depth, plotted on a log scale, at which the fluence rate is attenuated to 90 %, 10 % and 1 % of the incident light power. Data for the wavelength range of 200 nm - 400 nm is plotted over a log scaled image of the skin model where the '0' value on the depth axis shows the position of the skin models surface in each case.
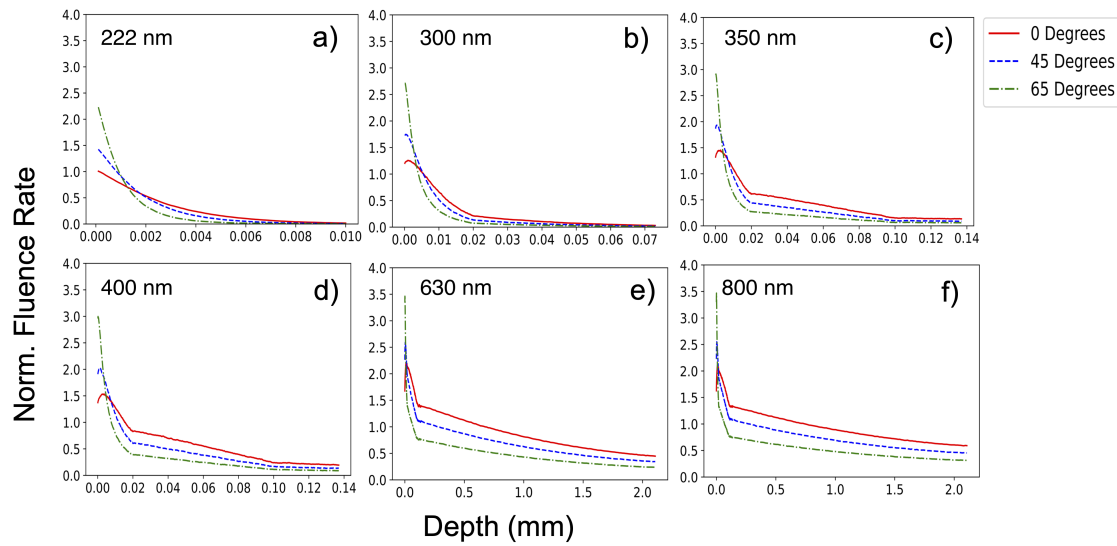
Figure 2.5: Plots showing the normalised fluence rate as a function of depth into the skin model for incident angles of 0°, 45° and 65° from the normal[42]. The results are presented for wavelengths of a) 222 nm, b) 300 nm, c) 350 nm, d) 400 nm, e) 630 nm and f) 800 nm with data extracted from the central column of the outputted fluence rate grid. At all wavelengths, penetration depth decreases with increasing angle, while the fluence rate at the top of the grid increases.

	Intersection depth (mm)					
Intersecting data-sets	222 nm	300 nm	350 nm	400 nm	630 nm	800 nm
0° and 45°	0.0017	0.0050	0.0068	0.0073	0.0145	0.0158
0° and 65°	0.0012	0.0034	0.0043	0.0047	0.0085	0.0088
45° and 65°	0.0010	0.0026	0.0031	0.0034	0.0061	0.0061

Table 2.3: Skin depth of intersection points between data sets presented in figure 2.5.

power. The physical reason for this larger fluence is due to scattering. We can see from figure 2.2b that the stratum corneum and epidermal scattering coefficients are much larger than those of the deeper layers. This means more scattering events are likely to occur in these layers per unit distance, increasing the path length that a photon will travel through the layer and resulting in an increase in fluence rate.

We can also see from figure 2.5 that the fluence rate at the top of the grid is higher for larger incident angles. A possible reason for this is the forward bias in the direction of scattering within biological tissue[68, 21]. Due to this bias, if the light enters the skin at an angle further away from the normal or z-direction, it is more likely to be scattered in the x or y directions, further increasing the path length within the top skin layers.

Lateral spread of laser light

Figure 2.6 presents contour plots, showing the lateral spread of light within the skin model for each wavelength. The contours indicate where fluence rate is attenuated to 90 %, 50 % 10 %, 1 % and 0.1 % of the incident irradiance. The results are presented for wavelengths of a) 222 nm, b) 300 nm, c) 350 nm, d) 400 nm, e) 630 nm and f) 800 nm at the central slice of the voxel grid. We can see from the plots that in each case, there are varying ranges of lateral spread, dependant on both the wavelength and the skin layer. Here the different scattering coefficients within each layer cause differences in the rate of the lights lateral spread, dictating the unique contour shape at each wavelength. For the 630 nm and 800 nm wavelengths in figures 2.6e and 2.6f, the spread goes beyond the grid width of 1 mm.

2.5   Discussion

One of the main challenges in compiling the set of optical properties used was the large variability in the values published in literature. These differences likely have several root causes such as different sample preparation and measurement methods, as well as the general variability in skin content and individual layer thickness[77, 79, 80, 81, 21]. This creates uncertainty in any published values. As it is difficult to know which values are most accurate, a focus was placed on finding values that fit well together over the full
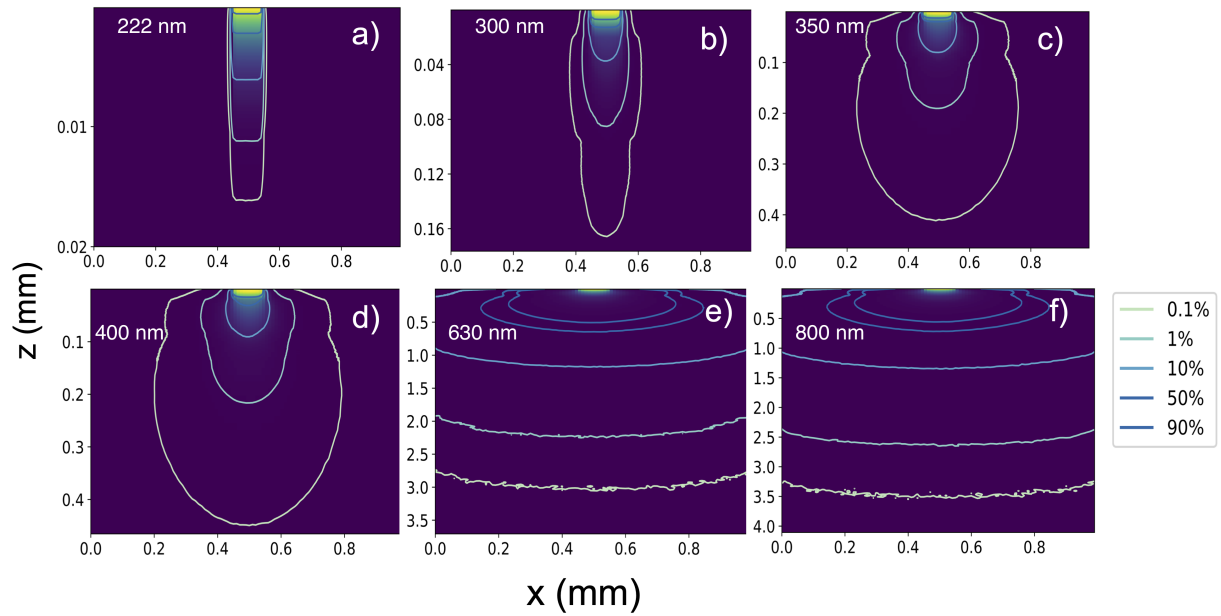
Figure 2.6: Contour plots showing the lateral spread of light into skin from a 0.1 mm radius laser beam incident normal to the surface of the skin[42]. Data is presented for wavelengths of a) 222 nm, b) 300 nm, c) 350 nm, d) 400 nm, e) 630 nm and f) 800 nm. Each plot contains 5 contours, representing the points where the fluence rate is attenuated to 90 %, 50 %, 10 %, 1 % and 0.1 % of the incident irradiance. The contour shapes are dictated by the different optical properties within each layer, where some layers allow a further spread of light than others. It can be seen in figures e) and f) that the spread of 630 nm and 800 nm light is further than the width of the grid. It should be noted that the repeating boundary conditions were turned off to allow the investigation of the lateral spread from a single laser beam.

wavelength range and contain the expected peaks relating to the biochemical content of the tissue. From the absorption coefficient plot in figure 2.2a, several peaks can seen. The peaks at 280 nm in the epidermis and stratum corneum correspond to the extra absorption due to the high amount of keratin in these layers[66]. The dermis and subcutaneous fat properties have three peaks at 425 nm (Soret peak), 545 nm and 578 nm (Q-band) due to blood[21, 66, 79]. Finally, due to the increased level of water absorption in the IR range, there is a peak at 970 nm in the epidermis, dermis and subcutaneous fat[70, 79]. While the combined data-sets fit together fairly well, some discontinuities can be seen at points where the data-sets join together due to differences in the values at these adjacent points.

It is clear from the described methods and results that the accurateness and reliability of the MCRT simulations largely depend on the accurateness of the optical properties used. However, the availability of optical properties in literature for individual skin layers is limited, especially in the highly absorbed UV-range, where measurement is more challenging[82]. This, coupled with the variability in optical properties between people, makes it clear that the simulation results cannot be applicable to treatment planning for a specific individual, but instead can be used to make broad comparisons in penetration depth between different wavelengths. One method to improve the accuracy of the results could be to allow the refractive index to vary with wavelength. As measured by Martins et al.[83], the refractive index of both rabbit pancreas and brain cortex decreases with increasing wavelength. This change should be implemented in future simulations. Changes to the optical properties of the melanin layer could also improve the simulation accuracy. The scattering coefficient of melanin was assumed to be equal to that of the epidermis, however, due to the small size of melanosomes (50 - 60 nm)[84], its scattering coefficient is likely to be significantly smaller. The refractive index of melanin has also been shown to be larger, with values of 1.7-1.8 in the visible light range[85, 86]. Making these changes should also be done in future simulations.

However, the penetration depth results in figure 2.3 do compare well to other depth values found in literature. Within the UV-range, Meinhardt et al.[82] measured *in vivo* the penetration depth of light into forearm skin and found that 300 nm light was attenuated to 37 % at a depth of around 15-30 μm while 340 nm light was attenuated to 37 % at 40-60 μm. By comparison, the simulation data in figure 2.3a show of 300 nm and 340 nm light attenuating to 37 % at depths of 15 μm and 54 μm, respectively. Within the visible light range, using a 2-D Monte Carlo simulation, Ash et al.[87] found the depth at which 450 nm and 650 nm light was attenuated to 1 % in skin was 1.6 mm and 4.75 mm, respectively. The simulation results in figure 2.3b show 450 nm and 650 nm light attenuating to 1 % at depths of 1.6 mm and just over 5 mm. These comparisons show that the penetration depth of light achieved by the simulation is within the expected range.

The advantage of the simulations reliance on optical properties is that as more optical

properties become available, such as for different photo-types and layer thicknesses, the model is easily adaptable to incorporate them. The incident light setup is completely adaptable as well, and so the model has great potential to be an excellent treatment planning tool. Its accuracy will increase proportionally with the accuracy of optical property measurement.

The results in figure 2.3 show that the penetration depth of light into skin is largest in the visible light/NIR region from roughly 620 nm - 920 nm and smallest in the UV region from 200 nm - 450 nm. This suggests that for deeper lesions, such as deep basal cell carcinoma (BCC) which can have depths of up to 5.5 mm[88], artificial red light sources, typically around 630 nm, would be more suited for PDT treatment than daylight PDT. However, due to the UV and visible light content of daylight and PpIX's large absorption peak at 420 nm, daylight PDT is well suited to treating superficial lesions as deep as 2 - 3 mm[89]. Similarly, visible light sources are well suited to vascular PDT due to their ability to penetrate down to the dermis where vascular structures are present[90]. We can see from figures 2.3 and 2.5 that, as the purpose of vascular PDT is to destroy a tumours vascular structure, using a direct source would provide further benefit as it allows deeper penetration depth in the visible range, providing higher fluence rates at larger depths.

The results in figure 2.4 align well with Eadie et al.'s statement that 222 nm germicidal lamps cause less skin damage than 254 nm lamps[52, 13]. We can see that with stratum corneum thicknesses of 14.8 μm and above, less than 1 % of 222 nm light reaches beyond the stratum corneum. However, it is only with a thick 30 μm stratum corneum that this is also the case with 254 nm. It therefore seems likely that 254 nm germicidal lamps will cause more skin damage.

2.5.1 Web app

In order to make the skin penetration depth data from figure 2.3 easily accessible, a web application was produced using R-Shiny. This can be accessed via `https://loufin.shinyapps.io/Depth_Pen_App/` The app allows users to upload a light spectrum of their choice and outputs data containing the resulting normalised fluence rate of each wavelength at each depth in the skin after irradiating it with an evenly distributed light source.

Figure 2.7 shows the app web-page which is split into 3 labelled sections. In section 1, the users spectrum can be uploaded. This should be done in the form of a single-columned CSV file. The wavelength range and step size can be chosen below this. The fraction of direct and diffuse light within the chosen source can also be specified. Once the spectrum is uploaded and the values selected, a plot of the inputted spectrum will appear at the bottom of section 1. If no spectrum file is uploaded, a default flat spectrum with a uniform value of 1 is used. The second section allows the thickness of stratum corneum to be se-
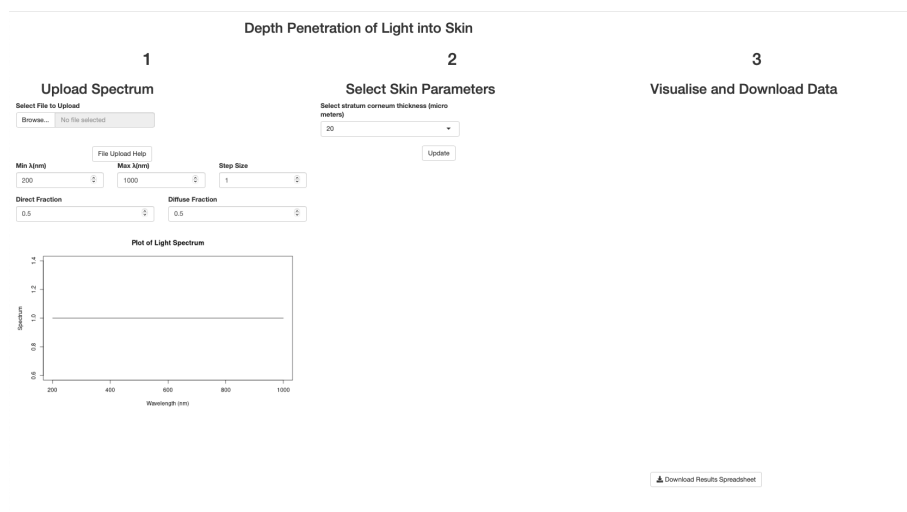
Figure 2.7: A screenshot showing how the web-app looks when first opened. The page has three sections where the user can upload their chosen spectrum, select available skin parameters, visualise and download data.

lected, however there is currently only one option of 20 μm. When the 'update' button in section 2 is pressed, two plots appear in section 3 (see figure 2.8). The top plot shows the resulting normalised fluence rate at the top of the epidermis as a function of wavelength while the bottom one shows the same, but deeper into the skin at the basal layer. A button labelled 'download results spreadsheet' is also seen below the two results plots. Pressing this downloads the full results as a spread sheet, an example of which can be seen in figure 2.9. This contains data for the normalised fluence rate of every wavelength in the uploaded spectrum for all 800 voxel depths.

2.6 Conclusion

The MCRT code was used to model penetration depth of light into skin for the wavelength range 200 nm - 1000 nm, covering the light spectrum from UV through to IR. The results were presented in a way that shows the attenuation of each wavelength, showing clearly the percentage of incident light that reaches each skin layer for both direct and diffuse sources. As expected, it was found that the penetration depth of light increases with wavelength, decreasing again when water absorption takes effect in the IR range. Across all wavelengths, the penetration depth of diffuse light was less than that of direct. Different parameters such as stratum corneum thickness and incident light angle and their effect on penetration depth were also investigated. The results show that the penetration depth
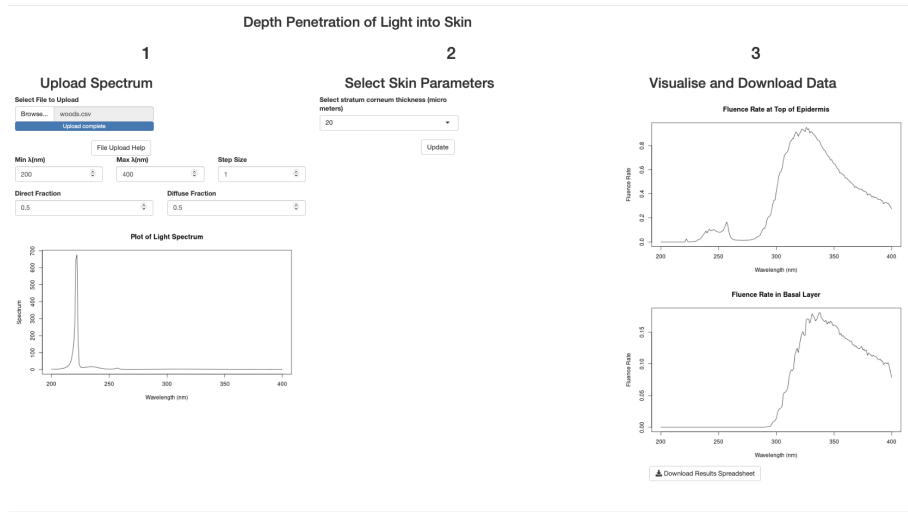
Figure 2.8: A second screen shot of the web-app showing how it looks after the user has uploaded their spectrum and selected the correct parameters. Two results plots appear that show the normalised fluence rate as a function of wavelength at the top of the epidermis and in the basal layer. The full results can be downloaded.
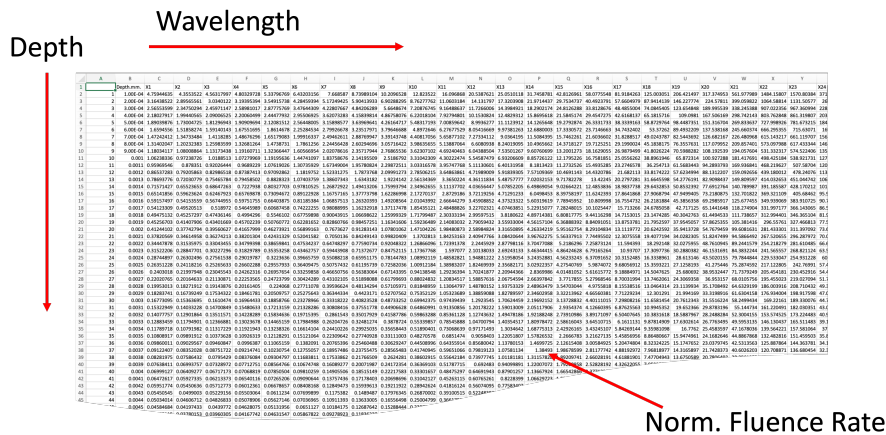
Figure 2.9: An image showing part of an example of the downloadable spreadsheet from the web-app. Depth increases vertically down each column while wavelength increases along each row. The values are the normalised fluence rate of each wavelength at each depth into the skin.

of each wavelength is decreased with increasing stratum corneum thickness, while more oblique incident angles result in higher fluence rates at the top of the skin, but smaller penetration depths.

The data presented within this work has the potential to aid clinicians and researchers in the development of new and existing light-based medical technologies and treatments for skin. Although published optical properties for skin are limited within literature, especially for Fitzpatrick skin types darker than type II, such properties could be easily incorporated into the simulation when available, in order to produce a useful and personalised planning tool.

Chapter 3

Modelling Photodynamic Therapy

3.1   Summary

The fundamentals of photodynamic therapy (PDT) are discussed before describing two different algorithms designed to computationally model it. The algorithms are individually incorporated into the MCRT code which is validated by using it to reproduce previous results.

3.2   Introduction

Photodynamic therapy (PDT) is a targeted cancer treatment that utilises the toxic reaction between specific wavelengths of light, a photosensitiser that selectively accumulates within cancer cells and the molecular oxygen present in the tissues at the treatment area[3]. PDT is used or being investigated for use within many areas of oncology such as for skin[91], head and neck[92], bladder[93], lung[94], esophageal[95] and brain cancers[96, 97]. The content presented in chapter 4 employs a unified algorithm for photodynamic therapy (PDT) in conjunction with a Monte Carlo radiative transport (MCRT) code to explore the potential of intraoperative PDT in glioblastoma treatment. This section outlines the integration of the PDT simulation within the MCRT code introduced in chapter 4.

3.2.1   PDT background

One of the first noted instances of cell death via photosensitisation was in 1900 when a medical student accidentally killed some paramecium cells by treating them with acridine red and exposing them to light[98]. Seventy eight years later in 1978, the first human clinical trials began for PDT treatment of skin lesions and a few years after this, clinical trials began for the treatment of brain tumours with PDT[99]. In early clinical trials, such as the trial for balloon based intraoperative PDT by Muller et al., the goal was to determine if PDT

71

was more effective than other treatments at increasing the overall survival of the patient. The outcome was positive for increasing survival; however, due to the poor selectivity of early photosensitisers, there was a high risk of side effects such as unwanted damage to healthy cells[100]. As a result, PDT is not a widely used treatment for brain tumours today. However, the recent FDA (USA) approval of the highly selective photosensitiser Protoporphyrin IX (PpIX) for use within the brain has seen higher success rates when using PpIX to treat brain tumours via PDT in more recent clinical trials[101, 97, 102]. PDT has also already been accepted as a second-line treatment for glioblastoma tumours in Japan using Laserphyrin, a form of the photosensitiser Talaporfin[96].

3.2.2 Photosensitisers

The success of PDT is hugely dependent on the effectiveness of the photosensitiser used. As a result, a large part of the research effort for PDT has focused on creating a sensitiser that is as close as possible to the ideal. An 'ideal' photosensitiser has the following characteristics:

- A well-defined chemical composition with no impurities

- Only cytotoxic when exposed to light

- Selectively accumulates only in the targeted cells

- Leaves the body quickly to minimise toxicity

- A high quantum yield for the relevant photochemical reaction

- A strong absorption coefficient within the wavelength range where light propagation through tissue is highest[103]

The development of photosensitisers can be split into three generations. First-generation photosensitisers were generally porphyrin-based compounds with absorption peaks at around 400 nm. One of the most successful of these to be approved was Hematoporphyrin Derivative (HpD) and was chosen due to the fact that it was known to selectively accumulate in cancerous cells[104]. Although HpD was approved and successfully used in many cases, it did not fully meet the standards set out above. For example, when used to treat skin cancer, it was found that HpD did not leave the body very quickly and, as a result, left patients' skin sensitive to sunlight for several weeks after treatment[105]. The tumour selectivity of HpD also turned out to be poorer than thought[106], increasing the risk of damage to healthy surrounding tissue.

Second generation photosensitisers were developed to overcome some of the limitations

of the first generation. Their activation wavelengths are generally 600nm or more and they are more efficient at producing highly reactive singlet oxygen. PpIX is an example of a successful second generation photosensitiser and is currently widely commercially available in the form of its precursor, 5-Aminolevulinic acid (5-ALA)[104, 101]. PpIX photobleaches very quickly and is highly selective to tumour cells, making it a much safer photosensitiser than the first-generation examples as, even if normal cells do accumulate minute concentrations of PpIX, it will likely not be enough to kill them via phototoxic effects, even when exposed to high fluences of light[101]. This makes PpIX very suitable for treating brain tumours, where protection of the surrounding healthy tissue is paramount.

Third-generation photosensitisers are currently under development, and so far, very few have been approved for clinical use in humans. Compared to second generation photosensitisers, they have improved selectivity to cancerous cells. One example of third-generation photosensitisers under development is nanoparticle photosensitisers. They use targets such as antibodies, peptides and aptamers to directly deliver drugs to tumour cells. One issue with currently approved photosensitisers, as well as chemicals in other treatments such as chemotherapy, is their lack of ability to pass the protective blood brain barrier (BBB). This often restricts treatments to higher-grade tumours, around which the BBB has deteriorated[104]. However, nanoparticle photosensitisers have enhanced cellular uptake in tumour cells which may help to overcome this problem[107]. Another issue with current photosensitisers is the low penetration depth achievable in the brain by the wavelengths needed to activate them. As a solution to this, upconverting nanoparticles are being developed that can absorb several photons of lower energy light with higher penetration depths and emit higher energy photons that can be used for PDT[108].

3.2.3 PpIX synthesis

As mentioned above, when using PpIX as a photosensitiser, it is first administered in the form of its precursor compound 5-ALA which is used to synthesise PpIX. The synthesis pathway of PpIX is one that occurs naturally in the cytoplasma of most cells and involves combining eight 5-ALA molecules to produce the PpIX molecule. PpIX is normally combined with ferrous iron (Fe^{2+}) to form a haem molecule, an important part of haemoglobin. A diagram illustrating this synthesis pathway can be seen in figure 3.1. The full reasons for why PpIX selectively accumulates in cancer cells after 5-ALA administration are not fully understood and may even depend on factors such as tissue type and genetic differences between cancerous and healthy cells. Within the brain specifically, several factors such as the increased permeability of the BBB around malignant cells as well as reduced ferrous iron availability and reduced enzyme (ferrochelatase (FECH)) and transporter(ABCB6 or ABCG2) activity are all thought to contribute to the accumulation selectivity[101].

By administering further 5-ALA, allowing PpIX to build up in the cancer cells, the con-

centration can become high enough to cause phototoxic effects when exposed to specific wavelengths and fluences of light.
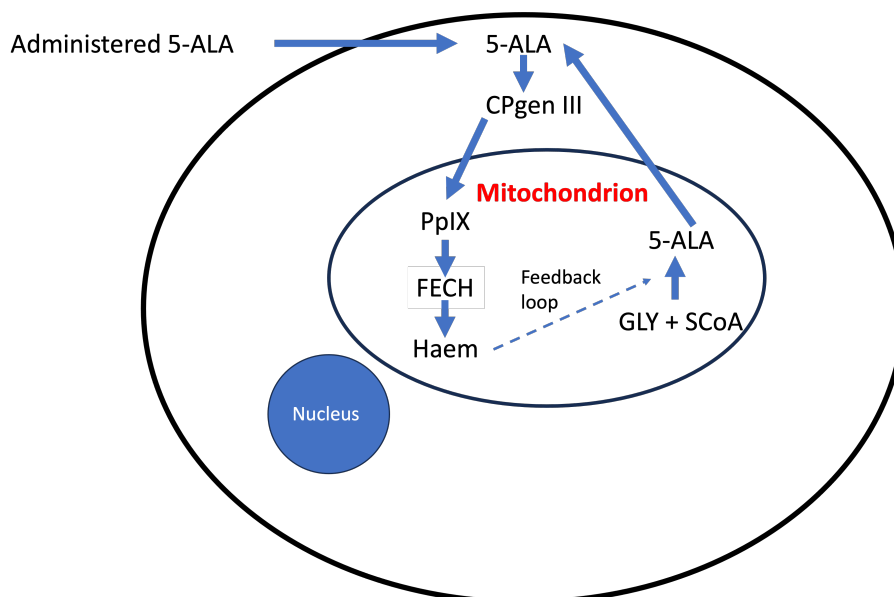
Figure 3.1: The simplified synthesis pathway of haem within a cell. Eight 5-ALA molecules are combined to form Coproporphyrinogen III (CPgen III) which leads to the formation of PpIX in the cells mitochondrion. The enzyme FECH is used to combine PpIX with iron to form haem. A feedback loop based on the amount of haem present results in further 5-ALA production from glycine and succinyl-coenzyme A (GLY + SCoA) if more haem is needed and inhibits 5-ALA production otherwise. The combination of more 5-ALA being added to the cell and shortages of FECH enzyme activity in cancer cells lead to a localised PpIX accumulation.

3.2.4 Light delivery

After the cancer cells have been successfully photosensitised, the next stage is delivering light to the cells. Within this work, light fluence (LF) refers to the total fluence of light delivered over time as described in equation 3.1 where $\Psi(i, j, k)$ is the fluence rate at position (i, j, k) and t is the total time.

$$\text{LF} = \Psi(\text{i}, \text{j}, \text{k})\text{t} \tag{3.1}$$

It is critical to the success of PDT that light is delivered to all malignant cells and is strong enough in dose to cause the desired cell death. There is a wide range of light sources available for PDT; the choice of which to use depends on two main factors: the depth of the

target cells (penetration depth needed) and the absorption wavelength of the administered photosensitiser. For PDT to be successful, the light source must be selected so that an appropriate light fluence at the correct depth can be achieved. The method of light delivery is one of the few fully controllable steps in PDT and so can be manipulated in order to get as close as possible to the best depth and light fluence for the required treatment[109, 110]. However, only ensuring that the correct energy and wavelength of light get to the correct place is not enough when planning a PDT treatment. Two additional factors, an adequate photosensitiser concentration and an adequate oxygen concentration, are also required for PDT to be successful. It is therefore important to use a treatment planning system that incorporates all three of these factors in order to be able to better predict or control the treatment outcome[111]. A system that also considers the extend of damage to the surrounding healthy tissue, or the general responsively of the treatment area to PDT would also be beneficial. Delivering light to the brain poses further challenges than to external areas and a balance normally needs to be found between minimal invasion and effective treatment.

Sources such as argon-dye lasers or xenon arc lamps have been commonly used for PDT in the past. Monochromatic lasers were used to activate photosensitisers with one strong peak while the broadband arc lamps were used to take advantage of photosensitisers that had more than one large absorption peak. Around the year 2000, diode lasers were developed and approved for PDT and have continued to be successful today. Currently, LED arrays are being developed for use in PDT. Their benefits include high power, narrow spectrum and low cost, making them a viable laser alternative[112, 109, 110].

3.2.5   PDT Reaction

Figure 3.2 presents a simplified Jablonski diagram of the photo-reactions that occur when a photosensitiser molecule (PS) is exposed to specific wavelengths of light. The energy of a photon of light can be calculated from its wavelength using equation 3.2 where h is Planck's constant, c is the speed of light within a vacuum and λ is the wavelength of the light.

$$E = \frac{hc}{\lambda} \tag{3.2}$$

If the energy of a passing photon matches the energy difference between two states of the photosensitiser molecule, it can be be absorbed, causing the photosensitiser to move from its ground state (^1PS) into a singlet excited state ($^1PS^*$). A molecule may have several excited states giving it the ability to absorb multiple wavelengths of light. We can see from the absorption spectra in figure 3.3 that the photosensitiser PpIX reacts to wavelengths of light around 410 nm, 510 nm , 545 nm , 580 nm and 635 nm, meaning photons at these
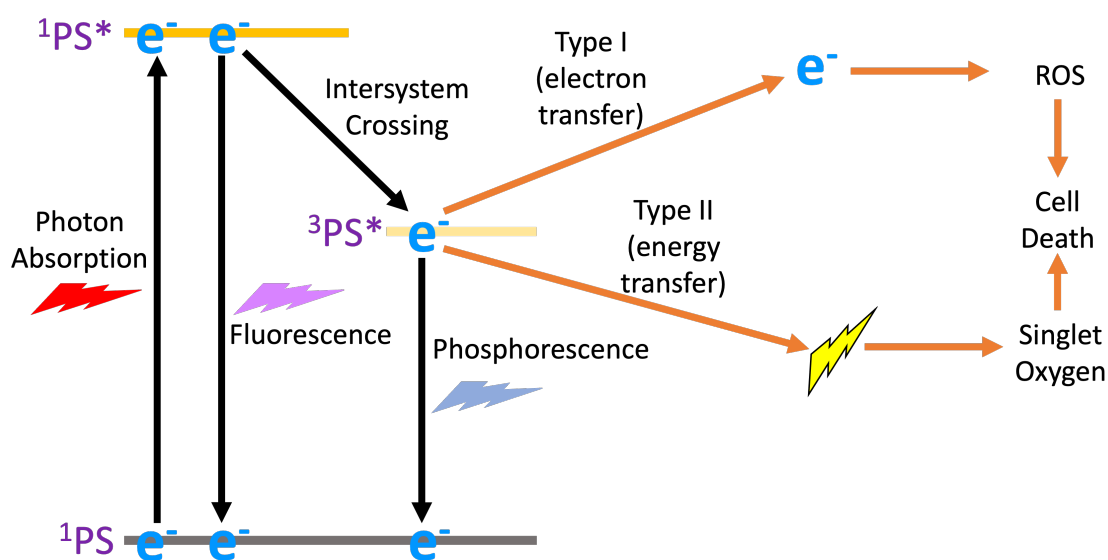
Figure 3.2: Simplified Jablonski diagram showing reactions of a photosensitiser (PS) molecule that occur when exposed to the correct wavelengths of light. When a photon is absorbed, the PS moves from its ground (^1PS) state to an unstable singlet excited state ($^1PS^*$). This results in either energy being released (fluorescence or heat) putting the PS back to its ground state or intersystem crossing, putting the PS into a more stable triplet excited state ($^3PS^*$). Once in the triplet excited state, the PS molecule can react with its surroundings in either a type I reaction which involves electron transfer and the production of ROS, or a type II reaction which involves energy transfer and the production of singlet oxygen. Both singlet oxygen and ROS can damage surrounding cells, causing them to die[3].
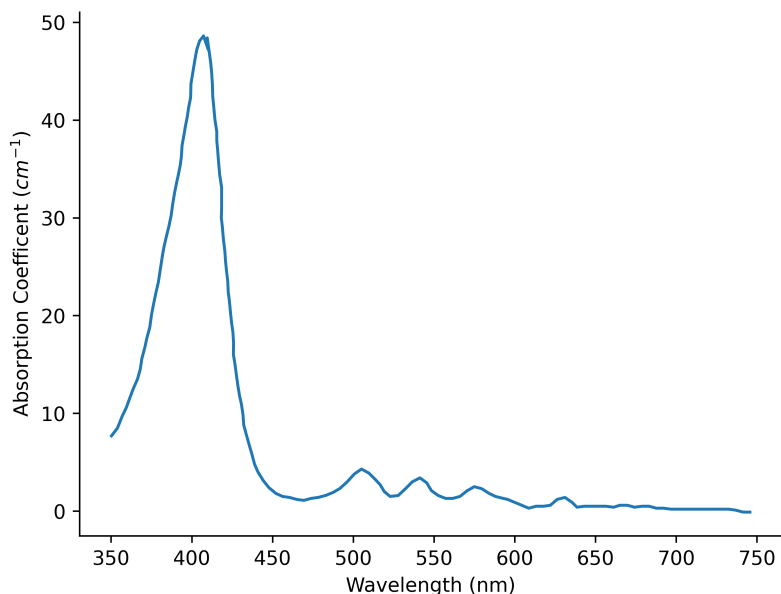
Figure 3.3: Absorption spectra for PpIX[115]

wavelengths match the energy difference between PpIXs ground and excited states. The singlet excited states are generally unstable and so may quickly decay directly back to the ground state by releasing extra energy as light or heat (see figure3.2). If the energy is released as a photon, this is called fluorescence. PpIX strongly adsorbs light at 405 nm and emits fluorescence at a peak of 634 nm[113]. This makes photosensitised brain tumours emit pinkish light and is used as a tool during fluorescence-guided surgery (FGS) to improve tumour margin detection and maximise surgical removal[114]. The excited state may instead undergo inter-system crossing and convert into a more stable triplet excited state ($^3PS^*$). This state can either decay back to the ground state by releasing light in the form of phosphorescence or, due to its longer lifetime, can react with surrounding molecules in either a type I or type II reaction. Type I reactions occur if the triplet state molecule reacts with some kind of substrate in the surroundings such as a cell membrane and undergoes an electron transfer. This results in the formation of free radicals which can react with oxygen molecules, leading to the production of reactive oxygen species (ROS), which are types of radical ion with the ability to damage cells. The predominant reaction within PDT however is the type II reaction. This is where the excited triplet state interacts with oxygen molecules directly, transferring energy to them and leading to the production of singlet oxygen, a very reactive molecule with the potential to interact with and damage many different biological substrates[3].

3.2.6 Cell death mechanisms

PDT can lead to tumour cell death through several different mechanisms. The combination of mechanisms that occur can vary between different treatment scenarios[3, 101].

Apoptosis and necrosis

Apoptosis and necrosis are induced by damage to the tumour cells caused by the ROS and singlet oxygen produced in the reactions discussed above. Necrosis is where the cell dies due to extensive, direct damage to several parts of the cell causing the cell membrane to break down and resulting in the release of cytoplasmic content. As a result, it leads to localised inflammation. Apoptosis however occurs when damage to a specific part of the cell, such as the DNA, leads to the cell triggering a death response. This results in the cell being broken down in a way that keeps the membrane intact and does not lead to any cytoplasmic leakage, meaning no inflammation response occurs[3, 101]. It should be noted that the distance that singlet oxygen can travel from its point of creation is $< 0.02\mu$m, making its toxic effects localised to the area of photosensitiser accumulation[116].

Inflammation

When the cells die as a result of necrosis, the resulting inflammation can cause an immune response to be triggered. This can lead to antibodies being produced that specifically target the tumour cells for a long period of time. It should be noted though that PDTs immunological mechanisms are not yet fully understood[3, 101, 117].

Vascular damage

As part of the targeted tumour, the endothelial cells within the tumours vascular system can also accumulate photosensitiser and be killed by damage caused by ROS and singlet oxygen. This can lead to the tumour being cut off from oxygen and nutrients, leading to further cell death[3]. Localised increased permeability of the BBB is also a sign of PpIX accumulation in endothelial cells[101].

3.2.7 Oxygen

As mentioned above, oxygen is one of the three vital components needed for successful PDT and we can now see from section 3.2.5 that this is due to the necessity of oxygen in the formation of singlet oxygen. This makes the availability of oxygen a limiting factor within PDT treatment. High treatment light fluence rates, for example, can lead to the consumption rate of oxygen by PDT becoming larger than the oxygen supply rate. This can lead to oxygen depletion around the treated area, halting the production of singlet oxygen and heavily reducing the therapeutic effect[3]. To help reduce the negative effects of oxygen depletion, some studies use light 'fractionation' where the treatment irradiation

time is split into several parts and rest periods are inserted between them where the light is switched off, allowing oxygen levels to recover[3]. This has been shown to improve the efficacy of PDT in several studies in skin[118, 119]. However, this improvement in PDT efficacy with fractionated light may not be universal to all treatment areas as no improvement was seen by van den Boogert et al. when treating the oesophagus with ALA-PDT[120]. In the case of glioblastoma tumours, due to their complex vasculature, tumour oxygenation is very heterogeneous even before PDT takes place, making PDT treatment efficacy vary across the tumour[101]. However, Leroy et al. found that a fractionated PDT treatment scheme increased the rate of cell apoptosis when treating human glioblastoma U87 cells that were grafted onto a mouse model[121]. Although it should be noted that U87 is a long established cell line and will therefore be less heterogeneous than natural GBM cells within a human.

3.2.8 Photobleaching

The accumulated concentration of PpIX is another limiting factor within PDT due to the fact that it is 'used up' during the process. Although theoretically a PpIX molecule might continually jump between ground and exited states, resulting in the production of ROS or singlet oxygen as described above, in reality it is often destroyed or changed in the process, resulting in the loss of its photosensitising properties. This could either be due to changes that occur to the molecule when transferring energy to an oxygen molecule or to damage caused by the produced ROS or singlet oxygen interacting with and damaging the PpIX molecule[122]. This reduction in the concentration of viable PpIX after activation is called photobleaching.

3.2.9 Future developments

As mentioned earlier, one future goal of PDT research is to develop a clinically approved nanophotosensitiser that can penetrate the BBB more easily as well as upconverting photosensitisers that aid deeper penetration of light[104]. Other studies, such as one by Wang et al.[123], are looking at using nanoplatforms for 5-ALA. These are shown to increase the concentration of PpIX that accumulates in the tumour cells as well as improve the level of oxygen supplied to the cells. Other research is looking to reduce the need for invasive operations by making cells produce their own PDT light via bioluminescence, chemiluminescence or Cerenkov radiation[124]. Other studies are looking at increasing the immune response that PDT naturally induces. If studied further, scientists think it could potentially be a viable treatment option or even be used to develop a vaccine for the prevention of brain tumours[125]. A recent study by Sun et al.[126] has shown there to be several barriers for this option due to treatment side effects and the fact that the environment that a brain tumour is in is often immunosuppressive, but it also suggested potential methods for overcoming these barriers[101].

MCRT/modelling application to PDT

Monte Carlo simulations can be used to simulate the intricate dynamics of PDT. They can produce a deeper understanding of the light distribution, absorption, scattering, and subsequent reactive oxygen species generation, which are fundamental to the therapeutic outcome. By varying parameters such as photosensitiser concentration, and light source characteristics, Monte Carlo simulations can provide insights into optimal treatment strategies, aiding in the development of more effective and personalised PDT protocols. This approach not only reduces the need for extensive and costly *in vivo* experiments but also accelerates the refinement of PDT techniques, ultimately enhancing its clinical applicability in treating various forms of cancer. Several MCRT/PDT models have already been developed. For example, Campbell et al.[8] used Monte Carlo combined with a fluence rate based PDT algorithm developed by Jacques et al.[127] to model the effectiveness of daylight PDT in different weather conditions. More recently, Wang et al.[10] have developed an open source software package that allows users to plan PDT treatments using the Monte Carlo software FullMonte and a PDT package named PDT-SPACE.

3.3 Jacques PDT method and validation

Before inserting our own models into the MCRT code described in chapter 1, it was important to first validate the accuracy of the code by using it to reproduce previous results. Using Monte Carlo simulations, Jacques et al.[127] developed mathematical functions to describe the penetration depth of 630 nm light into rat skin and the resulting escaped fluorescence at 705 nm. Their work goes on to develop an algorithm for estimating the resulting PDT effect based on a uniform PpIX concentration. Our goal was to reproduce Jacques et al.'s work within our MCRT code in order to validate the fluence rates produced and to insert a validated PDT algorithm that could be used to estimate PDT effect within our own models. The validation done first by using the optical properties of rat skin described by Jacques et al. to reproduce their calculated fluence rate of both 420 nm and 630 nm light. The escaped and observed fluorescence is also simulated and compared to Jacques et al.'s results. Finally, the PDT effect is validated by calculating the number of photons absorbed at each depth for different simulation times and comparing this to Jacques et al.'s results.

3.3.1 Theory

Fluence rate

Using measurement results from their MCRT code, Jacques et al. developed equations 3.3 and 3.4 to describe the penetration depth (or fluence rate) of the excitation light ($\Psi(z)$)

λ (nm)	C_1	C_2	C_3	k_1	k_2	k_3	μ_a (cm^{-1})	μ_s (cm^{-1})	δ (cm)
420	5.76	1.31	-	1.00	10.2	-	1.8	82	0.047
630	6.27	1.18	-	1.00	14.4	-	0.23	21	0.261
705	-	-	0.771	-	-	0.994	0.23	17	0.290

Table 3.1: Optical properties of rat skin and fitting parameters used in equations 3.3 and 3.4 [127].

and the escaped fluorescence emission ($E(z)$) from a depth of z.

$$\Psi(z) = \Psi_0(C_1 e^{(\frac{-k_1 z}{\delta})} - C_2 e^{(\frac{-k_2 z}{\delta})}) \tag{3.3}$$

$$E(z) = C_3 e^{\frac{-k_3 z}{\delta}} \tag{3.4}$$

Here Ψ_0 is the irradiance of the treatment light at the surface with units W/cm^2. C_1, C_2, C_3, k_1, k_2 and k_3 are wavelength dependant fitting parameters described in table 3.1. Finally, δ is the optical penetration depth described by equation 3.5. Values for δ as well as the absorption coefficients (μ_a) and scattering coefficients (μ_s) are also found in table 3.1.

$$\delta = \frac{1}{\sqrt{3\mu_a(\mu_a + \mu_s(1-g))}} \tag{3.5}$$

PDT

Once the fluence rate is simulated, Jacques' calculations go on to estimate the PDT effect. This starts by modelling the reduction in the concentration of PpIX over treatment time due to photobleaching. Assuming an initial uniform concentration of photosensitiser PpIX (C_0), the concentration at each z depth is recalculated after every time step using equation 3.6 where t is the total treatment time in seconds and Γ is the photobleaching time constant.

$$C(z,t) = C_0 e^{\frac{-t}{\Gamma}} \tag{3.6}$$

Γ is calculated using equation 3.7 where D is the photobleaching dose constant (table 3.2), dependent on the photobleaching wavelength (630 nm) and $\Psi_b(z)$ is the fluence rate of the photobleaching light at depth z.

$$\Gamma = \frac{D}{\Psi_b(z)} \tag{3.7}$$

The level of fluorescence detected during PDT is often used to monitor the progress of the treatment due to the fact that it decreases as the PpIX is used up[3]. Jacques et al. model

the level of fluorescence observed over treatment time ($F(t)$) using equation 3.8 where $\Psi_{ex}(z)$ is the fluence rate of the fluorescence excitation light at depth z, ϵ is the wavelength dependent excitation coefficient (table 3.2), Φ is the fluorescence quantum yield assumed to be 1 and f is the collection efficiency of the fluorescence measurement setup, also assumed here to equal 1.

$$F(t) = \int_0^\infty \Psi_{ex}(z)\epsilon C(z,t)\Phi E(z)f dz \tag{3.8}$$

The photodynamic dose (PD), is defined as the number of photons absorbed by the photosensitiser per unit volume. It can be calculated as the product of photosensitiser concentration, absorption coefficient and fluence rate. The photodynamic threshold dose is then defined as the PD needed before necrosis occurs[128]. To help predict the PDT outcome, Jacques et al. calculates the PD as the number of photons absorbed by PpIX per cm^3. They describe the PD using equation 3.9 and define a threshold PD of 8.6×10^{17} photons/cm^3[127, 33].

$$PD(z,t) = \frac{\lambda}{hc}\epsilon C_0 D(1 - e^{\frac{-\Psi(z)t}{D}}) \tag{3.9}$$

λ (nm)	ϵ (cm^{-1}(μg/ml)$^{-1}$)	D (J/cm^2)	C_0 (μg/ml)	L_0 (W/cm^2)
420	0.105	105	0.2	0.1
630	0.0265	105	0.2	0.1

Table 3.2: Property values measured/chosen by Jacques et al. for simulation[127].

3.3.2 Simulation validation

To setup the MCRT code to reproduce the Jacques' equations, a grid with dimensions 2 cm $\times$ 2 cm $\times$ 2 cm was used containing 100 x 100 x 100 voxels. First the fluence rate from 630 nm and 420 nm sources was simulated. This was done by applying the relevant optical properties for absorption and scattering coefficients for each wavelength from table 3.1. The treatment light was assumed to be uniformly irradiated over the top of the grid with an irradiance of 0.1 W/cm^2.

Figure 3.4 compares the fluence rates obtained by the MCRT code to the Jacques function for fluence rate (eq. 3.3) for both 630 nm and 420 nm light sources. The fluence rates are normalised by the source irradiance (L_0).

Next the escaped fluorescence (E(z)) was simulated. The code was setup so that every 630
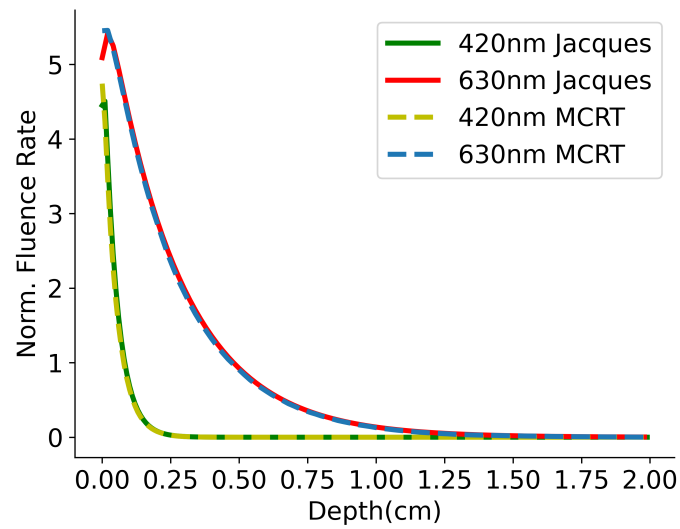
Figure 3.4: Plot comparing the normalised fluence rates found using the MCRT simulation to the function for fluence rate in skin (eq. 3.3) developed by Jacques et al.[127]. The plot shows results for both 420 nm and 630 nm light, with the MCRT and Jacques values matching well.
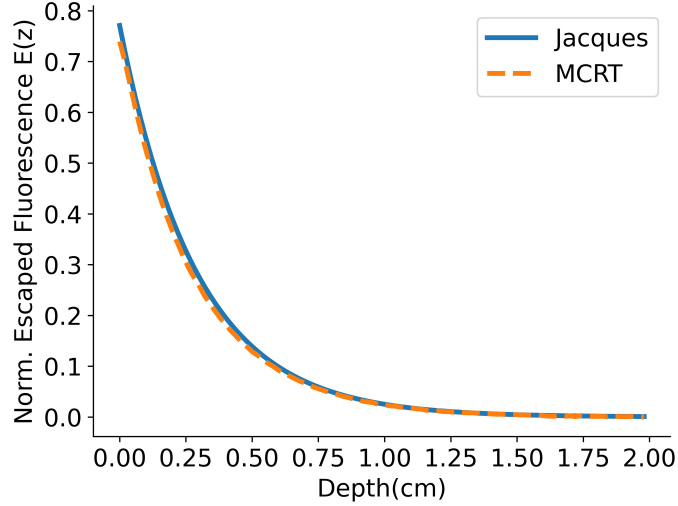
Figure 3.5: Plot comparing the normalised escaped 705 nm fluorescence as a function of z-depth obtained using the MCRT simulation against the function (eq. 3.4) developed by Jacques et al.[127]. The results are normalised against the 630 nm absorption rate at each depth.

nm power packet absorption resulted in the isotropic emission of a 705 nm power packet at the same position. In the interest of computational efficiency, all 630 nm power packets were run before switching the grid optical properties to those corresponding to 705 nm (table 3.1) and running each of the 705 nm power packets from their respective positions. This stopped the code from having to constantly redefine the grid properties. The escaped fluorescence was measured by counting the number 705 nm power packets leaving through the top of the grid from each z-depth.

Figure 3.5 compares the normalised escaped fluorescence found using the MCRT to the escaped fluorescence function developed by Jacques et al. (eq. 3.4). The results are normalised against the total number of 630 nm power packets absorbed at each z-depth and match Jacques et al.'s predicted results well.

To simulate the observed fluorescence over time, the code had to be adapted first to become time dependant, then to incorporate the photobleaching of PpIX. Time dependence was added by placing the full MCRT and fluorescence portion of the code into a loop. The code was re-run using the same number of power packets for each loop iteration and the total illumination time (t) increased by 1 second each time. The photobleaching of PpIX was simulated by recalculating the concentration of PpIX ($C(z,t)$) at the end of each time
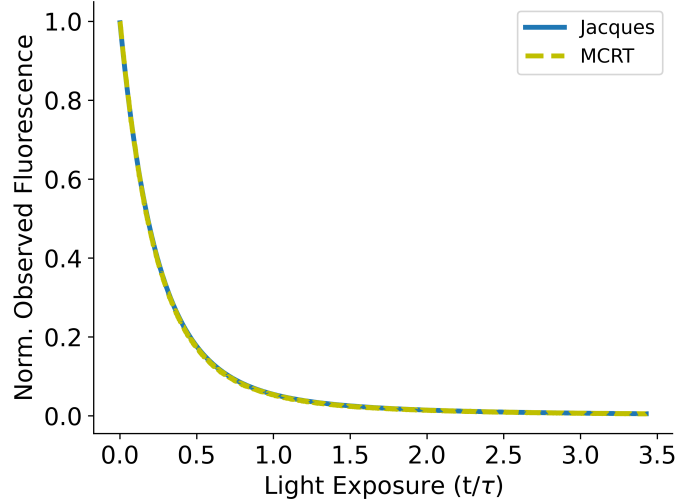
Figure 3.6: Plot comparing the normalised observed fluorescence as a function of light exposure (t/Γ)(eq. 3.7) when running the MCRT code with 630 nm irradiation light to the observed fluorescence function (eq. 3.8) developed by Jacques et al.[127]. The results are normalised by the observed fluorescence value at t = 0.

step using equation 3.6. A PpIX concentration of 0.2 μg/ml was applied to each voxel at the start of the simulation[127]. It was assumed that the addition of PpIX did not impact the fluence rate due its negligible absorption at these concentrations[33]. The absorption added by PpIX at 630 nm can be calculated by multiplying ϵ by C_0 from table 3.2. This results in an additional, negligible absorption of 0.0053 cm^{-1}. The observed fluorescence was measured by counting the number of 705 nm power packets leaving the top of the grid over each loop iteration.

Figure 3.6 compares the normalised observed fluorescence when using a 630 nm source as the excitation light to Jacques et al.'s observed fluorescence function (eq. 3.8)[127]. The results are normalised to the level of fluorescence observed at time t = 0 and match the predicted results well.

Finally, the change in photodynamic dose (PD) over time could be simulated. As mentioned above, the PD is defined as the number of photons absorbed by PpIX per cm^3. To calculate the change in PD over every time step, the number of photons absorbed by PpIX needed to be calculated using the total energy absorbed per second(ΔQ_{PpIX}). The energy absorbed by PpIX per cm^3 is calculated using equation 3.10 where A is the total area of irradiance (cm^2), $\mu_{a,\text{PpIX}}$ is the absorption coefficient of PpIX (0.032 cm^{-1} at 630 nm[99]), l (cm)

is the total path-lengths of all power packets passing through voxel (i, j, k) over the time step, N is the total power packets run per time step and ΔV is the voxel volume (cm^3).

$$\Delta Q_{\mathrm{PpIX}}(i, j, k) = \frac{\psi_0 A \mu_{a,\mathrm{PpIX}} l(i, j, k)}{N \Delta V} \tag{3.10}$$

This energy is converted into a number of photons by dividing it by the energy of a photon (b $= \frac{hc}{\lambda}$), where λ is the wavelength of the photon (630 nm), h is Planck's constant and c is the speed of light in a vacuum. The change in PD per time step (Δt) within each voxel was calculated using equation 3.11.

$$\Delta PD(i, j, k) = \frac{\Delta Q_{\mathrm{Ppix}}(i, j, k) \Delta t}{b} \tag{3.11}$$

The total PD within each voxel was calculated by summing up all the ΔPD contributions over time (eq. 3.12).

$$PD(i, j, k, t) = \sum_t \Delta PD(i, j, k) \tag{3.12}$$

Figure 3.7 compares the total PD from 630 nm light obtained using the MCRT simulation to the results obtained using the Jacques PD function(eq. 3.12)[127]. The results are plotted for total irradiation times of 1-10 minutes in steps of 1 minute then 20-60 minutes in steps of 10 minutes. The cell kill threshold dose of 8.6×10^{17} photons/cm^3 is marked on the plot by the black horizontal line. We can see that the MCRT results and the Jacques predicted results again match well at each time.

3.4 Wang PDT method and validation

While models that predict PDT outcome based on the absorption of light by a photosensitiser, such as the Jacques model described above, work well in well oxygenated conditions, their accuracy deteriorates when lower oxygen concentrations (hypoxia) occurs. Solid tumours, such as glioblastoma, tend to have heterogeneous oxygenation[129], resulting in hypoxia in some parts before treatment begins. Even when hypoxia is not already present however, high fluence rate PDT setup have been shown to induce hypoxia[130], lowering the effectiveness of PDT. A PDT algorithm that also takes oxygen concentration into account is therefore necessary to gain a more accurate prediction of treatment outcome[131].

In their work, Wang et al.[131] developed a mathematical model to describe PDT. Like the Jacques model, it incorporated fluence rate and photosensitiser concentration. However, it also included oxygen dynamics, modelling both the metabolic oxygen supply and usage as well as the production of singlet oxygen within the type II reactions described in section 3.2.5. The outcome of the model was an 'apparent reacted singlet oxygen concentration'
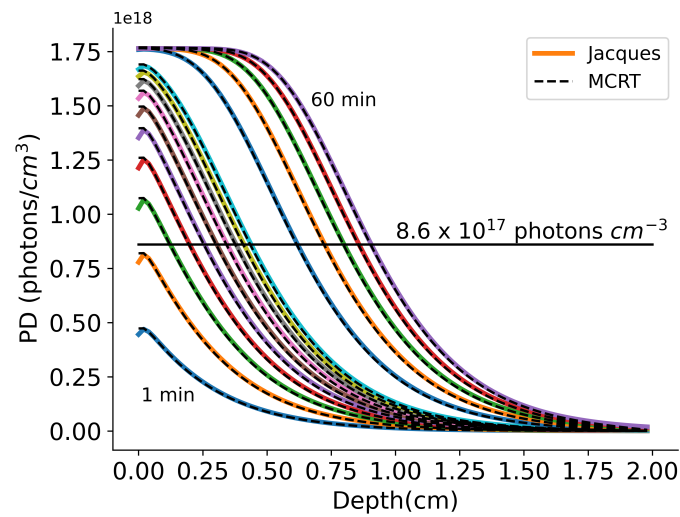
Figure 3.7: Plot comparing the total PD at each depth found using the MCRT simulation and the function developed by Jacques et al.(eq. 3.12)[127]. The PD is plotted for the times of 1-10 minutes in steps of 1 minute and 20-60 minutes in steps of 10 minutes. The point where the PD reaches the cell kill threshold of 8.6×10^{17} photons/cm^3 is marked by the horizontal black line.

which, along with estimates of a singlet oxygen concentration threshold, can be used to predict PDT cell kill via necrosis.

3.4.1   Theory

Wang et al.'s PDT algorithm[131] is comprised mainly of three, fluence rate dependant, differential equations that describe the change to photosensitiser concentration, triplet oxygen concentration and reacted singlet oxygen concentration over an irradiation time. The oxygen transport part of the algorithm was developed using the Krogh cylinder model. This is a simplified theoretical model used to describe oxygen transport in tissues. It assumes that oxygen is delivered to the tissue solely through parallel, equally spaced cylindrical capillaries, as shown in figure 3.8, with oxygen diffusion occurring at a constant rate, radially outward from the capillary into the surrounding tissue[132].

Fluence rate

The PDT model starts by using the light diffusion equation to define a fluence rate (ψ) based on the light source used and optical properties of the chosen medium. This is shown in equation 3.13 where S is the source term.

$$\mu_a \psi - \nabla \cdot (\frac{1}{3\mu'_s}\nabla\psi) = S \tag{3.13}$$

All parameters used within Wang et al.'s PDT model equations are defined in the glossary at the beginning of this thesis.

Photosensitiser concentration

The change in photosensitiser concentration (C) over time is calculated using equation 3.14.

$$\frac{dC}{dt} + \xi\sigma\frac{\psi(C+\delta)[^3O_2]}{[^3O_2]+\beta}C = 0 \tag{3.14}$$

Triplet oxygen concentration

Next, the change in concentration of triplet oxygen is calculated using equation 3.15.

$$\frac{d[^3O_2]}{dt} + \left(\xi\frac{\psi C}{[^3O_2]+\beta}\right)[^3O_2] - \Phi(t)\left(1 - \frac{[^3O_2]}{[^3O_2]_{t=0}}\right) = 0 \tag{3.15}$$

Here, $\Phi(t)$ is the time dependant maximum oxygen supply rate, the calculation of which includes the metabolic consumption and replenishment of triplet oxygen. To account for
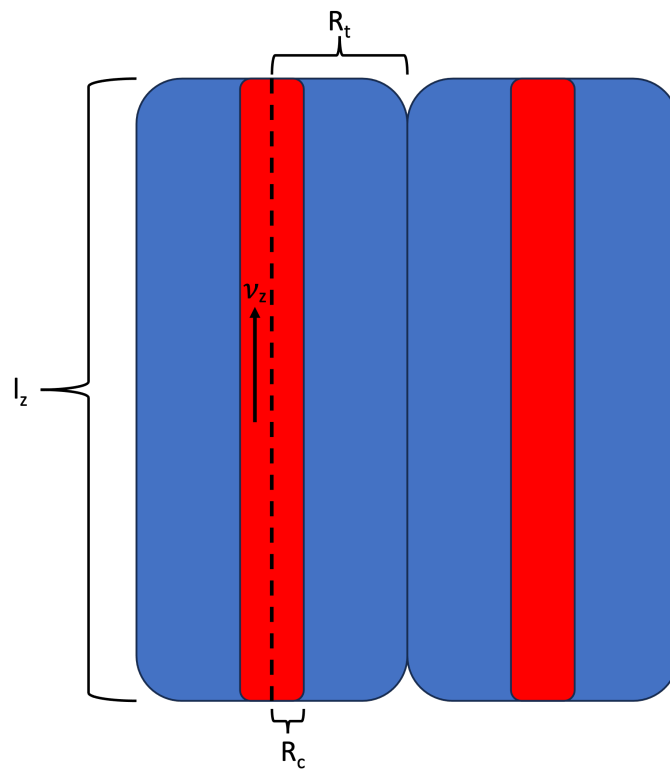
Figure 3.8: Diagram showing two adjacent Krogh cylinders with radii R_t and length l_z, each containing a capillary (red) of radius R_c. Blood flows through the capillaries at a constant velocity v_z[133] while oxygen diffuses radially outward from each capillary into the surrounding tissue.

changes to the blood flow during PDT, $\Phi(t)$ varies with time following equations 3.16 and 3.17 developed by Penjweini et al.[134].

$$\Phi(t) = \Phi_0 \frac{0.99t'^4 + 1.09t'^3 + 0.05t'^2 + 0.18t' + 0.32}{t'^4 + 1.16t'^3 + 0.18t'^2 + 0.24t' + 0.31} \tag{3.16}$$

$$t' = \frac{t - 750}{632.1} \tag{3.17}$$

Φ_0, is calculated using equation 3.18. The function, developed by Zhu et al.[133], uses the physical attributes of the capillaries at the treatment location (modelled using Krogh cylinders) along with an estimated maximum oxygen consumption rate, to calculate the net oxygen supply rate.

$$\Phi_0 = \frac{1200 v_z R_c \left(R_c + \frac{100^2 + q_0^2}{50^2 - q_0^2} \right)}{l_z (R_t + 4.2)^2} \tag{3.18}$$

Singlet oxygen concentration

Finally, the change in the concentration of reacted singlet oxygen over time is calculated using equation 3.19.

$$\frac{d[^1O_2]_{rx}}{dt} - \varrho \frac{\psi C[^3O_2]}{[^3O_2] + \beta} = 0 \tag{3.19}$$

A singlet oxygen concentration cell kill threshold value can be defined in order to estimate the level of cell kill and therefore the PDT treatment outcome. This value can vary between different tissue types and photosensitisers and ideally should be measured directly for each circumstance to gain a fully accurate estimation[131].

In vivo measurements

To quantify the parameters for their PDT model, Wang et al. performed _in vivo_ measurements on several mouse models with fibrosarcoma tumours[131]. They measured the tumour optical properties at 630 nm and the initial photosensitiser concentration (Photofrin) within each mouse before using a finite element method (FEM) code to solve equations 3.13-3.19. They calculated the fluence rate and the resulting change in photosensitiser, triplet oxygen and singlet oxygen concentrations.

Simulation validation

To incorporate and validate Wang et al.'s PDT algorithm with the MCRT code, it was used to reproduce the linear source results measured in one of their mouse models named mouse 3[131]. To set this up within the MCRT code, a voxel grid with dimensions 2 cm x

2 cm x 2 cm containing 100 x 100 x 100 voxels was used. The 630 nm optical properties measured by Wang et al. for mouse 3 ($\mu_a = 1.51\text{cm}^{-1}$, $\mu'_s = 12.29\text{cm}^{-1}$) were applied to the grid. The initial photosensitiser concentration was set (3.7 μM).

To simulate a cylindrical diffuser, a line of isotropic point sources was placed from the centre of the top of the grid to a depth of 1 cm. Wang et al. delivered a light power of 33 mW/cm to mouse 3, with a total delivered energy of 88 J/cm, corresponding to a treatment time of 44.4 minutes or 2667 seconds. As with the PDT simulation above, time dependence was simulated within the code by putting it within a repeating loop, where every iteration corresponded to 1 second.

Within the code, the fluence rate was simulated first using the standard MCRT methods described previously. Figure 3.9 plots the calculated fluence rate at a distance of 1 cm from the centre of the linear source along the x direction. The MCRT fluence rate is compared to the fluence rate that Wang et al. obtained using their FEM code. Both results match fairly well with a squared correlation coefficient of 0.91836, although the MCRT results show a larger fluence rate directly next to the linear source, which could either be due to differences in the calculation methods, such as different scattering phase functions.

Once the MCRT portion of the code is complete, the code was set to calculate the photosensitiser concentration, triplet oxygen concentration and singlet oxygen concentration by inserting the relevant values into equations 3.14 - 3.19. This is repeated for every loop iteration, or every second of treatment time and the final concentrations plotted along the same x-direction as the fluence rate and compared to Wang et al.'s results in figures 3.10, 3.11 and 3.12. We can see that the results match well in each case, with all squared correlation coefficients (r^2) valuing above 0.95. The MCRT triplet oxygen concentration is again larger at the source than Wang et al.'s, likely due to the same reasons as the larger fluence rate in figure 3.9.

3.5   Discussion

Due to the heterogeneous nature of glioblastoma tumours, as well as the importance of adequate oxygen level maintenance within the brain[135], it was deemed necessary to consider oxygen levels when modelling intraoperative PDT for the treatment of glioblastoma. The work covered in chapters 4 and 5 therefore uses Wang et al.'s algorithm for simulating PDT within a brain/glioblastoma model.

It should be noted here that Wang et al.'s model was chosen due to its simplicity to incorporate within the MCRT code; however, due to the fact that it is based on the Krogh
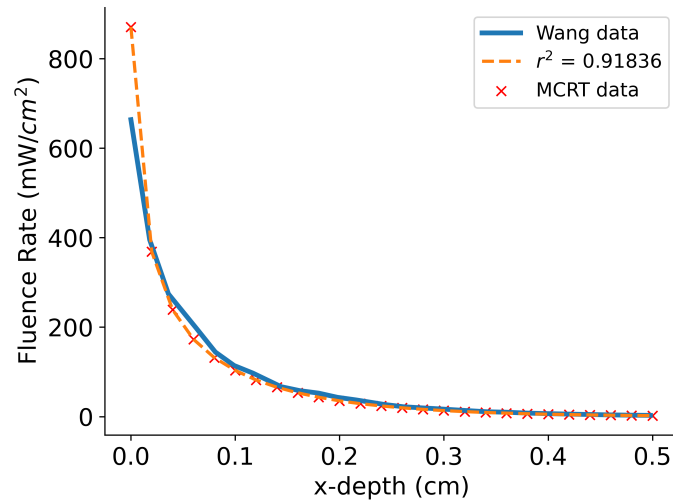
Figure 3.9: Plot comparing the radial fluence rate from a linear 630 nm, 33 mW/cm source in Wang et al.'s[131] mouse 3, calculated using Wang et al.'s FEM code, to the simulated MCRT data. The data matches well with a squared correlation coefficient (r^2) of 0.91836. The difference in fluence rate at the surface is likely due to differences in the scattering phase function between the two simulations.
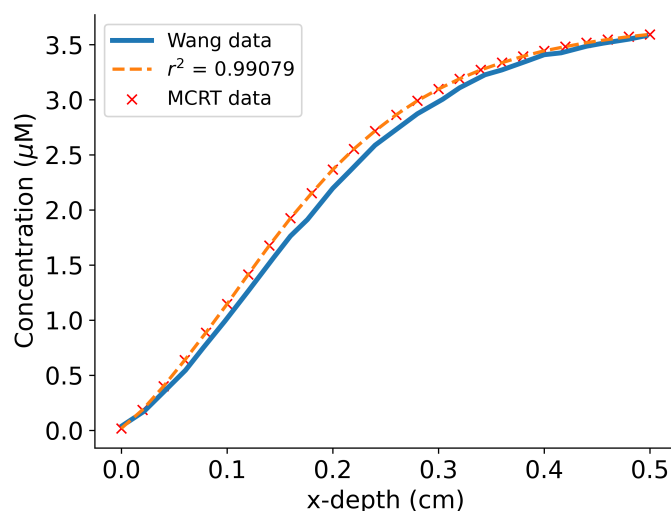
Figure 3.10: Plot showing the photosensitiser concentration with depth from the 630 nm, 33mW/cm linear source at the end of the 44.4 minute treatment time for Wang et al.'s mouse 3. Results from the MCRT simulation and Wang et al.'s FEM simulation are compared[131]. The data matches well with a squared correlation coefficient (r^2) of 0.99079.

cylinder model, using it for modelling oxygen transport within the brain has several downsides. As mentioned above, the Krogh cylinder model assumes that capillaries are evenly spaced and parallel. This is not the case for brain capillaries however which form a more complex mesh like network[136]. The model also assumes homogeneous blood flow velocity and oxygen consumption, both of which are generally variable throughout the brain[135]. Given these limitations, more sophisticated and realistic models, such as computational fluid dynamics (CFD) simulations or three-dimensional vascular network models, are preferred for studying oxygen transport in the brain. These models take into account the complex geometry of brain capillaries, blood flow dynamics, oxygen consumption heterogeneity, and other relevant physiological factors, providing a more accurate representation of oxygen transport in the brain[136]. However, they are also likely to be more complex and more computationally expensive, making the Krogh model a better starting point for this work which can be developed on in the future.

3.6 Conclusion

PDT has been shown to be an effective and targeted treatment for various forms of cancer. Computational modelling of PDT has many possible benefits, including, with further development, the potential to accurately pre-plan PDT treatments to optimise the treat-
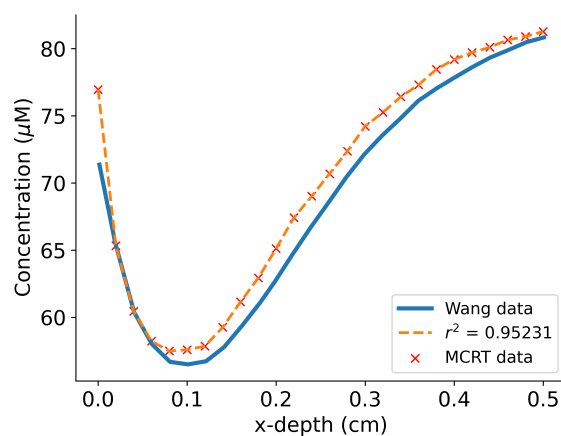
Figure 3.11: Plot showing the triplet oxygen concentration with depth from the 630 nm, 33 mW/cm linear source at the end of the 44.4 minute treatment time for Wang et al.'s mouse 3. The oxygen concentration is higher at the surface due to there being more oxygen availability from the surrounding environment. This then dips very low at the point where there is less triplet oxygen availability but still a high fluence rate. Finally it increases again as the fluence rate decreases. Results from the MCRT simulation and Wang et al.'s FEM simulation are compared[131]. The data matches well with a squared correlation coefficient (r^2) of 0.95231.
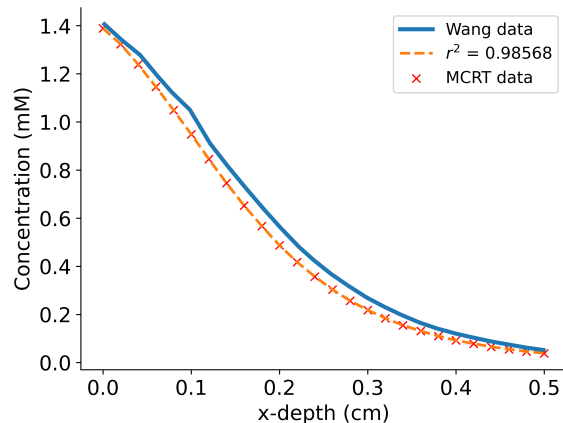
Figure 3.12: Plot showing the reacted singlet oxygen concentration with depth from the 630 nm, 33mW/cm linear source at the end of the 44.4 minute treatment time for Wang et al.'s mouse 3. Results from the MCRT simulation and Wang et al.'s FEM simulation are compared[131]. The data matches well with a squared correlation coefficient (r^2) of 0.98568.

ment outcome whilst minimising potential damage[7, 10]. Two PDT modelling schemes have been described and validated using the MCRT code. Theoretical validations were performed by reproducing previous results for both schemes. Based on the importance of oxygen within PDT and the brain, it was decided that the PDT algorithm developed by Wang et al.[131] would be used later when modelling intraoperative PDT for the treatment of glioblastoma (chapters 4 and 5).

Chapter 4

Intraoperative PDT for Glioblastoma

4.1 Summary

MCRT methods along with the algorithms for PDT modelling described in section 3.4, are used within this chapter to model intraoperative PDT for glioblastoma following the protocol of a recent clinical trial. By accurately employing the optical properties of brain tissue, including scattering and absorption, the MCRT model enables us to simulate the behaviour of light and its effect on photosensitiser activation and tumour cell destruction. Several of the trial protocol parameters such as light power, treatment time and photosensitiser concentration are modified in order to help optimise treatment parameters and predict therapeutic efficacy. The results indicate that increasing treatment time and light power predict moderate improvements to the treatment outcome when compared to the standard protocol; however tissue temperature increased as a result (This chapter does not look at tissue temperature variations. Please refer to Chapter 5 to see the full impact of the treatment on the surrounding tissue temperature.). The most significant improvement to tumour cell kill is seen when photosensitiser concentration is increased. The majority of work within this chapter was published in the *Journal of Biomedical Optics* in 2024[137].

4.2 Introduction

Glioblastoma is a highly aggressive and treatment resistant brain tumour with a current median survival rate of 14.6 months[104]. Maximal tumour resection has been shown to improve patient survival time[138] and so, with the recent FDA approval of PpIX mediated fluorescence guided surgery for brain tumours, there is interest in adding PDT to the standard glioblastoma treatment to help safely enhance tumour removal and improve patient prospects[104].

96

A realistic 3D model of a brain containing a glioblastoma tumour is implemented into the MCRT / PDT code 4.7 and adapted to simulate the intraoperative PDT treatment by reproducing the protocol of a phase I clinical trial (NCT04391062). The model is used to quantify the PDT effect by calculating tumour cell kill, enabling a direct comparison of therapeutic effect when modifying the treatment parameters. It is hoped that the information gained when using the simulation will aid the optimisation of PDT treatment for glioblastoma in the future.

4.3 The brain

4.3.1 Areas of the brain and their functions

The brain is formed from three main parts;

- The cerebrum

- The cerebellum

- The brainstem[139]

The locations of these parts can be seen in figure 4.1a.

The cerebrum

The cerebrum is the largest part of the brain and consists of two hemispheres. The right hemisphere is used for spatial thinking while the left hemisphere is used for abstract thinking and speech. While the brain consists of many different tissue types, the majority of the cerebrum is made up of white matter and grey matter. The outer layer, also known as the cerebral cortex, is made from grey matter while the inner 'subcortical' is made mainly from white matter.

The cerebrum is further split into 4 lobes;

- The frontal lobe

- The parietal lobe

- The temporal lobe

- The occipital lobe

The frontal lobe controls language and motor functions as well as processes like mood, personality, moral reasoning and speech. The parietal lobe is responsible for integration and processing of sensory functions such as sensory, hearing and visual interpretation. The
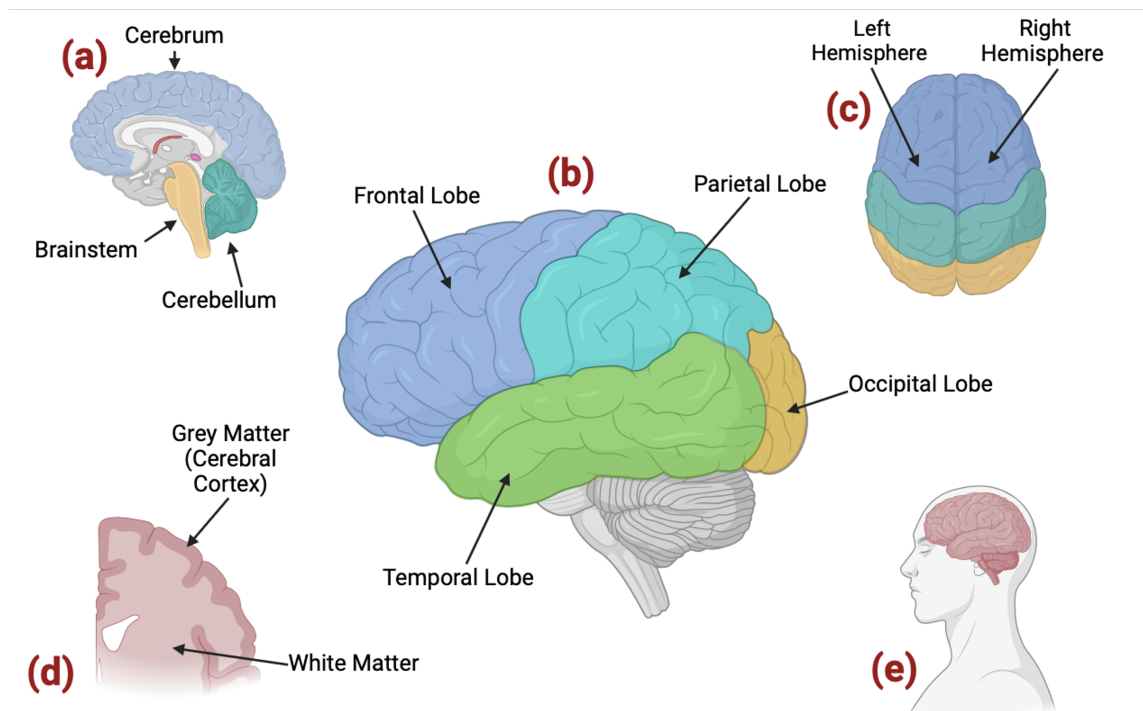
Figure 4.1: (a) Image highlighting the three main parts of the brain; the cerebrum, brainstem and cerebellum. (b) The four lobes of the cerebrum; the frontal lobe, parietal lobe, occipital lobe and temporal lobe. (c) Superior view of the left and right hemispheres. (d) Section of cerebrum showing the white matter core surrounded by a layer of grey matter (the cerebral cortex). (e) Image showing the orientation of the brain inside the head. (Created with BioRender.com)

temporal lobe processes auditory input, memory and emotion, which helps us to interpret written and spoken language. Finally the occipital lobe contains the visual cortex which functions to process visual information[139].

The cerebellum

The cerebellum again consists of a white matter core covered by a layer of grey matter[140] and its main function is to help control posture, balance and the coordination of conscious, voluntary movement[139].

The brainstem

The brainstem connects the cerebellum and the cerebrum to the spinal cord and is made of a mixture of white and grey matter[141]. It also contains parts of the brain responsible for involuntary functions such as breathing, heart function and digestion[139].

4.3.2 Brain tumours

Brain tumours come in many different types, dependant upon their cellular origin. The risk that they pose depends both on their specific location as well whether they are benign or malignant. Identifying and classifying brain tumours is complex but vital, due to the fact that each type will respond to treatments differently, making proper identification necessary for optimal treatment[142].

Tumour grades

In 1979, the world heath organisation(WHO) published the first edition of their 'Classification of Tumours of the Central Nervous System'. This has since been updated 5 times with the most recent update in 2021[143]. The classification system defined brain and spinal cord tumours into separate grades from I-IV which describe the tumours malignancy or benignity based on measurable histological features. Table 4.1 presents definitions of each grade. Note that the 2021 edition now takes into account molecular features, which are more closely related to prognosis than histology.

Tumour types

As well as the grades discussed above, brain tumours can also be separated into different types, dependant on the types of cells they originate from.

The most common type of CNS tumour are meningiomas, originating within the meninges, three layers of membrane that surround the spine and brain. These make up about 37 % of all diagnosed CNS tumours and about 50 % of those that are benign[145].

Grade	Features
I	• Most benign • Doesn't infiltrate • Very slow growing • May be fully treatable with surgery
II	• Benign • Mostly non-infiltrative • Slow growing • Chance of recurrence as a high grade tumour
III	• Malignant • Fairly infiltrative • Fast growth • Likely to reoccur as a higher grade
IV	• Most malignant • Very infiltrative • Very fast growing and aggressive • Reoccurs quickly • Necrosis may occur

Table 4.1: Table presenting the brain tumour classification system developed by WHO[144, 143].

The most common malignant tumours are gliomas which are diagnosed in 6 out of every 100,000 people in the US every year. They originate from cells within the brain called glia. There are three different types of glia cell which are astrocytes, ependymal cells and oligodendroglial cells. Gliomas can originate from one or a combination of these cell types[146].

Glioblastoma tumours are the most invasive type of glioma with a WHO grading of IV. They can be made from several types of glial cell, such as astrocytes and microglia and can be mixed with oligodendrocytes[147]. They can be located anywhere in the brain, but the majority of glioblastomas form within the cerebral hemispheres, specifically within the frontal and temporal lobes[148].

4.4   Current treatments for glioblastoma

The current standard of care for glioblastoma treatment follows the Stupp protocol, named after its creator, oncologist Roger Stupp. It involves maximal resection via surgery, followed by radiotherapy and temozolomide chemotherapy and resulted in a clinically significant increase in patient survival time when first used[149].

However, glioblastoma tumours remain incurable. The median time to tumour recurrence (progression free survival) after treating with the Stupp protocol is only a matter of months and median overall survival (time to death) only 15 months[150]. Glioblastomas usually contain glioma stem cells (GSC) which have unique molecular characteristics such as genetic heterogeneity and the ability to self-renew[151]. This essentially means that any GSCs that survive radio- and chemotherapy during the first treatment are able to rapidly proliferate into new radio and chemotherapy resistant cells, causing a fatal tumour recurrence[152]. Only a few GSCs are required for this to happen and the infiltrative nature of glioblastomas into surrounding brain tissue and along blood vessels make it almost certain that some will remain. There are also general difficulties when trying to treat brain tumours that apply to glioblastoma treatment, such as tumours being located in deep / eloquent areas of brain that are unsafe for a neurosurgeon to attempt complete / near complete resection. Furthermore, the inability for medications or immune cells to penetrate the blood brain barrier (BBB)[153, 154] makes adjuvant treatment relatively ineffective.

Thankfully, new research into the development of glioblastomas and the brain's microenvironment is constantly evolving and resulting in the development of potential new therapies for glioblastoma[155]. These therapies involve, for example, methods to disrupt the BBB to improve drug penetration[156] and research into immune therapies[157].

4.4.1 Photodynamic therapy for glioblastoma

Photodynamic therapy (PDT) is one treatment modality that has shown promise within the field of glioblastoma as it is able to overcome or improve several of the problems discussed in section 4.4. The idea of using PDT to treat glioblastomas was first explored in the 1980s[158]. However, while some positive effects on survival time were seen, it was soon discovered that the available photosensitisers at the time were not selective enough, causing a high risk of side effects due to healthy brain tissue damage and long lasting sensitivity to sunlight. More recently, new classes of photosensitisers with much higher selectivity, such as the recently FDA (USA) approved PpIX, have reopened the possibility of PDT as a viable treatment for gliomas[104] and resulted in its acceptance as a second line treatment for GBM in Japan[96]. However, given the lack of Class 1 evidence of efficacy against GBM, even experimental use elsewhere is still rare. Though, as Cramer et al.[104] and Mirreti et al.[153] point out, there are several clinical trials, past, present and future, aiming to explore the potential of PDT for glioblastoma treatment. Although glioblastomas are currently incurable, studies have shown that increasing the extent of glioblastoma resection leads to an improvement in the overall survival of the patient[159]. This is likely due to the fact that over 80 % of recurrences appear within 2 cm of the original tumour[138]. Though safe to use, there are limits to how much tumour can be removed surgically, even when using FGS, as the risk and consequences of damaging surrounding 'eloquent' brain tissue are too great[160]. This is where PDT can help. Due to its lack of genetic sensitivity, as well as its selectivity to malignant cells, PDT has the ability to safely remove a greater amount of infiltrated glioblastoma cells than resection surgery alone. This is especially true when coupled with 5-ALA mediated FGS[153, 104].

PDT is delivered to glioblastomas using one of two main methods - interstitial PDT (iPDT) and intraoperative PDT.

Interstitial PDT is the most invasive of the two, as it delivers treatment light by inserting one or several laser coupled fibre optic cables through intact brain tissue. However its advantage is that it can be delivered to to a fully intact tumour that is otherwise deemed inoperable (e.g. located too deep within brain to be safely surgically removed). This also allows the treatment to be delivered for patients who might be too weak for surgery[161]. Treatment planning systems such as FullMonteWeb[10] are used before treatment to determine the optimum number, geometry and placement of fibres in order to optimise treatment by finding a balance between maximising the treated volume and keeping thermal and physical damage to the surrounding tissues to a minimum[104].

Intraoperative PDT however is generally applied after the tumour has been surgically removed with the main goal of removing any remaining tumour tissue. Most commonly this is done by inserting a balloon diffuser containing an optical fibre into the resection

a) Interstitial PDT   b) Intraoperative PDT
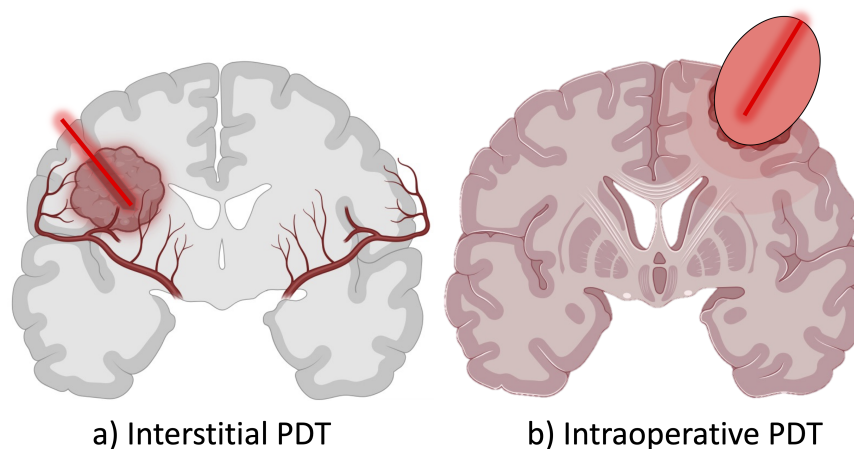
Figure 4.2: Image showing the basic setup of (a) interstitial PDT for glioblastoma and (b) intraoperative PDT. Interstitial PDT involves inserting one or a number of laser coupled optical fibres directly into an intact tumour to deliver the PDT treatment light. Intraoperative PDT involves surgically resecting the main bulk of the tumour before treating the remnant tumour tissue with PDT light using an optical diffuser such as a scattering fluid filled balloon. (Created with BioRender.com)

cavity[162]. This allows the treatment light to be delivered evenly around the cavity. Inflating the balloon to an appropriate size for the specific tumour cavity allows the full area to be treated in one go. A diagram illustrating the difference between intraoperative and interstitial PDT can be seen in figure 4.2.

Table 4.2 presents several recent clinical trials using either iPDT or intraoperative PDT to treat glioblastoma.

4.4.2 INDYGO trial

A phase I clinical trial named the INDYGO trial (INtraoperative photoDYnamic therapy for GliOblastoma) recently took place at Lille University Hospital, France. The aim of the trial was to test the feasibility of enhancing the Stupp protocol (see section 4.4) by treating the resection cavity walls with 5-ALA mediated PDT in order to maximise tumour resection and improve patient survival time[97].

Figure 4.3 shows the basic setup of the light delivery method used. An optical fibre

Author	Method	Results	Number of patients
Stepp et al. (2007)[163]	• iPDT (post operative) • Recurrent and new GBM • 5-ALA (20 mg/kg) • 100, 150 and 200 J/cm^2	• 41 % with 6 months progression free survival	18 clinics
Beck et al. (2007)[9]	• iPDT • Recurrent GBM • 5-ALA (20 mg/kg) • 100 J/cm^2	• 15 months median overall survival	10
Johansson et al. (2013)[164]	• iPDT • Recurrent and new GBM • 5-ALA (20 - 30 mg/kg) • 720 J/cm^2	• 3 of the 5 patients still alive after 36 months • No further follow-up	• 1 new • 4 recurrent
Schwartz et al. (2015)[165]	• iPDT • New GBM • 5-ALA (20 - 30 mg/kg) • 12.960 J/cm^2	• 16 months median progression free survival	15
Schipmann et al. (2020)[102]	• Fluorescence Guided Surgery (FGS)+ Intraoperative PDT • New HGG • 5-ALA (20 mg/kg) • 200 mW/cm for 1 hour • 100 % oxygen ventilation	• 6 months mean progression free survival	20
Vermandel et al. (2021)[97]	• Intraoperative PDT • New GBM • 5-ALA (20 mg/kg) • 200 J/cm^2	• 23.1 months median overall survival	10

Table 4.2: Table presenting several clinical trials looking at treating glioblastoma brain tumours with 5-ALA mediated PDT using either iPDT or intraoperative PDT.
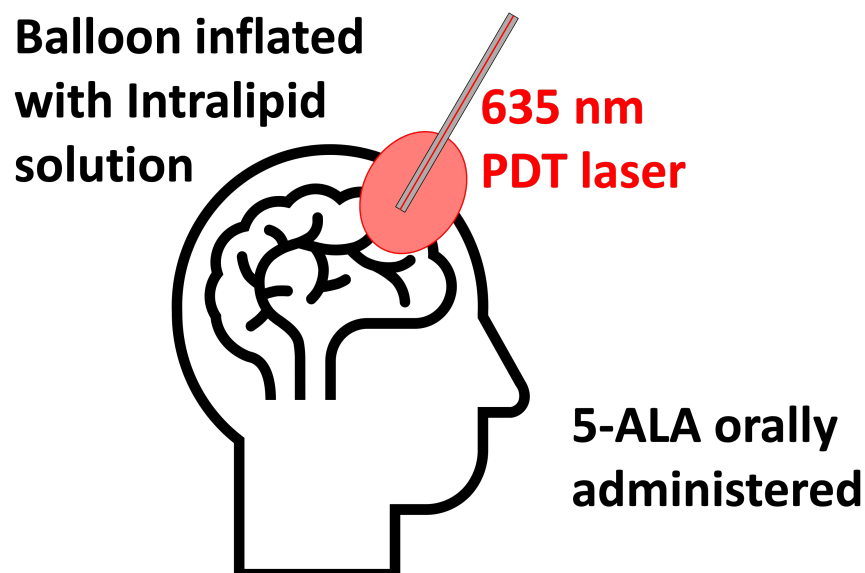
Figure 4.3: Basic setup of the INDYGO trial protocol. 5-ALA, precursor to the photosensitiser PpIX, is orally administered 6 hours before resection surgery. A balloon attached to the trochar device, which contains an optical fibre coupled to a 2 W, 635 nm PDT laser, is inserted into the resection cavity left by surgical tumour removal and is inflated with Intralipid scattering solution until it conforms with the cavity walls. This combination allows the PDT treatment light to be delivered evenly around the cavity wall.

coupled to a 635 nm PDT laser sits inside an inflatable balloon which is attached to the trocar device. Six hours before surgery, the patient is orally administered a dose of 5-ALA - precursor to photosensitiser PpIX. Fluorescence guided surgery (FGS) is used to safely remove as much of the tumour as possible before inserting the balloon into the resection cavity and filling it with intralipid scattering solution until it expands to the size of the cavity. The laser is switched on, illuminating the cavity walls with PDT treatment light, further removing remnant tumour cells within the surrounding healthy tissue.

By measuring how much intralipid solution is injected into the balloon ($V_{intralipid}$), the total PDT treatment time (t) is calculated based on equation 4.1.

$$t(min) = 0.1176 V_{\text{intralipid}}(ml) + 3.4276 \tag{4.1}$$

This is an algorithm developed pre-clinically by the trial group to calculate the time needed to achieve a total light fluence of 200 J/cm^2 at the balloon wall using the 635 nm laser at a power of 2 W. This value was based on the assumption that a fluence of 200 J/cm^2 at the

Parameter	Standard Value
Intralipid Volume ($V_{intralipid}$)	50 ml
Treatment Time	8.6 Min + 8 Min of fractionation breaks
Light Power	2 W
PpIX Concentration	5 μM

Table 4.3: Standard protocol parameters used throughout this work.

balloon wall results in a fluence of 25 J/cm^2, known to have good PDT effect, at a depth of 5mm from the balloon[166].

To encourage triplet oxygen recovery and increase treatment efficacy, the trial protocol also includes 'fractionation' of the treatment light. This is where the treatment time, calculated using equation 4.1, is split into 5 equal fractions and a 2 minute rest period, where the light is switched off, is inserted between each fraction[167]. This extends the total time it takes to deliver the PDT treatment by 8 minutes.

The preliminary results of the trial were published in 2021[97]. They included an increased median survival rate from the current 14.6 months[104] to 23.1 months and an absence of any adverse effects. A secondary, multicentre phase II clinical trial named DOSINDYGO (DOSe finding for INtraoperative photoDYnamic therapy of GliOblastoma) followed the INDYGO trial. The purpose of this second stage was to modify the light dose delivered to find an optimum level for the best treatment tolerability and effect[97]. The results of this trial have not yet been published at the time of writing.

4.4.3 INDYGO trial simulation

The aim of this work was to simulate the INDYGO trial protocol using MCRT methods with the goal of increasing understanding of the treatment and how changes to the standard parameters might affect treatment efficacy. Further to the simulation benefits discussed in section 3.2.9, simulating PDT for glioblastoma is especially valuable as, due to the rarity and heterogeneity of the disease, as well as often very strict eligibility criteria, clinical trials can be difficult to recruit to[168]. This makes it extremely useful to be able to, pre-clinically, simulate a fully optimised treatment protocol, minimising clinical trial failures.

The 'standard protocol' parameters used throughout this work are detailed in table 4.3. The values for oxygen modelling described in section 3.4.1 are also used.

Using the Wang protocol for PDT modelling described in section 3.4, the percentage of glioblastoma cells killed over the treatment time is calculated and used as a measure of

treatment efficacy. The difference in glioblastoma cell kill due to changes to the standard treatment parameters are explored. To test the sensitivity of the oxygen modelling parameters, such as the initial triplet oxygen concentration and the singlet oxygen concentration toxic threshold, these are also varied and the effect on cell kill determined.

4.5 Brain model

The first step needed to simulate PDT for glioblastoma was to obtain a realistic computational model that could be incorporated into the MCRT code. The model used was developed by Suveges *et al.* at the University of Dundee[169]. They used mathematical modelling to model the growth and development of glioblastoma tumours within a 3D brain model, created using MRI scans. A model containing the final result of a tumour grown in the front-right section of the brain (shown in figure 4.4) was provided in the form of three 236 x 206 x 150 voxel arrays. These arrays contained density values for white matter, grey matter and glioblastoma tissue, and could be combined to form a model of the full brain. No information about the dimensions of the brain model was provided, and so, based on the average dimensions of a human brain, the full size of the model was assumed to be 165 mm x 144 mm x 105 mm, making each voxel have dimensions 0.7 mm x 0.7 mm x 0.7 mm and volume 0.7 mm^3.

4.6 Model adaptations

Before inserting the above brain model into the code, a few adaptations needed to be made in order to recreate the INDYGO trial setup.

4.6.1 Tumour resection

To simulate the surgical resection of the tumour, the centre of the tumour model was computationally removed, leaving only the edges. To achieve this, a 5 x 5 'mask', made using an array containing only 1s, was created and scanned through each 2D slice of the array containing the tumour as shown. At each point, the mask is multiplied by the section of the tumour array that it overlaps and the number of 0s in the resulting array are counted as shown in figure 4.5. If the number of 0s was three or less then the central value of the tumour array section, underlined in figure 4.5 was changed to a 1. By doing this for each point in the array, the centre of the tumour was converted to 1s, leaving a roughly 2 mm thick border of tumour cells as shown in figure 4.6. The final result of the resection algorithm when applied to the tumour array can be seen in figure 4.7b which shows the border left after resecting the 2D tumour slice shown in figure 4.7a.

(a)   (b)   (c)
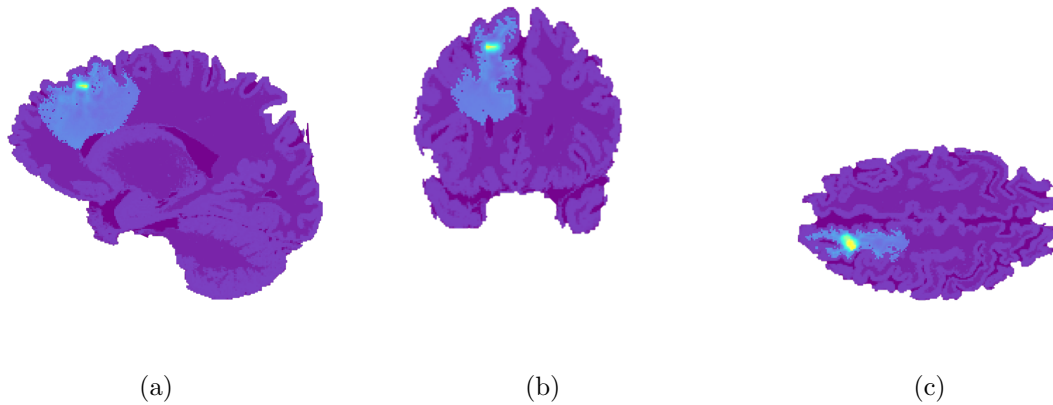
Figure 4.4: 3D model developed by Suveges *et al.* at the University of Dundee to simulate the evolution of glioblastoma tumours[169]. The model contains an algorithmically grown glioblastoma (coloured blue with the high density necrotic centre shown in yellow) within a brain model created using MRI scans. It was shared in the form of separate voxel arrays for each tissue type (grey matter coloured light purple and white matter indicated by the darker purple), allowing it to be easily incorporated into the MCRT code. The image shows three 2D slices of the models (a) sagittal plane, (b) coronal plane and (c) axial plane[137].

(a)   (b)
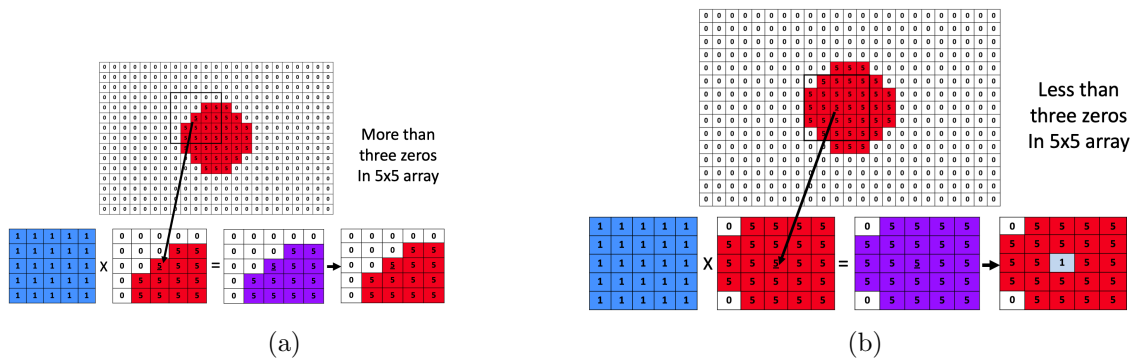
Figure 4.5: Images demonstrating the computational process used to 'resect' the tumour model. For each 2D slice of the model, a 5 x 5 array of 1s is scanned through the slice and multiplies with each 5 x 5 section that it overlaps. If the resulting array has more than 3 zeros as seen in (a), the central value of the section remains the same. However, if the resulting array has less than 3 zeros as in (b), then the central value is changed to a 1.

0	0	0	0	0	0	0	0	0	0	0	0	0	0	0	0	0	0	0	0	0	0	0
0	0	0	0	0	0	0	0	0	0	0	0	0	0	0	0	0	0	0	0	0	0	0
0	0	0	0	0	0	0	0	0	0	0	0	0	0	0	0	0	0	0	0	0	0	0
0	0	0	0	0	0	0	0	0	0	0	0	0	0	0	0	0	0	0	0	0	0	0
0	0	0	0	0	0	0	0	0	0	5	5	5	0	0	0	0	0	0	0	0	0	0
0	0	0	0	0	0	0	0	0	5	5	5	5	5	0	0	0	0	0	0	0	0	0
0	0	0	0	0	0	0	0	5	5	1	1	1	5	5	0	0	0	0	0	0	0	0
0	0	0	0	0	0	0	0	5	5	1	1	1	5	5	0	0	0	0	0	0	0	0
0	0	0	0	0	0	0	0	5	5	1	1	1	5	5	0	0	0	0	0	0	0	0
0	0	0	0	0	0	0	0	0	5	5	5	5	5	0	0	0	0	0	0	0	0	0
0	0	0	0	0	0	0	0	0	0	5	5	5	0	0	0	0	0	0	0	0	0	0
0	0	0	0	0	0	0	0	0	0	0	0	0	0	0	0	0	0	0	0	0	0	0
0	0	0	0	0	0	0	0	0	0	0	0	0	0	0	0	0	0	0	0	0	0	0
0	0	0	0	0	0	0	0	0	0	0	0	0	0	0	0	0	0	0	0	0	0	0
0	0	0	0	0	0	0	0	0	0	0	0	0	0	0	0	0	0	0	0	0	0	0

Figure 4.6: The end result after completing the full 'resection' process on the image shown in figure 4.5. A border of 2 pixels are left, with the central part of the shape converted to 1s.

(a) (b)
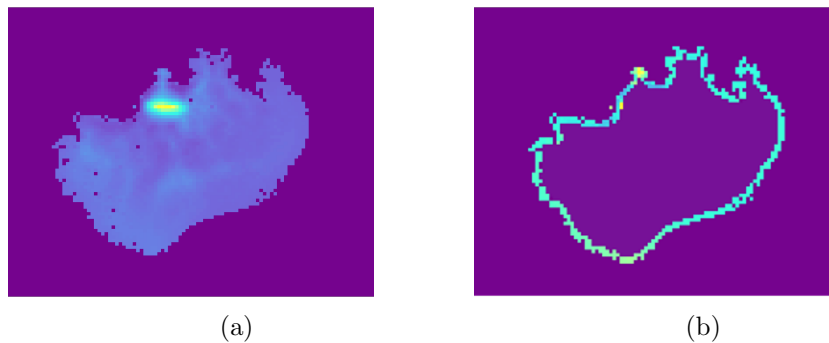
Figure 4.7: (a) A central 2D slice of the original tumour array. (b) The result after removing the central part of the tumour slice in (a) using the described resection algorithm. In both images, tumour is shown by the blue colour with the high density tumour centre shown in yellow[137].
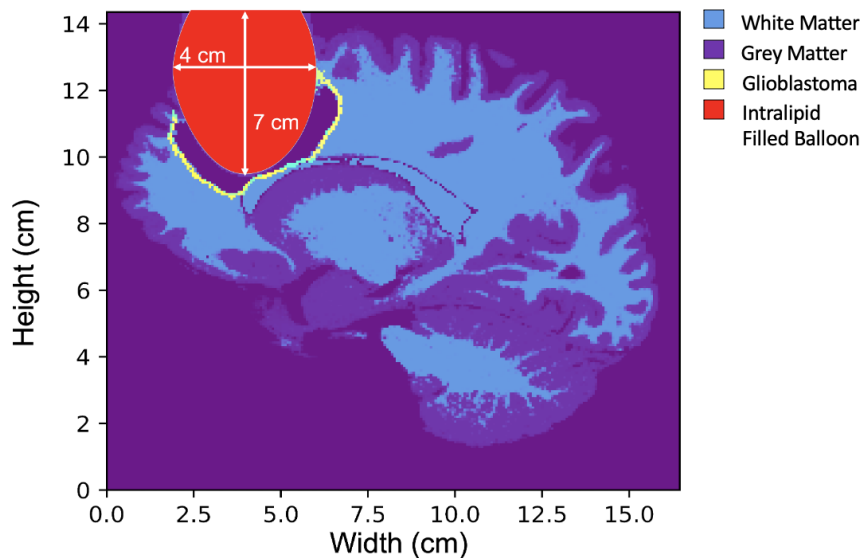
Figure 4.8: Central 2D slice of the full brain model after tumour resection and balloon insertion. The colour reference indicates the different tissue and material types included in the model[137].

4.6.2 Balloon insertion

The next step was to insert the balloon into the resection cavity. To do this, a 3D ellipse with minor axis lengths of 4 cm and 3 cm and a major axis length of 7 cm was created and placed within the centre of the resection cavity. The size of the balloon was chosen based on the dimensions of the tumour cavity and the assumption that the elliptical shape of the balloon will deform slightly as its pressed against the brain's falx cerebri.

An image showing the central slice of the full model with the balloon inserted can be seen in figure 4.8. It can be seen from this that gaps remain between the edges of the balloon and the cavity walls. Based on communication with the INDYGO trial team, it is known that this is realistic due to the fact that the cavity is not a perfect sphere. The balloon is stiffer than the brain tissue, and so will not conform to the cavities shape, resulting in saline filled gaps forming as modelled.
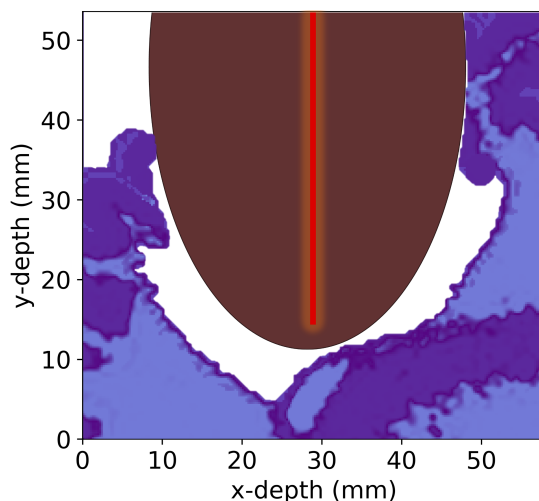
Figure 4.9: Image showing the central slice of the cut model with balloon inserted used in simulation with the smaller dimensions of 58 mm x 54 mm x 36 mm.

4.6.3 Resolution increase

While a model containing the full brain is useful to have, for the majority of investigations only a small part of the model was needed. A small section of the model containing the full resected tumour and at least 1 cm of surrounding brain tissue was extracted and used in the final simulation. An image of this section can be seen in figure 4.9. The number of voxels within this section was 83 x 77 x 52 making the grid dimensions 58 mm x 54 mm x 36 mm.

To gain higher resolution data, the resolution of the cut model was increased within a Python code using the SciPy function 'zoom'. This function uses spline interpolation to increase the number of points in an array. It was used to increase the grid resolution by a factor of 3, making number of voxels in the grid 250 x 231 x 155 and changing the voxel volume to 0.233 mm^3. A factor of 3 was chosen to allow the number of voxels to be similar to that of the original model, increasing the resolution but keeping simulation time reasonably low. The resolution increase then allowed more detail in the changes of different factors with depth from the cavity wall to be seen, such as fluence rate.

Once inserted into the code, a small 'blob' of tumour tissue was added back into the resected model which can be seen in the top, right hand corner of the cavity in figure 4.9. This was to help simulate a more realistic resection at the point where the top of the cavity overhangs slightly, potentially resulting in the surgeon removing less of the tumour there.

This unresected 'tumour remnant' also allowed us to simulate light penetrance into solid tumour, as opposed to 'tumour edge' (section 4.8.1).

4.6.4 Optical properties

The optical properties used for propagation of 635 nm light through each material type within the model are presented in table 4.4. The brain model consists of white matter, grey matter and glioblastoma tissue. The resection cavity contains the balloon, filled with intralipid solution, and the remaining cavity gaps are filled with saline solution to provide some level of index matching at the resection cavity walls. This index matching helps to minimise reflection, refraction and diffraction effects, decreasing the light power loss at the cavity walls.

Tissue / Material	Absorption Coefficient $(\mu_a)(\text{cm}^{-1})$	Scattering Coefficient $(\mu_s)(\text{cm}^{-1})$	Refractive Index (n)	Anisotropy Factor (g)	Reference
White Matter	0.63	686.0	1.38	0.85	[170]
Grey Matter	0.99	202.0	1.38	0.85	[170]
Glioblastoma	1.3	218.0	1.38	0.85	[170]
Intralipid Solution	0.001	10.0	1.33	0.875	[171]
Saline Solution	0.003	0.003	1.33	0.9	[172]

Table 4.4: Optical properties used within the simulation for propagation of 635 nm PDT treatment light. The brain tissue consists of white matter, grey matter and glioblastoma tissue. The resection cavity contains the intralipid filled balloon and any remaining gaps filled with saline solution.

The penetration depth of 635 nm light into each tissue/material used within the model is presented in figure 4.10. The data was produced by running MCRT simulations of 635 nm light transport into homogeneous slabs of each material type. The materials with high scattering coefficients compared to absorption result in large fluence rates at 0 cm due to back scatter. The low absorption coefficients of the saline and intralipid solutions result in lower attenuation rates, causing their fluence rates to remain above 0 beyond the 2 cm.

The optical properties were applied to the model using the density values of each tissue type. The provided white and grey matter grids were normalised, making their total
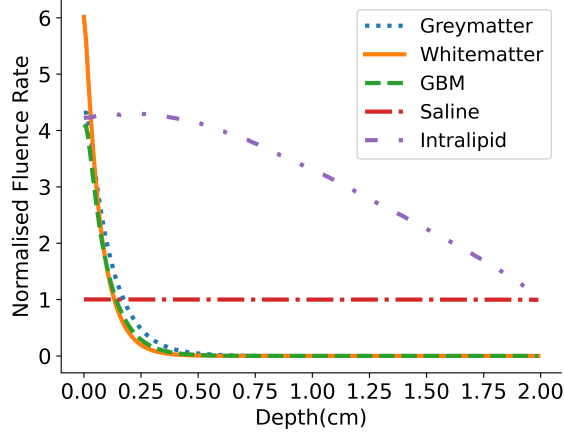
Figure 4.10: Fluence rate as a function of depth into homogeneous slabs of each material/tissue type used within the brain model. The fluence rate is normalised against the incident irradiation. The brain tissues cause high attenuation of the 635 nm light, due to their larger absorption coefficients. However, the intralipid and saline solutions have lower absorption coefficients, allowing a normalised fluence rate of at least 1 to reach the edge of the balloon and minimising the light attenuation within the remaining saline filled gaps.

equal 1 at the positions where brain matter is located and forming a complete brain when combined. This made applying the optical properties to voxels without tumour cells simple by using equation 4.2 where μ_x is the calculated value for the optical property within a specific voxel and $F_{\text{WhiteMatter}}$ and $F_{\text{GreyMatter}}$ are the fractions of white and grey matter within the voxel.

$$\mu_x = \mu_{x,\text{WhiteMatter}}F_{\text{WhiteMatter}} + \mu_{x,\text{GreyMatter}}F_{\text{GreyMatter}} \tag{4.2}$$

However, when the tumour grid is added in, the total values at the locations where the tumour is present go above 1. It was therefore assumed that, at the locations where tumour is present, the white and grey matter should only make up the remaining fraction. This is described mathematically in equation 4.3 where F_{GBM} is the fraction of glioblastoma cells in the voxel.

$$\mu_x = (1 - F_{\text{GBM}})\left(\mu_{x,\text{WhiteMatter}}F_{\text{WhiteMatter}} + \mu_{x,\text{GreyMatter}}F_{\text{GreyMatter}}\right) + \mu_{x,\text{GBM}}F_{\text{GBM}} \tag{4.3}$$

The starting concentration of PpIX within each voxel is calculated using equation 4.4 where $PpIX_0$ is the initial PpIX concentration (μM) for a voxel containing 100 % glioblastoma tissue.

$$C_{\text{PpIX}} = C_{\text{PpIX}_0} F_{\text{Glioblastoma}} \tag{4.4}$$

The optical properties of PpIX were also accounted for. The transmission coefficient of PpIX is $\mu_t = C_{\text{PpIX}}\varepsilon$, where ε is the extinction coefficient ($\varepsilon = 0.0265\text{cm}^{-1}(\mu\text{g/ml})^{-1}$ at 635 nm)[127].

4.7   PDT simulation

The algorithm, developed by Wang et al.[131] and described in section 3.4, was used within the model to simulate PDT. This model was selected over the Jacques model, described in section 3.3, as it accounts not only for the fluence rate and photosensitiser concentrations, but also for the concentrations of triplet and singlet oxygen, parameters that are equally important for PDT success.

The specific values for the PDT calculations (equations 3.14, 3.15 and 3.19) used within the brain model are presented in table 4.5.

Symbol	Definition	Value / Units	Reference
S_0	Photosensitiser (PpIX) concentration	$\mu M, t_{=0} = $ varied	[131]
$^3O_2$	Triplet oxygen concentration	$\mu M, t_{=0} = 38\mu M$	[173, 133]*
$[^1O_2]_{rx}$	Apparent reacted singlet oxygen concentration	$\mu M, t_{=0} = 0\mu M$	[131]
ξ	Ratio of proportional constant between the photochemical oxygen consumption and fluence rates, and photosensitiser concentration	$3.7 \times 10^{-3} cm^2 mW^{-1} s^{-1}$	[131]
ϱ	Low concentration correction	$33\mu M$	[131]
σ	Ratio of rate of $^1O_2$ reaction with ground state photosensitiser and rate of $^1O_2$ reaction with biological substrate, multiplied with concentration of biological substrate	$9 \times 10^{-5} \mu M^{-1}$	[131]
β	Ratio of rate of decay of photosensitiser triplet state and rate of triplet state photosensitiser quenching by $^3O_2$	$11.9\mu M$	[131]
Φ_0	Maximum rate of oxygen perfusion	$21.6\mu M s^{-1}$	[133]
υ_z	Blood flow velocity	$200\mu m s^{-1}$	[133]
R_c	Capillary radius	$2.5\mu m$	[174]
R_t	Radius of Krogh tissue cylinder (Half the distance between two capillaries)	$30\mu m$	[175]
l_z	Length of capillary	$200\mu m$	[174, 133]
q_0	Maximum metabolic consumption rate	$26.3\mu M s^{-1}$	[176, 135, 177] **
$[^1O_2]_{rx,threshold}$	Singlet Oxygen Threshold Concentration	$560\mu M$	[178]

Table 4.5: Parameter definitions and values for all PDT calculations.

* $^3O_2(i, j, k)$ at time $t = 0$ is set using the equation:

$$^3O_2(i, j, k)_{t=0} = \alpha PtiO_2 \tag{4.5}$$

where α is the triplet oxygen solubility in tissue $= 1.295\mu M/mmHg$[178] and $PtiO_2$ is the partial pressure of triplet oxygen in the brain $=$ 30 mmHg[173]

**The maximum metabolic consumption rate, in the required units of μMs^{-1}, was produced using equation 4.6 by using a comparison with the maximum metabolic oxygen consumption in skin.

$$q_{0,\text{cerebral}}(\mu M s^{-1}) = q_{0,\text{skin}}(\mu \text{Ms}^{-1}) \frac{q_{0,\text{cerebral}}(100\text{g}^{-1}\text{min}^{-1})}{q_{0,\text{skin}}(100\text{g}^{-1}\text{min}^{-1})} \qquad (4.6)$$

The cerebral metabolic rate of oxygen consumption according to Patel et al.[176] and Rink et al.[135] is 3.5ml100g^{-1}min^{-1}. Rink et al. also states that the metabolic rate of oxygen consumption in the skin is 0.2ml100g^{-1}min^{-1} whereas Lopez et al.[177] uses the value 1.5μMs^{-1}. By assuming that 0.2ml100g^{-1}min^{-1} and 1.5μMs^{-1} are equivalent, equation 4.6 uses the ratio of cerebral metabolic oxygen consumption to skin metabolic oxygen consumption to calculate a value for cerebral oxygen consumption in μMs^{-1}. The resulting calculation is shown by equation 4.7.

$$q_{0,\text{cerebral}}(\mu\text{Ms}^{-1}) = 1.5\mu\text{Ms}^{-1}\frac{3.5\text{ml100g}^{-1}\text{min}^{-1}}{0.2\text{ml100g}^{-1}\text{min}^{-1}} = 26.3\mu\text{Ms}^{-1} \qquad (4.7)$$

While white and grey matter are known to have different oxygen consumption rates, an average oxygen consumption rate for brain tissue was used here for simplicity, to create a single value estimate.

4.8 Parameters tested

4.8.1 Depth of effective PDT dose

The simulation was first run using the standard protocol parameters described in table 4.3. To determine how deep light penetrates into the brain and how far an effective PDT dose reaches using this protocol, the light dose and accumulated singlet oxygen concentration were plotted as a function of depth along the x, y and z lines shown in figure 4.11.

These lines were chosen for their relatively central positions and large enough tumour rim thicknesses that allow us to clearly view the results along a line with a good level of PDT activity. Due to the varying tumour thicknesses and densities, some areas around the resection cavity walls contained very little tumour and PpIX, resulting in much lower levels of singlet oxygen accumulation.

To test the depth of PDT effect into solid tumour, the depth of cell kill into small sphere of tumour tissue, placed in the upper right-hand corner of the resection cavity, was examined. A larger volume of tumour remaining in this area is possible as it is a point that is more likely to be missed by a surgeon.
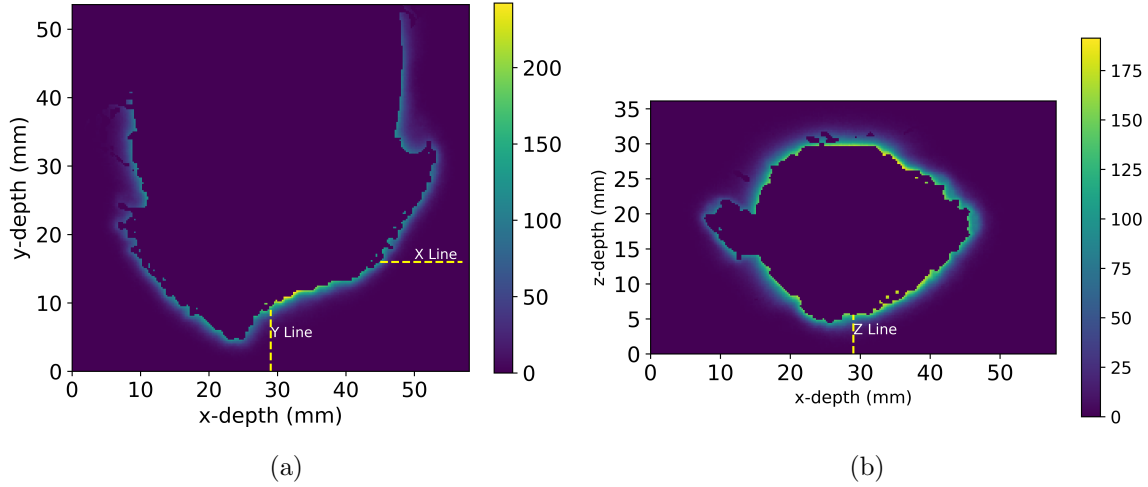
Figure 4.11: Images showing the light fluence in Jcm^{-2}, indicated by the colour bar, of a central slice of the tumour resection cavity. (a) shows a slice in the x-y plane and indicates the x and y lines used in data collection. (b) shows a slice in the x-z plane and indicates the z line used for data collection[137].

4.8.2   Photosensitiser and oxygen variation with distance

To explore the behaviour of the PpIX, triplet oxygen and singlet oxygen concentrations at different distances from the balloon wall, using the standard treatment protocol, each value was plotted over time for distances of 0 mm, 1 mm and 2 mm along the x-line indicated in figure 4.11a.

4.8.3   PpIX concentration

Next, several of the standard protocols parameters were varied and the efficacy of each variation quantified by the percentage of remaining GBM cells at the end of the treatment time.

The first treatment parameter to be varied was the initial concentration of the photosensitiser. The concentration of PpIX (μM) within each of the model's voxels was set relative to the fraction of GBM tissue ($F_{\text{Glioblastoma}}$) within it, as described by equation 4.8 where $PpIX_0$ is the initial PpIX concentration of pure GBM tissue.

$$\text{PpIX} = \text{PpIX}_0 F_{\text{Glioblastoma}} \tag{4.8}$$

Using the standard protocol described in table 4.3, a simulation was run for four different initial PpIX concentrations where $PpIX_0$ was set to 1 μM, 3 μM, 5 μM and 10 μM.

These values were chosen based on the range of PpIX concentrations measured in resected glioblastoma tissues by Johansson et al.[111], after performing fluorescence guided surgery.

4.8.4 Light fluence

The next parameter investigated was the light dose. This was varied first by doubling the treatment time to 17.2 minutes plus fractionation breaks, then by doubling the light power to 4 W.

4.8.5 Triplet oxygen depletion

The effect of oxygen depletion on the results was investigated by changing equation 3.15 to equation 4.9 in order to neglect the triplet oxygen depletion.

$$\frac{\delta^3 O_2(i,j,k)}{\delta t} = 0 \tag{4.9}$$

As mentioned previously, the purpose of fractionating the light source is to allow triplet oxygen recovery during the rest periods[167]. The difference in cell kill between constant and depleted triplet oxygen was therefore also explored without source fractionation.

4.8.6 Light source fractionation

To explore the difference that light source fractionation makes to the treatment outcome, a simulation was run where the total treatment time was kept at 16.6 minutes (8.6 + 8 minutes), but with the light switched on the whole time instead of turning it off for the fractionation breaks.

4.8.7 Singlet oxygen cell kill threshold

The singlet oxygen cell kill threshold value of 560 μM was produced by Zhu et al.[178] from *in vivo* measurements taken in mouse tumour models using the photosensitiser Photofrin. Unfortunately a value measured when using PpIX could not be found in literature, and so this value was used as an estimate until a more accurate value is found. While this is likely to be within the correct range, this threshold is known to vary with different factors such as photosensitiser and tissue type. Direct measurements are needed to gain a more accurate threshold for each specific scenario.

To determine the effect of varying this value on the simulation results, the standard protocol was run first with a 25 % larger cell kill threshold of 700 μM, then with a 25 % smaller threshold of 420 μM.

4.8.8 Maximum rate of oxygen perfusion

The maximum rate of oxygen perfusion controls the rate of triplet oxygen recovery within the model. As described in section 3.4.1, it is calculated using values such as the maximum metabolic consumption rate, the capillary length and radius, and the blood flow velocity through the capillary. These values are highly variable and difficult to measure directly, which made finding them in literature particularly challenging. To explore the sensitivity of the simulation results to changes in this rate, the percentage of glioblastoma cells killed when running the standard treatment protocol with three different values were compared. The values used were the standard protocol value ($\Phi_0 = 21.6$), double the standard value ($\Phi_0 = 43.2$) and half the standard value ($\Phi_0 = 10.8$).

4.8.9 Initial triplet oxygen concentration

The initial concentration of triplet oxygen was also challenging to find within literature due to its variability. The results from the standard protocol were therefore compared to those using half the standard concentration (19 μM) and double the standard concentration (76 μM) to test the sensitivity of results to this value.

4.9 Results

4.9.1 Depth of effective PDT dose

Plots showing the effective light dose and singlet oxygen concentration with depth are presented in figure 4.12 with the horizontal dashed line indicating the singlet oxygen concentration cell kill threshold and the vertical dashed line indicating the maximum depth of glioblastoma cells along the line. We can see from the blue dashed line in each plot that some level of light is reaching all tumour cells in each direction. However, by looking at where the horizontal threshold line crosses the orange singlet oxygen concentration line, we can see that the singlet oxygen does not get high enough to kill all glioblastoma cells within the region of investigation.

Figure 4.13a shows the tumour margin around the resection cavity wall before PDT, including the added tumour sphere (shown in yellow) in the upper right hand corner. The red area in figure 4.13c indicates where the singlet oxygen cell kill threshold has been achieved. We can see that a potential cell kill depth of around 1 mm is obtained within the solid tumour sphere.

4.9.2 Photosensitiser and oxygen variation with distance

Figure 4.14 presents 4 panels with plots showing the light power, photosensitiser concentration, triplet oxygen concentration and singlet oxygen concentration over the standard
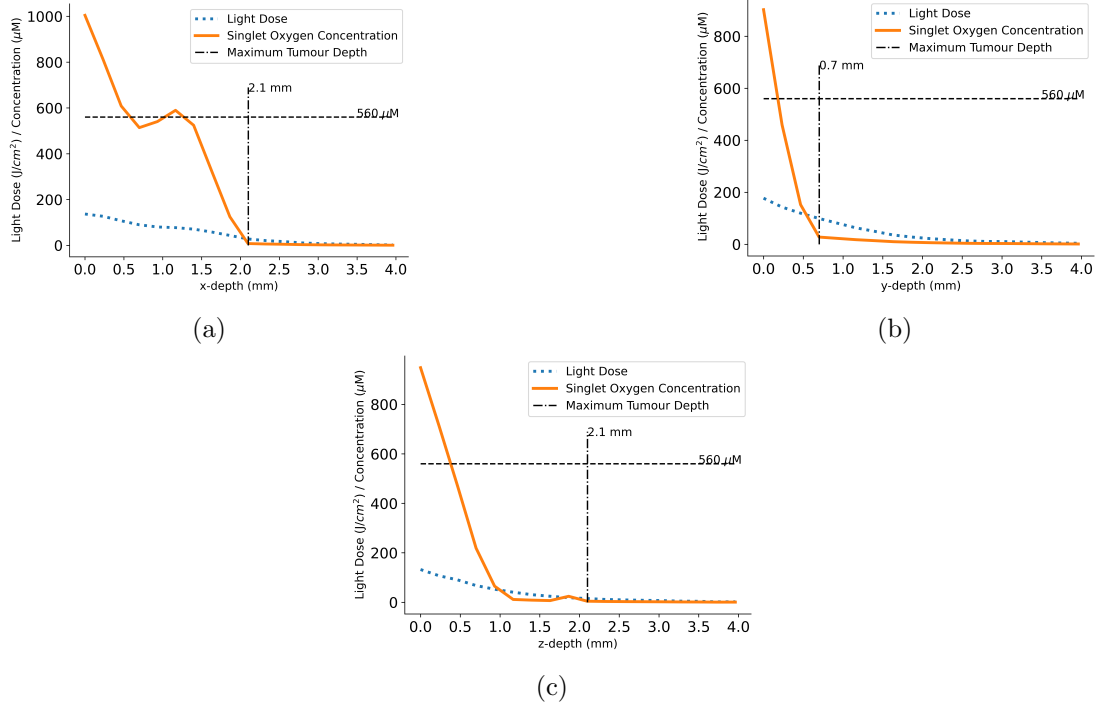
Figure 4.12: Line plots displaying the light dose and final singlet oxygen concentration over depth at three points in the x (a), y (b) and z (c) directions shown in figures 4.11a and 4.11b after delivering the standard treatment protocol from table 4.3. The horizontal dashed lines indicate the threshold singlet oxygen concentration value needed to cause cell death, while the vertical dashed lines show the maximum depth of glioblastoma cells along the lines. The results show that while some light appears to reach all glioblastoma cells along these lines, not enough singlet oxygen is being produced at deeper depths to allow all glioblastoma cells to be killed[137].
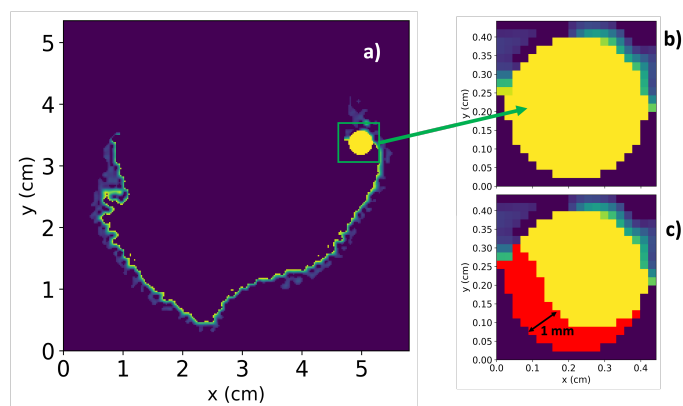
Figure 4.13: a) Tumour margin remaining after surgical resection but before PDT has occurred. The solid tumour sphere is shown in yellow. b) Close up image of the tumour sphere. c) The tumour sphere after the standard protocol PDT with the areas where the singlet oxygen cell kill threshold is reached marked in red. A potential cell kill depth of 1 mm is obtained[137].

protocols treatment time at at specific points along the x-line in figure 4.11a.

4.9.3 PpIX concentration

The percentage of glioblastoma cells remaining over the treatment time for each initial PpIX concentration is seen in figure 4.15. No glioblastoma cells are killed when using a concentration of 1 μM, however 39 % of the cells are killed with 5 μM and 61 % with 10 μM.

Figure 4.16 presents the results from figure 4.15 graphically. Each square shows a central slice of the resected tumour margin. The red areas indicate where cells have died and can be seen to increase over treatment time, especially for larger initial PpIX concentrations.

4.9.4 Light fluence

The results were compared with those from the standard protocol as shown in figure 4.17. In both cases, the total post-resection glioblastoma cell kill was seen to increase by a similar amount (15/16 %).
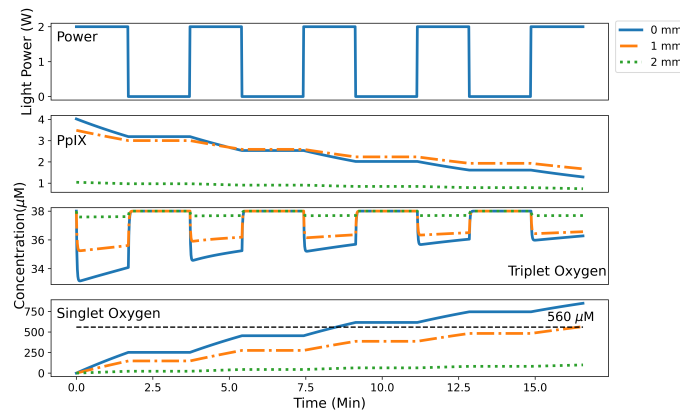
Figure 4.14: Line plots showing the change in light power, photosensitiser concentration, triplet oxygen concentration and singlet oxygen concentration over time when using the standard treatment protocol. Data from three different depths along the x-line marked in figure 4.11a are plotted, corresponding to 0 mm, 1 mm and 2 mm. The plot of singlet oxygen concentration demonstrates that glioblastoma cell kill is only possible up to 1 mm along this line when using the standard protocol[137].
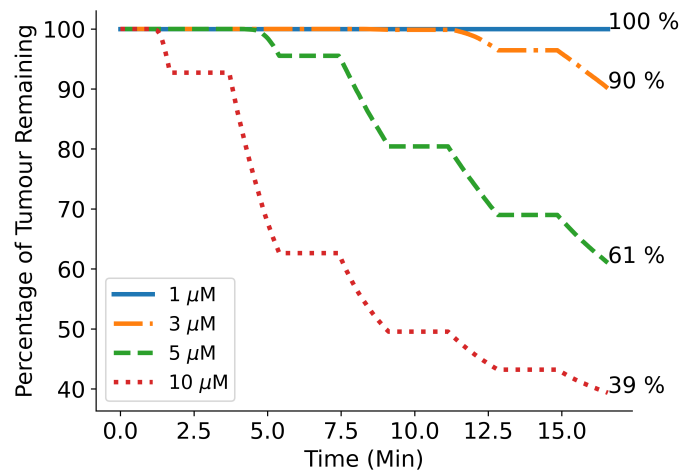
Figure 4.15: Line plot displaying the percentage of all, post-resection, glioblastoma cells remaining over treatment time for 4 different initial PpIX concentrations using the standard treatment protocol. A concentration of 1 μM shows no evidence of cell kill while 5 μM killed 39 % of glioblastoma cells and 10 μM kills 61 %[137].
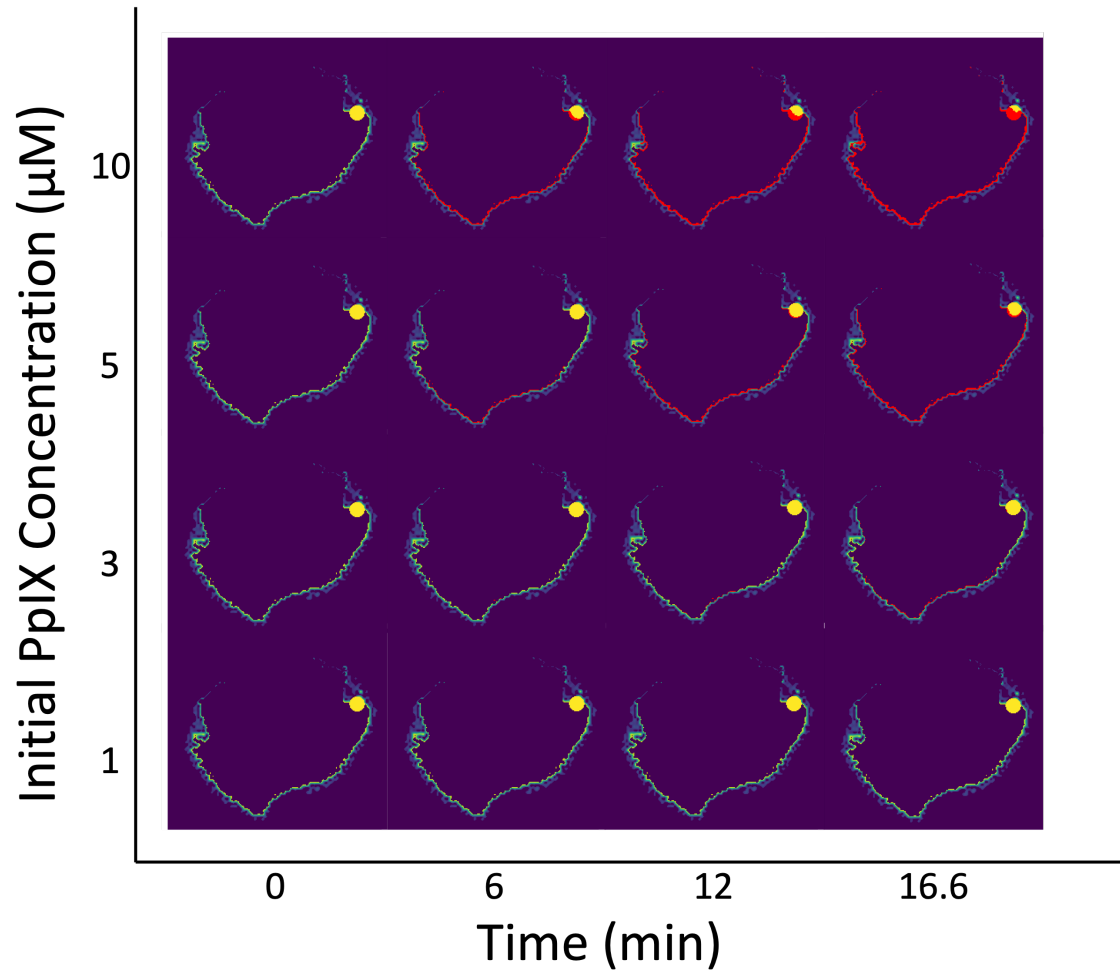
Figure 4.16: Graphical representation of glioblastoma cell kill over treatment time using the standard treatment protocol and initial PpIX concentrations of 1 μM, 3 μM, 5 μM, 10 μM. Each panel shows a central slice of the remaining tumour margin post simulated resection. The red areas highlight where glioblastoma cells have been killed by PDT over the treatment time.
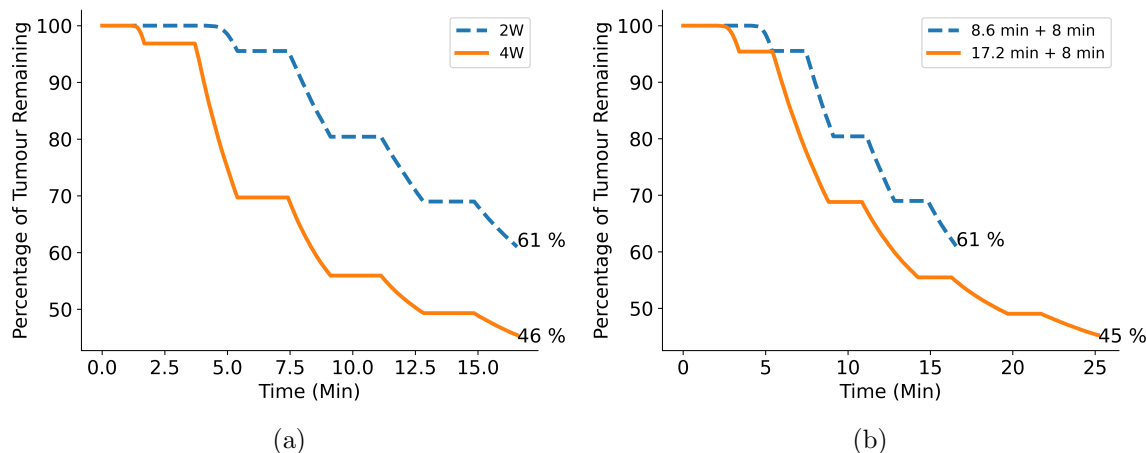
Figure 4.17: (a) Line plot showing a 15 % glioblastoma cell kill increase when doubling the light power from 2 W used in the standard protocol to 4W (b) Plot showing a similar 16 % glioblastoma cell kill increase when using the 2 W source and doubling the light dose by doubling the treatment time from the standard protocol to 17.2 minutes plus fractionation breaks[137].

4.9.5 Triplet oxygen depletion

The resulting glioblastoma cell kill when keeping the triplet oxygen constant is compared to the standard protocol with triplet oxygen depletion in figure 4.18a, where we can see that there is very little difference in GBM cell kill between the two cases.

Figure 4.18b shows the resulting cell kill when repeating the above comparison but without light source fractionation. Again, very little difference is seen between the two cases.

4.9.6 Light source fractionation

The glioblastoma cell kill over the full treatment time is compared to that of the standard protocol with fractionation breaks in figure 4.19. We can see from this that by leaving the light on for 8 minutes longer during the treatment time, the glioblastoma cell kill is increased by 16 %.

4.9.7 Cell kill threshold

The cell kill due to the singlet oxygen concentration toxic threshold value of 560 μM is compared to the results using values of 420 μM and 700 μM in figure 4.20. We can see from this that changes to the cell kill threshold affect the results with a 14 % decrease in
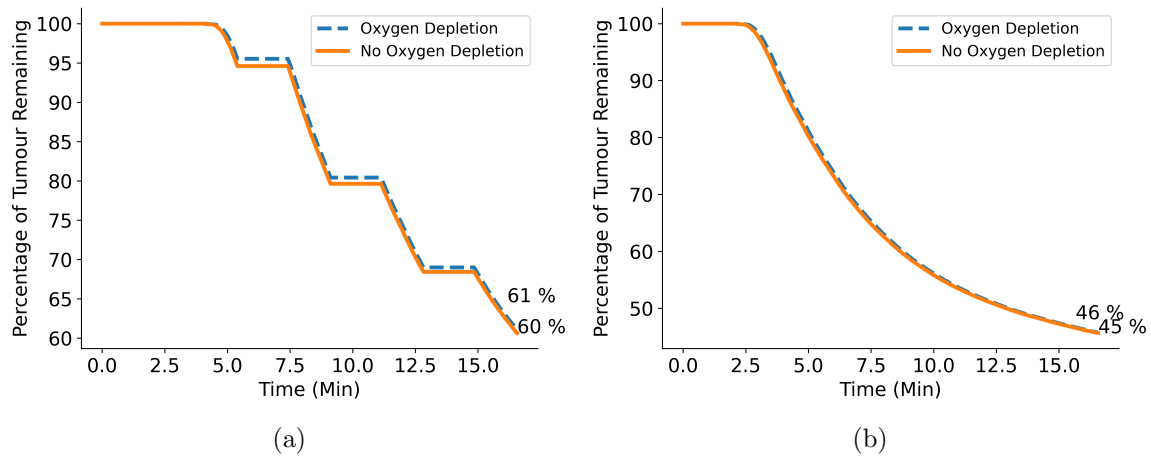
Figure 4.18: (a) Line plot comparing glioblastoma cell kill using the standard protocol, with and without triplet oxygen depletion. By the end of the treatment time, there is only a 1 % difference in the percentage of glioblastoma cells remaining. (b) Similar to (a) but done without fractionation of the light source. Again, almost no difference is seen in results[137].
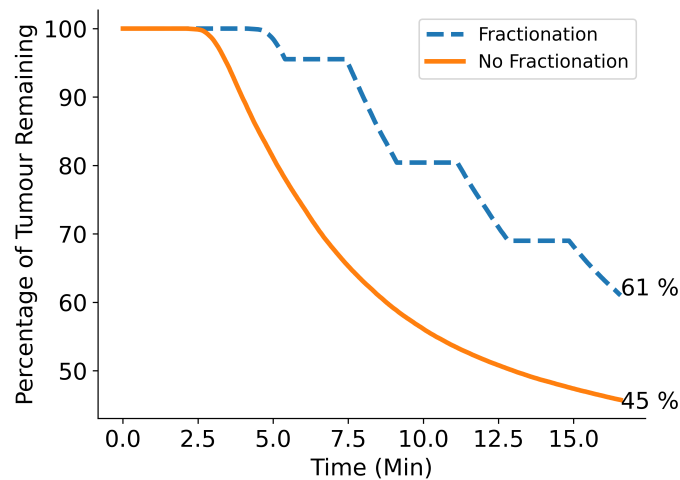
Figure 4.19: Plot comparing the glioblastoma cell kill over the treatment time when running the standard protocol with and without light source fractionation. By running the simulation for the full treatment time of 16.6 minutes but leaving the light on the full time, total cell kill was increased by 14 %[137].
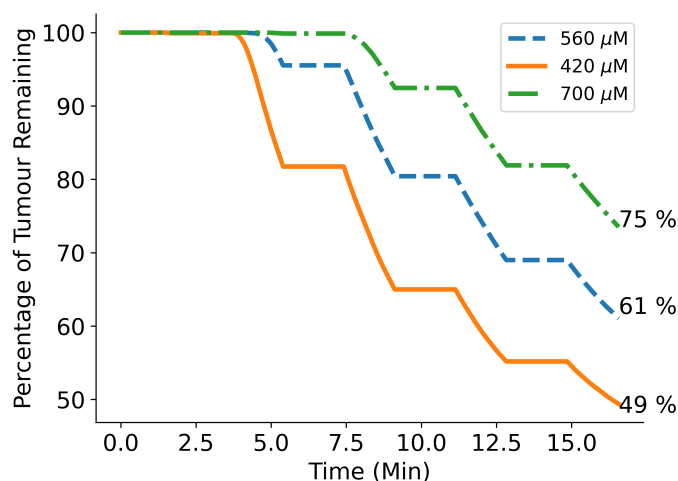
Figure 4.20: Line plot showing the glioblastoma cells remaining over treatment time with three different singlet oxygen concentration cell kill thresholds. The standard protocol is used and the standard threshold value of 560 μM is compared to threshold values of 700 μM (+ 25 %) and 420 μM (- 25 %). A cell kill difference of 14 % was seen when using 700 μM compared to the standard value. Similarly the cell kill percentage increased by 12 % when the lower value of 420 μM was used. These results suggest a roughly linear relationship between the percentage of glioblastoma cells killed and the singlet oxygen concentration cell kill threshold used[137].

cell kill when the threshold value is increased to 700 μM and a 12 % increase in cell kill when the value is decreased to 420 μM.

4.9.8   Maximum rate of oxygen perfusion

Figure 4.21 shows the results comparing GBM cell kill when using different maximum oxygen perfusion rates. We can see there is very little difference between the values.

4.9.9   Initial triplet oxygen concentration

From the results in figure 4.22, we can see that halving the initial triplet oxygen concentration causes a 7 % decrease in glioblastoma cell kill while doubling the initial concentration only causes a 4 % increase in cell kill.
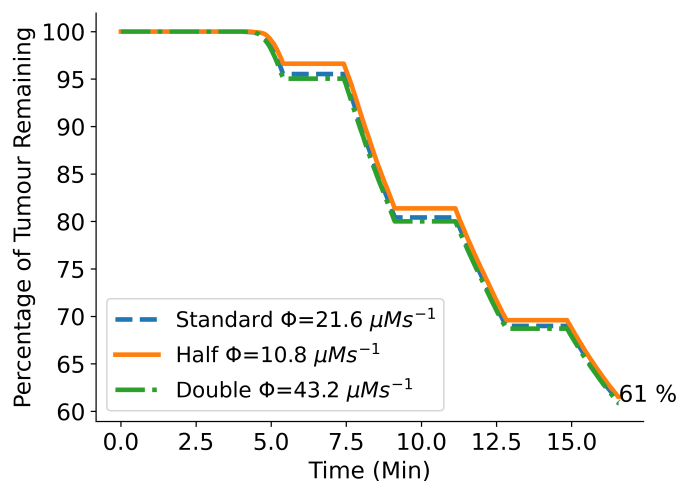
Figure 4.21: Line plot comparing the glioblastoma cell kill when using the standard treatment protocol and varying the maximum rate of oxygen perfusion. There is minimal difference in cell kill between the simulations using standard value of 21.6 μMs^{-1} and those using half and double this value.
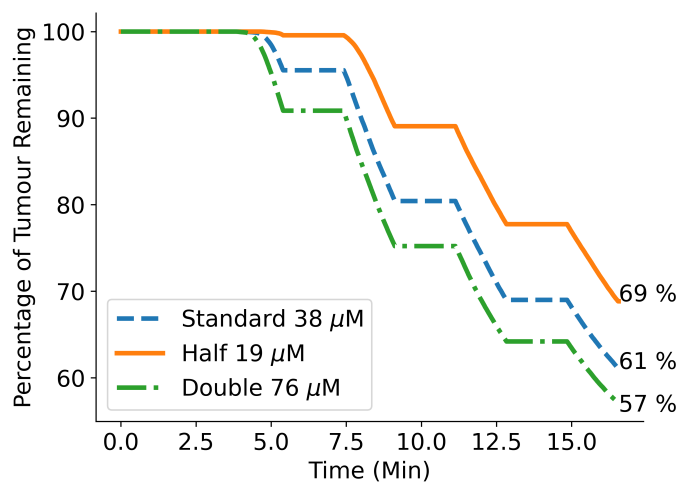
Figure 4.22: Plot showing the difference in glioblastoma cell kill when using the standard treatment protocol and varying the initial concentration of triplet oxygen. A non-linear relationship is seen with half the standard value causing a decrease in cell kill of 7 %, while doubling the standard value results in the cell kill increasing by 4 %.

4.10 Discussion

4.10.1 Depth of effective PDT dose

As with the skin model optical properties, the optical properties used for the brain may have been affected by the sample preparation process, making them differ from their *in vivo* equivalents. However, as all of the tissue properties were taken from the same source and therefore prepared in the same way, any uncertainties are more likely to be consistent over all tissue types.

The plots in figure 4.12 demonstrate that, with an initial PpIX concentration of 5 μM, the standard trial protocol will not remove all remaining GBM cells. However, the blue dotted lines demonstrate that most of the remaining tumour cells are exposed to some level of treatment light exposure. This suggests that simply increasing the light dose will improve the level of cell kill achieved as it will induce higher concentrations of singlet oxygen production at deeper depths.

The differences in the plots in figure 4.12 demonstrate that the depth of light penetration and PDT effect is variable at different positions in the model. This is likely due to the heterogeneous nature of the brain model and is consistent with *in vivo* measurements in literature. Using a similar balloon device to that used in the INDYGO trial, Muller et al.[179] measured the penetration depth of 635 nm light into the brain while similarly using it to treat malignant tumour in the resection cavity walls with PDT. Although variable, the penetration depths simulated do fit within the range of Muller et al.'s measurements into mixed tumour and brain tissue. They measured the fluence rate to be attenuated to 37% at 0.8 - 4.9 mm with an average of 2.4 mm[179]. Within the simulation results in figure 4.12, the light dose is attenuated to 37% of the dose at the resection cavity wall over the depth range of 1.2 - 2.1 mm with an average depth of 1.6 mm. We can see that this model produces a satisfactory level of accurateness when simulating light transport into the brain.

When considering the depth of potential cell kill into the solid tumour (figure 4.13), we can see that most of the tumour sphere remained unharmed after PDT treatment. This suggests that intraoperative PDT is only a useful adjuvant treatment when coupled with a successful resection (> 95% tumour removal with no remaining solid tumour lumps). It should therefore be noted that all cell kill results refer to a model containing the tumour sphere and therefore to a 'worst case scenario' where ideal resection has not taken place.

4.10.2 Photosensitiser and oxygen variation with distance

From the second plot in figure 4.14, we can see that the initial photosensitiser decreases with distance from the edge of the resection cavity. This is due to the decrease in glioblastoma cell density with distance, resulting in there being a lower concentration of PpIX.

This decrease in concentration away from the resection cavity also corresponds well with Johansson et al's[111] findings which saw significantly lower levels of PpIX in tumour infiltrative zones of grade IV tumours. We can also see over time, that the PpIX concentration at 0 mm drops below that at 1 mm. This is due to the larger fluence rate there, as shown in figure 4.12 which causes more PpIX to be removed as described in equation 3.14.

The triplet oxygen concentration at each depth over the treatment time is seen in the third plot of figure 4.14. We can see here that the triplet oxygen depletion decreases with depth from the cavity wall. It can be seen from the second part of equation 3.15 that this is again caused by a larger fluence rate closest to the cavity wall, causing more triplet oxygen to be removed. From the steeper slant in the troughs where the light is switched on, we can also see that the oxygen recovery rate is faster at depths closest to the cavity wall. This can be explained by the third part of equation 3.15 where a lower triplet oxygen concentration causes more oxygen to be added back into the cell. Finally, we can also see that at later times, the drop in triplet oxygen when the light is switched on get smaller at all depths. This is caused by the decrease in PpIX concentration with time, which we can see from the second part of equation 3.15, causes a decrease in the amount of oxygen removed. This recovery of triplet oxygen concentration as photosensitiser is photobleached, was also seen experimentally by Georgakoudi et al. when measuring the oxygen concentration tumour cell spheroids during PDT treatment[180, 181].

The bottom plot of figure 4.14 shows the total concentration of singlet oxygen produced over time at each depth. As would be expected from equation 3.19, the larger fluence rate and PpIX concentrations at smaller depths cause more singlet oxygen to be produced there. The horizontal black dashed line on this plot indicates the threshold concentration needed for cell kill and from this we can see that, for the standard protocol, glioblastoma cells are only being killed up to a depth of 1 mm along this line.

4.10.3 PpIX concentration

It is clear from figure 4.15 that increasing the concentration of PpIX makes the largest difference to the GBM cell kill and therefore treatment efficacy. Any method that improves PpIX uptake will therefore likely have a positive effect on treatment outcome. Several recent studies have shown promise in this area by using methods such as photobiomodulation[182] and utilising nanoparticles for photosensitiser delivery[123]. A study by Mansi et al.[183] also showed promise by using ABCG2 transporter inhibitors to slow down the removal of PpIX, increasing its accumulated concentration in human glioma cell lines. However, while higher PpIX concentrations do appear to improve cell kill, a study looking at the effect of PDT on the permeability of the blood brain barrier (BBB) showed that PpIX doses above the approved 20 mg/kg combined with light doses above 15 J/cm^2 were associated with permanent damage to brain tissues and the BBB[184]. The potential toxic effect of increasing

PpIX concentration in tissue must be considered[153].

As mentioned in chapter 3, a small concentration of PpIX (0.1 μM) was added to the healthy tissue within the model to simulate imperfect PpIX selectivity. Lilge et al. have shown *in vivo* that the selectivity of PpIX to tumour tissue is very high, especially in white matter where no PpIX was detected[185]. The simulation results show that tissue with concentration values of 1 μM were not damaged during the standard protocol, suggesting that necrotic damage to healthy tissues due to PpIX accumulation is unlikely. This correlates with the relative safety profile of the clinical trials of interstitial PDT in brain[164, 163].

It should also be noted here that PpIX uptake is modelled here based on the tumour concentration within each voxel. In reality, photosensitiser uptake within tumours is extremely heterogeneous and the exact biological cause of this heterogeneity is not well understood, making it very difficult to accurately model PpIX distribution and uptake[104]. However, its clear from the results that sufficient PpIX uptake is vital to treatment success and therefore work needs to be done on both predicting the uptake of PpIX and measuring it *in vivo* in order to incorporate this value within the treatment planning process. Simply looking at administered light and photosensitiser doses are not enough to predict the treatment outcome[164].

4.10.4 Light dose

The results in figure 4.17 suggest that the effect when doubling the light dose from 200 to 400 J/cm^2 at the balloon wall is a 15 % increase in cell kill. Doubling the light power instead of treatment time achieves this cell kill increase in less time. However, this needs to be balanced with the increased rate of triplet oxygen consumption that a higher light dose brings. This correlation in cell kill with light dose has been observed *in vivo*, where the threshold dose values were seen to vary with photosensitiser type[185]. The effect of increasing the light dose on the temperature of the tissue also needs to be considered and is something that is explored in chapter 5.

It should be noted that these results may vary for other PDT induced mechanisms of cell kill. *In vitro* measurements on U87 cells performed by Vermandel et al.[186] showed that while higher treatment light powers increased cell kill via necrosis, they were associated with higher levels of inflammation and treatment toxicity, suggesting lower light powers are more effective at providing PDT treatment with lower side effects. Other studies by Lilge et al.[187, 188] have also shown that light fluences too low to induce cell kill via necrosis can induce larger rates of cell kill via apoptosis. Cell death via apoptosis is not considered within the PDT model used[131] and so it is possible that the reduction in necrotic cell kill with lower light power may be balanced out by an increase in cell kill via apoptosis. Finding a method to include apoptosis modelling into the simulation is an

important next step in order to improve its accuracy and reliability.

4.10.5 Triplet oxygen depletion

From the results in figure 4.18, it appears that oxygen depletion makes very little difference to the treatment efficacy within this model. The oxygen recovery rate is particularly high within brain tissue[135], likely making it sufficiently higher than the PDT usage rate for depletion to cause much of an issue. Further to this, it is also the case that the patient will have higher tissue oxygen saturation due to being anaesthetised and ventilated with oxygen rich gas in order to maintain tissue oxygen saturation[189]. Although it is known that GBM tumours can have necrotic areas with hypoxia[129], it should be observed here that this study is looking at treating the infiltrative growing edge of the GBM, which will likely have a good blood supply.

4.10.6 Light source fractionation

The results show that triplet oxygen depletion due to PDT makes no difference to the treatment efficacy, and so removing the light source fractionation seems to be a simple way to increase cell kill by 16 % without changing the treatment time or light power as shown in figure 4.19. However, as this would also mean a change to the light dose delivered, the resulting tissue temperature needs to be considered (see chapter 5).

4.10.7 Singlet oxygen cell kill threshold

From figure 4.20 we can see that the value used for the singlet oxygen concentration toxic threshold affects the GBM cell kill in a roughly linear way. While a fixed value of 560 μM is used within most of this work, it should be noted that the real value likely varies between people, tissue types and photosensitiser used. The standard value used was measured *in vivo* by Zhu et al.[178] using the photosensitiser Photofrin and a mouse model. Unfortunately a measured value using PpIX cannot be found in literature. The tissue response and singlet oxygen quantum yield of Photofrin and PpIX differ. They also accumulate in different parts of the cell which results in them needing different concentrations of singlet oxygen to cause cell kill. Therefore, to gain a fully accurate value for each scenario, direct measurements are needed.

Values for several other parameters (ξ and β) used within the PDT rate equations (see table 4.5) were also unavailable in literature for PpIX and were instead assumed by Wang et al.[131] to be equal to those to for Photofrin. Figure 4.20 was produced to form an estimation of how the calculated cell kill might change with different singlet oxygen thresholds.

However, the benefit of computational simulation is that as more accurate parameters

become available, the results can easily be updated and in the mean time, the simulation is a useful tool to compare how changes to different parameters affect efficacy.

4.10.8 Maximum rate of oxygen perfusion

The results in figure 4.21 suggest that all of the values for maximum oxygen perfusion tested, provide sufficiently high enough oxygen recovery for the PDT oxygen usage to pose minimal issues.

4.10.9 Initial triplet oxygen concentration

Initial triplet oxygen concentration is another value that is quite variable between tissue types, however the results in figure 4.22 show that the predicted efficacy of the treatment is not hugely sensitive to this value. It should also be noted that the model assumes a homogeneous initial distribution of triplet oxygen. In reality, this distribution is likely to be heterogeneous due to different tissue consumption rates and PO2 gradients around blood capillaries[136, 190].

4.10.10 Applicability of model

The numerical results and specific cell kill percentages obtained above apply only to the properties and geometry of the brain model used. Qualitative conclusions, such as changes that might increase cell kill may be more widely applicable however. Glioblastoma cell kill may also vary from the simulation results due to other factors that are not accounted for such as an immune response[104]. An ideal goal to increase applicability would be a personalised treatment planning system, allowing the simulation to be applied to patient MRI-generated brain models and increasing the accuracy of the quantitative results.

4.11 Conclusion

A Monte Carlo simulation of intraoperative PDT for the treatment of glioblastoma that incorporates light dose calculations as well as photosensitiser and oxygen depletion was developed. The impact of treatment parameters such as light dose and photsensitiser concentration on glioblastoma cell kill was investigated with the outcome calculated based on the concentration of singlet oxygen produced.

The work has shown several methods that could be used to improve the cell kill found using the INDYGO trials standard protocol. Increasing the light dose by increasing treatment time or light power are simple and effective methods. However, their safety first needs to be considered by looking at their effect on the tissue temperature. Larger PpIX concentrations appear to have the greatest effect on GBM cell kill but again, the safety of

high PpIX concentrations within brain tissues needs to be considered.

The sensitivity of the results to factors relating to the oxygen modelling such as triplet oxygen depletion, triplet oxygen perfusion, singlet oxygen cell kill threshold and initial tissue oxygen concentrations were also explored and the results found to be quite robust in most cases.

The results gained within this work have direct potential clinical benefit as evidence within literature shows that maximising tumour removal leads to improvement in treatment outcome. While the exact percentages of cell kill calculated cannot be relied upon to be fully accurate due to the many complexities and heterogeneous nature of GBM and its treatment, the model is an excellent tool for exploring the potential effect of several parameters on the treatment efficacy.

Chapter 5

Temperature effects of PDT

5.1 Summary

The brain model used within chapter 4, along with the fluence rates calculated within the MCRT simulations, are used within a heat diffusion code to predict the thermal effects of the standard INDYGO trial protocol (table 4.3), as well as some of the adapted protocols tested. Some 'optimised' protocols are developed that aim to increase overall GBM cell kill whilst keeping the tissue temperature at a safe level. The majority of work within this chapter was published in the *Journal of Biomedical Optics* in 2024[137].

5.2 Introduction and background

While intraoperative PDT is a promising treatment for glioblastoma brain tumours, an aspect that needs more investigation is the treatment's effect on the temperature of the surrounding brain tissue. The brain is very sensitive to changes in temperature[191] and so adequate temperature prediction and monitoring should be carried out to avoid adverse effects to the patient. During the pre-clinical work of the INDYGO trial, the thermal effects of the treatment were predicted by placing the balloon device into a water bath heated to 37 °C and leaving the 2 W laser on for 2 hours. This resulted in only a very small increase of the temperature of the water and so the thermal effects were deemed acceptable[166]. However, the ability of visible light to cause heating within a medium is dependent on the wavelength dependent absorption coefficient of the material. At 635 nm, the absorption coefficient of water is 0.00325 cm^{-1}[192] while the absorption coefficients of white matter, grey matter and GBM tissue are significantly higher at 0.63 cm^{-1}, 0.99 cm^{-1} and 1.3 cm^{-1} respectively[170]. This means that brain tissue is likely to heat up more than water when exposed to 635 nm light and so further investigation into the thermal effects of the INDYGO trials protocol is needed.

5.2.1 Tissue damage due to heating

Heating biological tissue to temperatures above the normal value of 37 °C can cause a range of effects, dependant on the duration and temperature range. When tissues reach between 40 °C and 45 °C, hyperthermia occurs. This can cause several physical and cytotoxic effects such as increased blood flow, cellular apoptosis and necrosis. Oedema or swelling can also occur, with potential haemorrhaging as temperatures increase[191]. At temperatures over 45 °C, protein and lipid denaturation can begin to occur where the tissue's physical and chemical structure can change[193]. Other changes that can occur specifically in brain tissue due to heating are increased BBB permeability, as well as changes in metabolism and neural activity[194]. If the above occurs in the brain, the patient can be affected by a range of physical and neurological symptoms[195].

5.2.2 Current temperature monitoring

While tissue temperature monitoring is not commonly used in glioblastoma resection surgery, monitoring methods do exist and are used when performing techniques such as photothermal therapy, where reaching and maintaining the correct temperatures is critical. To reduce any further risk to the patient, non-invasive monitoring methods can be used. These include techniques such as computed tomography, photoacoustic imaging, magnetic resonance thermometry and microwave radiometry, all of which allow 3D temperature maps to be produced[196, 197].

5.3 Methods

To simulate the temperature behaviour of the brain tissue, a heat diffusion code was used and run separately to the MCRT code developed in chapter 3. The code was originally developed by McMillan et al.[40] in order to simulate laser ablation of the skin using a pulsed laser. By changing the tissue model and thermal coefficients, as well as the light power and pulse length, the code could be adapted to simulate the temperature effects of intraoperative PDT on the surrounding brain tissue.

5.3.1 Heat diffusion simulation

Figure 5.1 presents a flow chart of the basic process followed by the heat diffusion code. A fluence rate grid produced using the MCRT simulation described in chapter 4 is first inserted into the code and used to obtain values for the absorbed energy within each voxel. These energy values are used within the heat transfer and temperature calculations to determine the effect of the fluence rate from the PDT source on the brain tissue temperature. The following sections go into further detail about each of these steps.
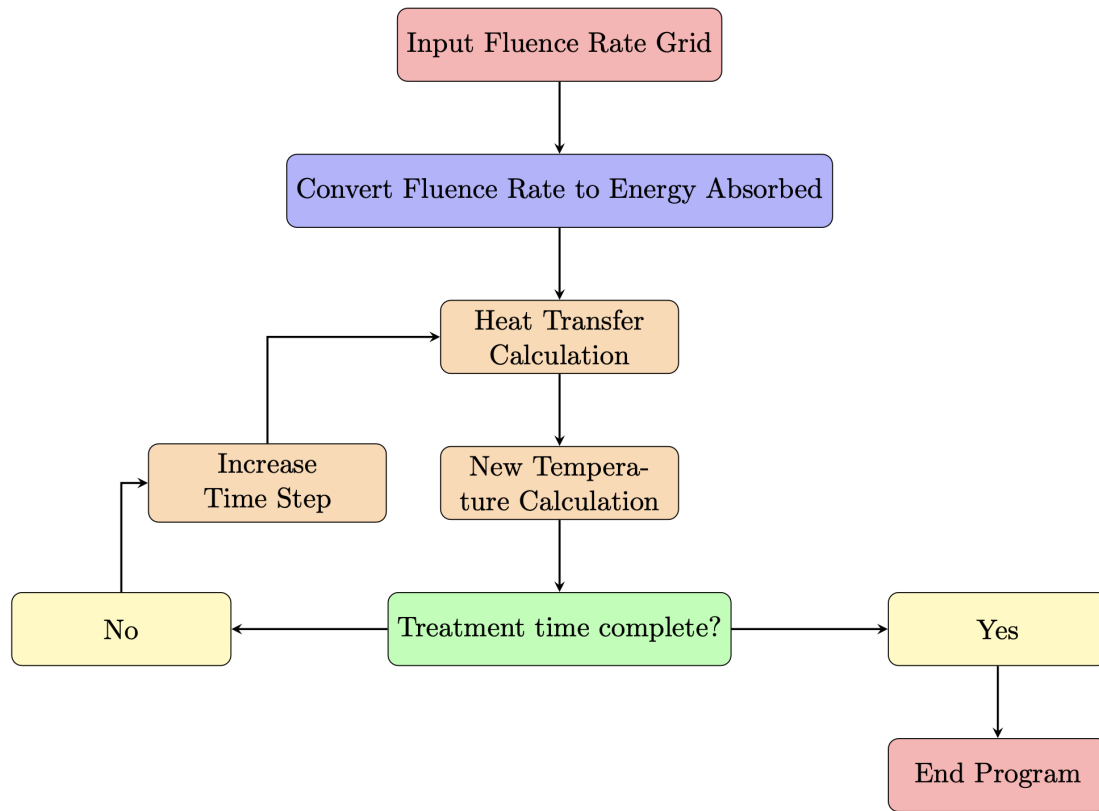
Figure 5.1: Flow chart summarising the process of the heat diffusion code. The MCRT output fluence rate grid is inserted into the code and used to calculate absorbed energy. These energy values are used to estimate the heat transfer and temperature changes within at each point. The process is repeated for each time step until the treatment time is complete.
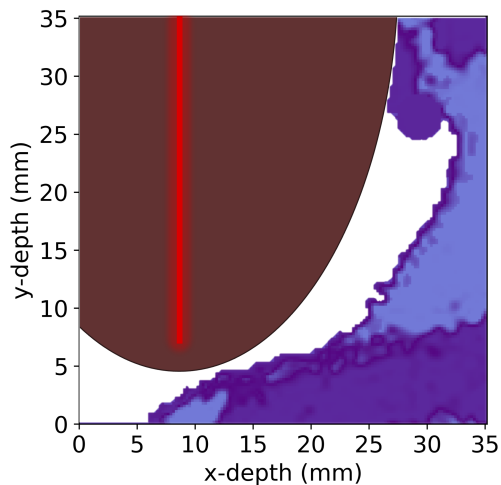
Figure 5.2: Central slice of the reduced voxel grid used within the heat diffusion simulation.

Grid input

In an effort to reduce the running time of the heat diffusion code, instead of running a new MCRT simulation for each time step, the fluence rate grid produced by the simulation described in chapter 4 was used within the code. This is possible as it is assumed that the only changes to the optical properties throughout the treatment time are due to changes in PpIX concentration which result in small, negligible optical property differences. The change to the fluence rate over the treatment time is therefore also minimal. The light power used is varied by changing the inserted fluence rate grid and fractionation breaks are simulated by temporarily setting the fluence rate to 0.

Due to constraints within the heat diffusion code caused by the parallelisation protocol[198], the number of voxels along each edge needed to be equal and divisible by 4. The grid used in chapter 4 was therefore cut to have 152 x 152 x 152 voxels, resulting in a grid with dimensions 35 mm x 35 mm x 35 mm and containing only part of the cavity as shown in figure 5.2. Assuming the fluence rate reaching each half of the tumour cavity is relatively symmetric, simulating only one half is reasonable to do. However, as the model itself is not symmetric, some differences in the energy absorbed and temperature increase between the two halves is likely.

Convert fluence rate to absorbed energy

To use within the heat transport calculations, the fluence rate first needed to be converted to absorbed energy. Within an MCRT simulation, energy absorbed can be calculated using equation 5.1.

$$Q_{\text{absorbed}}(i, j, k) = \frac{P}{V(i, j, k)N} \sum_N \mu_a(i, j, k)l(i, j, k) \tag{5.1}$$

Here:
$Q_{\text{absorbed}}(i, j, k)$ = the energy absorbed within the voxel at position (i, j, k) $(mJs^{-1}cm^{-3})$
P = the power of light source used within the MCRT simulation (mW)
N = the number of photon packets used within the MCRT simulation
V(i,j,k) = the volume of the voxel at position (i,j,k) (cm^{-3})
$\mu_a(i, j, k)$ = the total absorption coefficient within the voxel at (i,j,k) (cm^{-1})
$l(i, j, k)$ = the pathlength of a photon packet within voxel (i,j,k) (cm)

As the fluence rate $(\Psi(i, j, k))$ was calculated within the MCRT simulation using equation 5.2, the absorbed energy was obtained by multiplying the fluence rate grid with a 3D array containing the absorption coefficients of each voxel.

$$\Psi(i, j, k) = \frac{P}{V(i, j, k)N} \sum_N l(i, j, k) \tag{5.2}$$

For the heat transfer calculations, the absorbed energy was needed in units of $Js^{-1}m^{-3}$ and so it was necessary to convert the units of the calculated absorbed energy. Equation 5.3 shows the calculation used to convert the fluence rate $(mJs^{-1}cm^{-2})$ to the energy absorbed.

$$Q_{\text{absorbed}}(i, j, k) = 1000\Psi(i, j, k)\mu_a(i, j, k) \tag{5.3}$$

Heat transfer and new temperature calculations

To simulate the diffusion of heat throughout the model, the code works to solve the standard heat equation. This was derived using a combination of energy conservation laws and Fourier's law. Equation 5.4 shows the standard heat equations simplest 1 dimensional form with homogeneous thermal properties.

$$\rho c_p \frac{\partial T}{\partial t} = \Delta \cdot (\kappa \Delta T) + \dot{q} \tag{5.4}$$

Here:

ρ = density (kgm^{-3})
c_p = specific heat capacity (JK^{-1})
κ = thermal conductivity (Wm^{-1}K^{-1})
T = temperature at a specific time and position (K)
$\dot{q}$ = the source and sink term at a specific time and position (Wm^{-3})

The source and sink term ($\dot{q}$) accounts for all of the external heat sources and sinks. Within the simulation it is assumed that the energy absorbed due to the PDT light source (equation 5.3) is the main source of heat while the only loss of heat is due to conduction into the surrounding medium. At the start of the simulation, the temperature of the brain tissue is assumed to be 37 °C and everything else is assumed to be room temperature at 22 °C. To account for heat supplied by the body's metabolism, boundary conditions are set at the edges facing brain matter to stop the temperature dropping below 37 °C.

In this form, equation 5.4 can be solved using analytical methods. However, for higher dimensions, as used within this simulation, numerical models need to be used. The numerical model used within the heat diffusion code to solve the heat equation within the 3D grid is a Finite Difference Method (FDM) derived using the Taylor series (equation 5.5).

$$f(x_0 + \Delta x) = f(x_0) + \frac{f'(x_0)}{1!}\Delta x + \frac{f''(x_0)}{2!}\Delta x^2 + ... + \frac{f^{(n)}(x_0)}{n!}\Delta x^n + R_n(x) \qquad (5.5)$$

The FDM works by approximating a function $f(x)$ as a grid with N nodes spaced at a distance of Δx. The difference to $f(x)$ in the 'forward' direction is found by calculating the first order derivative of the function at the point $x_0 + \Delta x$. This is found by truncating the Taylor series after the second term, assuming the terms beyond this are small enough to be negligible, and rearranging to get equation 5.6.

$$f'(x_0) \approx \frac{f(x_0 + \Delta x) - f(x_0)}{\Delta x} \qquad (5.6)$$

The difference in the 'backward' direction is found by replacing $f(x_0+\Delta x)$ with $f(x_0-\Delta x)$ in equation 5.6 and the central difference is found by using the average of $f(x_0 + \Delta x)$ and $f(x_0 - \Delta x)$. The second order differential equations can also be approximated in a similar fashion by truncating equation (5.5) after the third term and rearranging for $f''(x_0)$ leading to equation 5.7.

$$f''(x_0) \approx \frac{f(x_0 - \Delta x) - 2f(x_0) + f(x_0 + \Delta x)}{\Delta x^2} \qquad (5.7)$$

The temperature at points $f(x,t)$, $f(x + \Delta x, t)$ and $f(x - \Delta x, t)$ are known while the temperature at $f(x, t + 1)$ is unknown. Using the FDM, we can take equation 5.4 and

insert the approximations for the first order time derivative and the second order spacial derivative. This can be rearranged to find $f(x, t+1)$ as shown in equation 5.8 which calculates the temperature (T) at point x and time $t+1$.

$$\frac{T_x^{t+1} - T_x^t}{\Delta t} = \frac{\kappa}{\rho c_p} \frac{T_{x-1}^t - 2T_x^t + T_{x+1}^t}{\Delta x^2} + \frac{\dot{q}}{\rho c_p} \tag{5.8a}$$

$$T_x^{t+1} = T_x^t + \Delta t \frac{\kappa}{\rho c_p} \frac{T_{x-1}^t - 2T_x^t + T_{x+1}^t}{\Delta x^2} + \Delta t \frac{\dot{q}}{\rho c_p} \tag{5.8b}$$

To account for potential differences in the thermal and optical properties, both temporally and spatially, the average of adjacent points (equation 5.9) are used instead.

$$\kappa^{\pm} = \frac{\kappa_x + \kappa_{x\pm1}}{2} \tag{5.9a}$$

$$\rho^{\pm} = \frac{\rho_x + \rho_{x\pm1}}{2} \tag{5.9b}$$

$$c_p^{\pm} = \frac{c_{p,x} + c_{p,x\pm1}}{2} \tag{5.9c}$$

This makes equation 5.8:

$$T^{N+1} = \Delta t (AT_{x-1}^t - 2DT_x^t + BT_{x+1}^t) + T_x^t + \frac{\Delta t \dot{q}}{\rho c_p} \tag{5.10}$$

where:

$$A = \frac{\kappa^-}{\rho^- c_p^- 2\Delta x^2} \tag{5.11a}$$

$$B = \frac{\kappa^+}{\rho^+ c_p^+ 2\Delta x^2} \tag{5.11b}$$

$$D = \frac{A + B}{2} \tag{5.11c}$$

Equation 5.10 refers only to the 1D case but can easily be converted to the 3D case as shown in equation 5.12.

$$U_x = AT^t_{x-1,y,z} - 2DT^t_{x,y,z} + BT^t_{x+1,y,z} \tag{5.12a}$$

$$U_y = AT^t_{x,y-1,z} - 2DT^t_{x,y,z} + BT^t_{x,y+1,z} \tag{5.12b}$$

$$U_z = AT^t_{x,y,z-1} - 2DT^t_{x,y,z} + BT^t_{x,y,z+1} \tag{5.12c}$$

$$T^{N+1}_{x,y,z} = \Delta t(U_x + U_y + U_z) + T^t_{x,y,z} + \frac{\Delta t \dot{q}}{\rho c_p} \tag{5.12d}$$

Equation 5.12d is the full numerical solution to the heat equation where $T^N_{x,y,z}$ is the temperature in units of kelvin (K) at voxel (x, y, z) within the current time step and $T^{N+1}_{x,y,z}$ is the new temperature at voxel (x, y, z)[198].

The thermal properties used within the simulation are displayed in table 5.1. For simplicity, the values used within brain tissue are for average brain rather than separate values for white matter, grey matter and GBM, while the Intralipid values are assumed to be the same as that of water. All values were taken from the IT'IS foundation tissue database[199].

Tissue / Material	Density (ρ) (kgm^{-3})	Heat Capacity (c_p) (Jkg$^{-1\circ}$C^{-1})	Thermal Conductivity (κ) (Wm$^{-1\circ}$C^{-1})
Brain Tissue	1046	3630	0.51
Intralipid Solution	994	4178	0.6

Table 5.1: Thermal properties used within the heat simulation for Intralipid solution and brain matter[199].

Initial temperature

To allow the temperatures at the material boundaries to equalise naturally before the PDT light source was switched on, the heat diffusion code was run with a light fluence rate of zero for 10 minutes. The resulting temperature grid (figure 5.3) was used to set the initial temperature within each voxel for all further simulations.

5.3.2 Simulated maximum temperature of brain tissue

To explore how the intraoperative PDT protocols from chapter 4 affect the temperature of the brain tissue, heat diffusion simulations were run that reproduced the delivered light fluences and fractionation breaks. To evaluate the safety of each protocol, the maximum temperature over the treatment time is recorded.
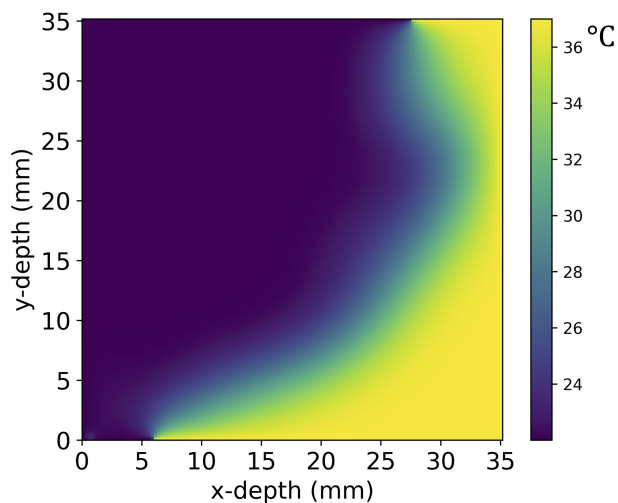
Figure 5.3: Heat map showing the initial temperature of the grid slice shown in figure 5.2 in °C.

Standard protocol

First the standard protocol (table 4.3) was simulated by inputting the 2 W fluence rate grid and running the simulation with an 8.6 minute irraditation time, split into 5 equal fractions separated by 2 minute rest periods.

Doubling the light fluence

Next, the protocols that doubled the delivered light fluence were simulated. First the treatment time was doubled by increasing the irradiation time to 17.2 minutes, then the power was doubled by changing the inserted fluence rate grid to one produced using a 4 W light source.

Removing fractionation breaks

Finally, the effect of removing the fractionation breaks from the standard protocol was determined by running the simulation with the 2 W fluence rate grid and an irradiation time of the full protocol time of 16.6 minutes with no rest periods.
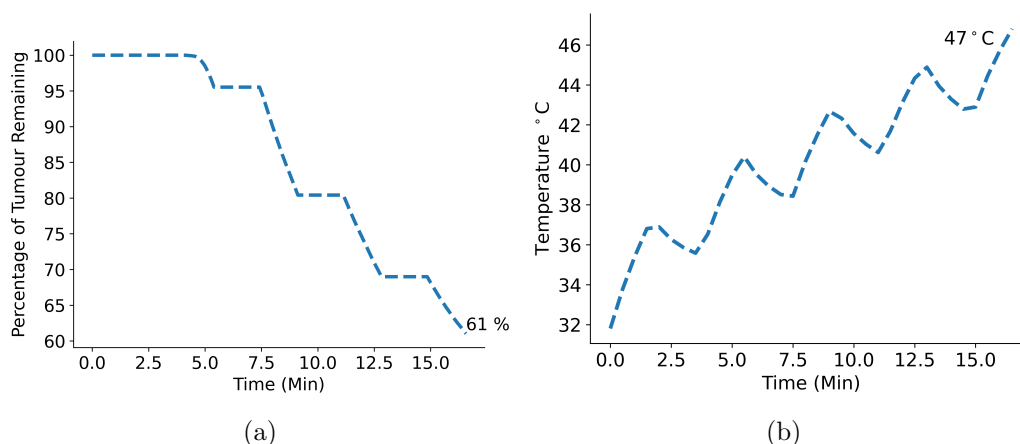
Figure 5.4: (a) Line plot showing the percentage of GBM cells remaining over time for the standard protocol simulation, as seen in chapter 4 (b) Line plot showing the maximum tissue temperature over time for the standard protocol. The maximum temperature reached is 47 °C[137].

5.4 Results

5.4.1 Standard protocol

Figure 5.4a shows the percentage of GBM cells remaining over the standard treatment protocol while figure 5.4b shows the maximum tissue temperature reached within the model over the treatment time. Cramer et al. states that the maximum temperature of brain tissue during PDT treatment where permanent damage is not generally observed is 48 °C[104]. We can see that the maximum tissue temperature was within safe limits at 47 °C.

Figure 5.5 shows a heat map of the grid slice where the point of maximum temperature is located at the end of the standard protocol. The colour bar to the right of the map indicates the corresponding temperature in °C for each colour, with the yellow areas showing where the temperature is highest.

5.4.2 Doubling the light fluence

Figure 5.6 shows the effect of doubling the irradiation time to 17.2 minutes on the simulation results, with figure 5.6a showing the percentage of tumour remaining and figure 5.6b showing the maximum tissue temperature reached over the treatment time. By doubling the irradiation time from the standard protocol, the maximum temperature reached increases by 10 °C to 57 °C.
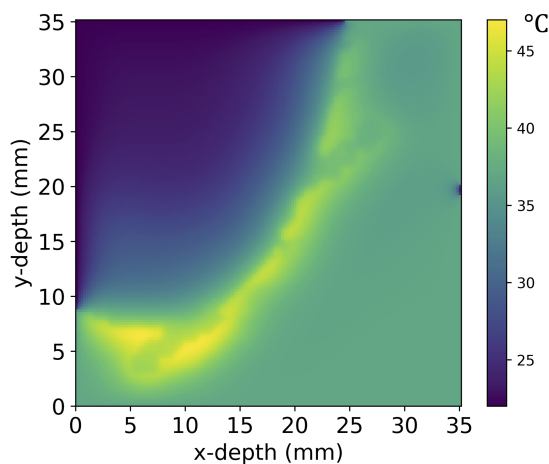
Figure 5.5: Heat map of the grid slice where the temperature reaches its maximum value of 47 °C at the end of standard protocol treatment time. The colour bar indicates tissue temperature[137].

Figure 5.7 presents the results obtained when doubling the PDT light power from 2 W to 4 W with figure 5.7a again showing the GBM cell kill and figure 5.7b presenting the maximum temperature reached over the treatment time. By doubling the treatment light power, the maximum temperature reached increased by 15 °C to 62 °C.

5.4.3   Removing fractionation breaks

The results obtained from removing the fractionation breaks from the standard protocol are displayed in figure 5.8. We can see from figure 5.8b that removing the fractionation breaks increases the maximum temperature reached by 12 °C to 59 °C.

5.4.4   Optimised protocol

Using the obtained results, optimised protocols that aimed to increase the GBM cell kill whilst keeping the maximum tissue temperature at a safe level were developed. To make sure the protocols stayed within safe limits, maximum temperature and total treatment time constraints were set to 48 °C and 30 minutes respectively. Any protocol tested that exceeded these limits was deemed unacceptable.

First a protocol was developed using the 2 W PDT light source. As the maximum tem-
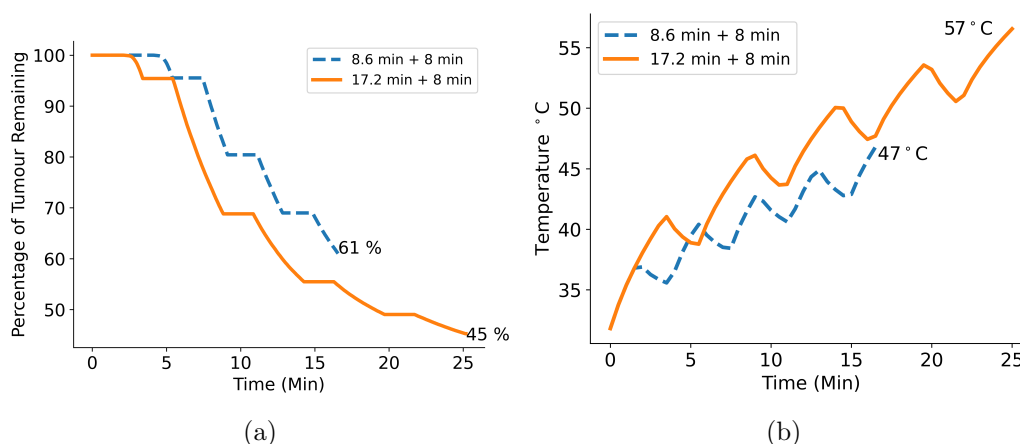
Figure 5.6: (a) Plot comparing percentage of GBM cells remaining with 2 W light source and 5 μM initial PpIX concentration for the cases of the standard treatment time (8.6 minutes + 8 minutes of fractionation breaks) (dashed) and double the treatment time (17.2 minutes plus 8 minutes of fractionation breaks) (solid). Doubling the standard treatment time results in a GBM cell kill increase of 16 %. (b) Plot comparing the maximum tissue temperature over the treatment time for the standard protocol and the protocol with double treatment time. The maximum temperature seen at the end of the double treatment time protocol is 57 °C[137].
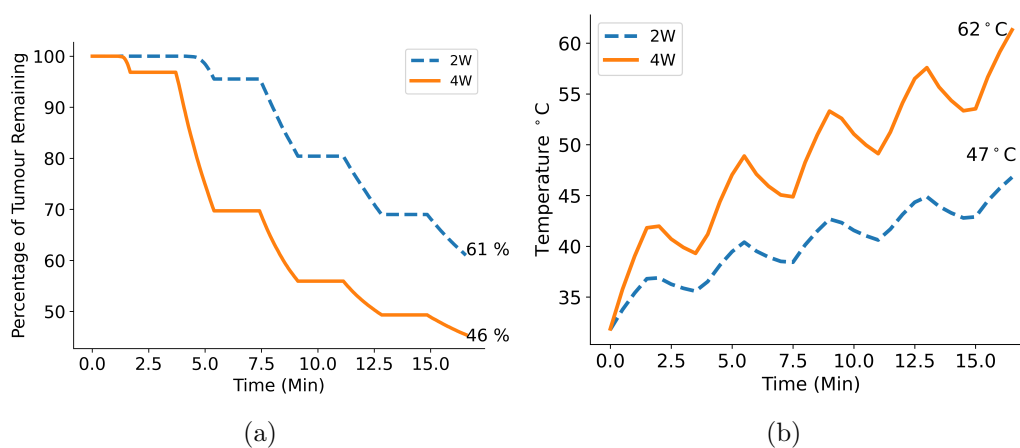
Figure 5.7: (a) Plot comparing percentage of GBM cells remaining using the standard treatment time and 5 μM initial PpIX concentration for the cases where the standard 2 W light source is used (dashed) and where a 4 W light source is used (solid). Doubling the standard treatment light power to 4 W results in a GBM cell kill increase of 15 %. (b) Plot comparing the maximum tissue temperature over the treatment time for the standard protocol and the protocol with light power. The maximum temperature seen at the end of the double light power protocol is 62 °C[137].
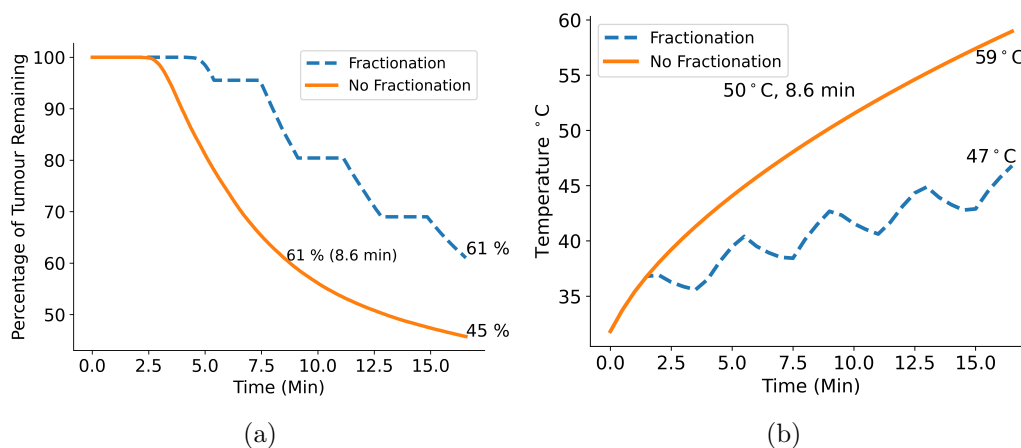
Figure 5.8: (a) Plot comparing percentage of GBM cells remaining over the standard PDT treatment time with 2 W light source and 5 μM initial PpIX concentration for the cases with standard fractionation of the PDT light source (four evenly spaced periods of two minutes where the light is switched off)(dashed) and where fractionation is neglected (solid). Using the unfractionated treatment light results in a GBM cell kill increase of 14 % at the end of the treatment time. (b) Plot comparing the maximum tissue temperature over treatment time for the standard protocol with and without light fractionation. The standard protocol achieves a maximum temperature of 47 °C. After an equivalent illumination time of 8.6 minutes, the non-fractionated treatment reaches a maximum temperature of 50 °C which increases to 59 °C after the remaining 8 minutes of treatment time[137].

(a)

(b)
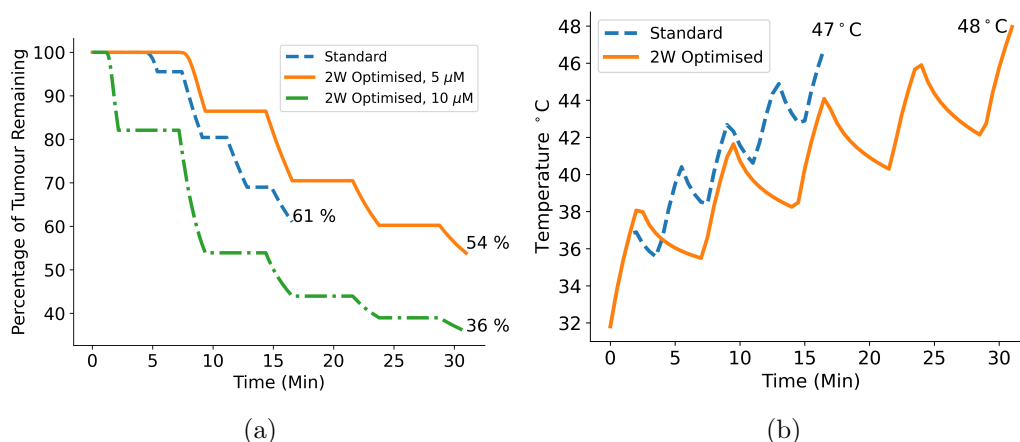
Figure 5.9: (a) Plot comparing the cell kill for the standard protocol and the optimised protocol using a 2 W light source. The optimised protocol involved using a longer treatment time of 11 minutes while extending the fractionation breaks to 5 minutes to allow sufficient tissue cooling. With the same initial concentration of PpIX (5 μM), the optimised protocol improved cell kill by 5 % which is improved by a further 18 % when an initial concentration of 10 μM is used. However, further improvement within a 30 minute time frame is limited by the maximum tissue temperature as shown in (b) where the optimised protocol has reached the damage threshold temperature of 48 °C[137].

perature obtained using the standard protocol was already very close to the maximum limit, increasing the cell kill whilst not exceeding the limit was challenging. However, by extending the total treatment time to 30 minutes and the fractionation breaks to 5 minutes each, the irradiation time could be increased to a total of 11 minutes. As shown in figure 5.9, this resulted in a cell kill increase of 5 % while keeping the maximum temperature reached to an acceptable level.

Next, a protocol using the 4 W PDT source was developed. Various fraction and rest period durations were explored using the standard 5-fraction setup, however, due to the high power of the source, a protocol could not be found that did not exceed the safety limits set. Figure 5.10 shows the maximum temperature over treatment time of a protocol with only 3 fractions and 2, 10 minute rest periods.

We can see that over each rest period, the rate at which the temperature decreases, slows down. Using this information, it was theorised that several shorter rest periods would be more efficient when cooling the tissue than one longer period of the same total duration. A protocol using the 4 W light source was developed with a shorter total irradiation time
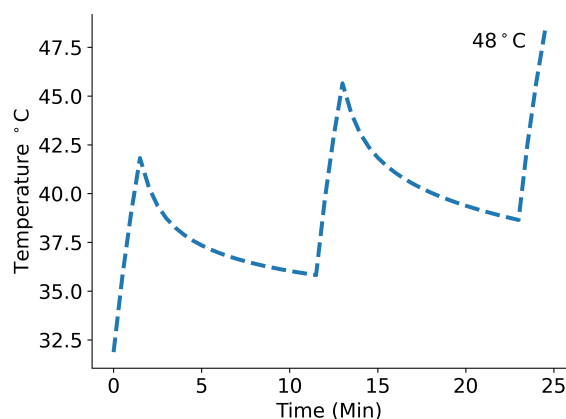
Figure 5.10: Line plot of the maximum tissue temperature reached when using a protocol with 4.5 minutes of irradiation split into three fractions separated by two 10 minute long rest periods. The rate of cooling noticeably reduces over the 10 minutes that the light is switched off during each rest period.

of 5.5 minutes, split into 10 fractions, each separated by a 2.7 minute rest period. Figure 5.11 displays the results from this protocol. We can see from figure 5.11a that the GBM cell kill is improved by 6 % compared to the standard 2 W protocol, while the maximum temperature is kept below the 48 °C maximum limit.

5.5   Discussion

5.5.1   Standard protocol

Figure 5.4 demonstrates that the INDYGO trial's protocol does not exceed the safety limit set for maximum tissue temperature of 48 °C and also manages to achieve a good level of cell kill within the relatively short time of 16.6 minutes. This result agrees with the trial results which showed no toxic effects occurring and an improvement in overall survival time[97]. Figure 5.5 shows that the level of tissue heating around the resection cavity is not even, with the maximum temperature being reached towards the bottom of the resection cavity, while the tissue around the sides is noticeably cooler. This is likely due to the light source placement within the simulation, where the simulated fibre is slightly closer to the bottom of the cavity than it is to the sides. This finding has the potential to be directly relevant to the design of future light diffusers.
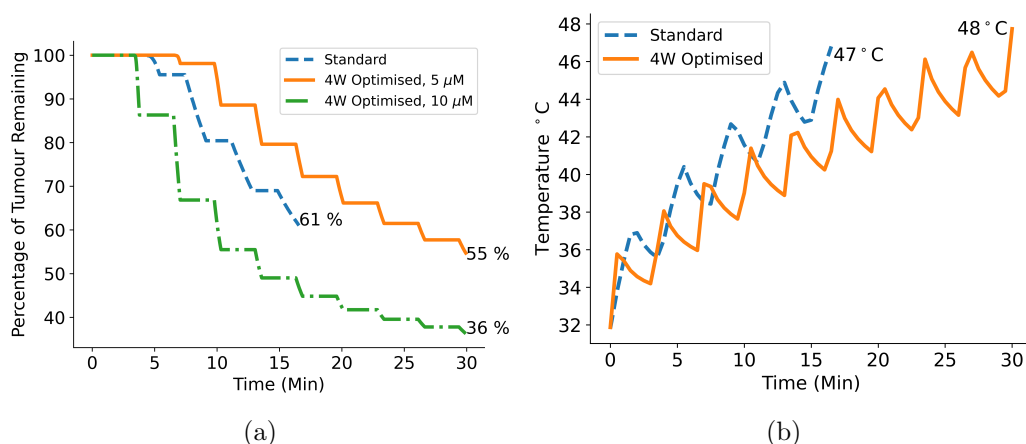
Figure 5.11: (a) Plot comparing the cell kill for the standard protocol and a protocol using a 4 W light source. The 4 W protocol involved using a shorter treatment time of 5.5 minutes split over 10 fractions instead of 5 while extending the fractionation breaks to 2.7 minutes to allow sufficient tissue cooling. With the same initial concentration of PpIX (5 μM or 10 μM), the optimised protocol achieved a 3-5 % increase in cell kill. Further improvement within a 30 minute time frame is limited by the maximum tissue temperature as shown in (b) where the 4 W protocol has reached the damage threshold temperature of 48 °C.

5.5.2 Doubling the light fluence

Although the light fluence is increased by the same amount in figures 5.6b and 5.7b, the maximum temperature achieved is different, with the protocol that doubles the light power reaching a maximum temperature 5 °C higher than that of the protocol using double irradiation time. This suggests that the relationship between delivered light fluence and tissue heating and cooling is not necessarily linear and that the individual source powers and irradiation durations will have different thermal effects.

5.5.3 Removing fractionation breaks

While the results from chapter 4 suggest that fractionating the PDT source irradiation makes very little difference to the tissue oxygen levels and resulting cell kill, figure 5.8b demonstrates why fractionation could still play an important role. By neglecting the rest periods, the maximum tissue temperature at the end of the 8.6 minute irradiation time is 2 °C over the safe temperature limit of 48 °C. Continuing to the end of the 16.6 minute protocol time, this increases to 11 °C over the safe limit without fractionation breaks. It seems therefore, that these rest periods are important for tissue cooling and allowing higher light fluences to be delivered safely, resulting in improved cell kill.

On the other hand, it has been shown that hyperthermic tissue temperatures within the range of 41 - 49 °C can actually enhance the PDT effect without harming healthy tissue[200, 201]. This is potentially related to the increase in permeability of the BBB due to warmer temperatures, allowing higher concentrations of PpIX into the brain[202]. If the treatment time of the non-fractionated protocol was set slightly below the 8.6 minute protocol time to allow the temperature to stay below 49 °C, it is possible that the higher temperature throughout the treatment time (figure 5.8b) will enhance the PDT effect. Figure 5.12b demonstrates that the non-fractionated protocol takes 7.5 minutes to reach the threshold temperature of 48 °C. Figure 5.12a shows that this treatment time results in a GBM cell kill of 35 % i.e. only 4 % less than the standard, fractionated protocol. This makes it very possible that increased temperature enhancing effects could improve the cell kill to at least match that of the standard protocols, but in less time. Juzeniene et al. suggest that cooling the tissue down after the treatment can also enhance the effect of PDT[201].

5.5.4 Optimised protocol

While the optimised protocols in figures 5.9 and 5.11 did improve cell kill by about 5% whilst keeping the tissue at a safe temperature, the large increase in the treatment time necessary to do this is unlikely to be perceived as worth the small gain in efficacy (keeping the brain exposed for these longer treatments has the potential to increase infection rate, for example). However, as noted before, the increased tissue temperature of these protocols
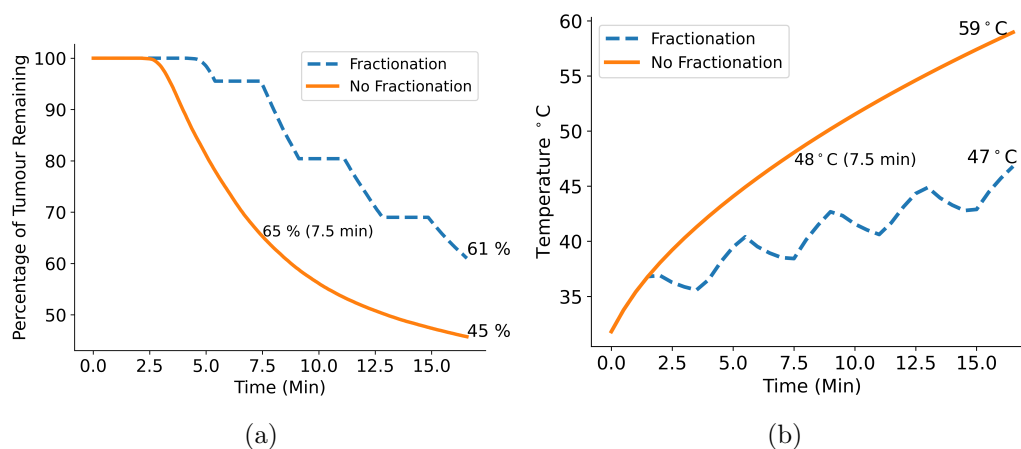
Figure 5.12: (a) Plot comparing the percentage of GBM cell kill over time resulting from the fractionated and non fractionated protocols. The plot shows that 65 % of GBM cells remain after 7.5 minutes using the non-fractionated protocol. This corresponds to the point that the 48 °C temperature safety limit is reached as shown in (b).

may improve the PDT cell kill effect more than is calculated by the simulation.

A method to improve results that may be worth considering is active tissue cooling throughout the treatment time. This could be done, for example, by using chilled intralipid solution within the balloon or by irrigating the resection cavity with chilled saline solution. This would lower tissue temperatures, allowing higher light fluences to be safely delivered. However, if the higher temperatures do help to improve results as discussed in section 5.5.3, this improvement may be reduced by the chilled saline. Saline irrigation is already a method that is used by Schipmann et al. within their clinical trial looking at intraoperative PDT for high grade gliomas[102] to reduce debris and blood clots within the resection cavity which may also help improve treatment efficacy by reducing physical obstacles for the treatment light.

Another future option that might improve results without heating the tissue too much would be to use a different photosensitiser that reacts to a wavelength that can penetrate further into brain tissue. It is possible for infiltrating GBM tumour cells to be present up to 4 cm from the resection cavity wall[104] and so any improvement in the penetration depth of the light is likely to improve treatment efficacy. Using the optical properties of brain and GBM tissue measured by Shapey et al.[170], the simulation properties were changed to those corresponding to 820 nm, where the brain matter absorption is lowest. Figure 5.13 shows that using a 820 nm source for 8.6 minutes results in a light fluence of 25 J/cm^2, 0.5
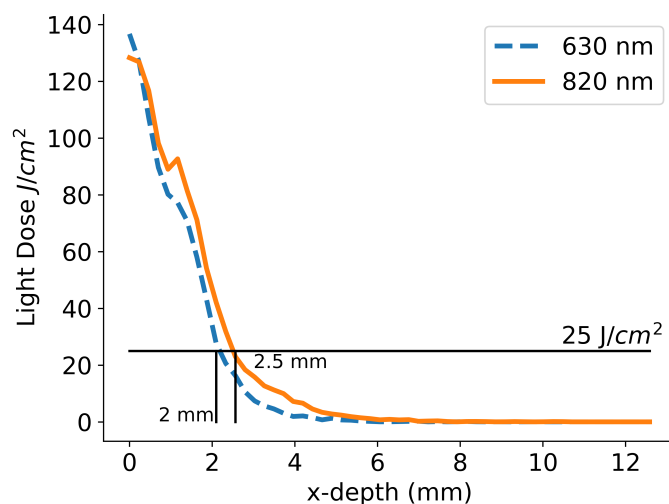
Figure 5.13: Line plot showing the difference in penetration depth into the brain model when using 635 nm and 820 nm light sources. The results show that using an 820 nm source for the 8.6 minute irradiation time, a light fluence of 25 J/cm^2 is achieved 0.5 mm deeper than when using a 635 nm source.

mm deeper into the tissue than a 635 nm source. This could result in some improvement to cell kill, assuming that the photosensitiser reacting to 820 nm is at least as efficient as PpIX in producing a phototoxic effect.

5.5.5 Simulation improvements

While the presented temperature simulation acts as a good starting point for estimating the temperature changes in the brain due to intraoperative PDT, there are some improvements that could be made to enhance the accurateness of the results.

The results show that the increase in temperature around the cavity walls is heterogeneous. It is likely that this is partially due to the heterogeneity in the optical properties but it is also clear that heterogeneity in the treatment light distribution from the balloon is also affecting results. To ensure that the results are fully realistic, more attention needs to paid to the exact placement of the optical fibre within the balloon, as well as the light distribution from the tip of the fibre to ensure they are reproducing the INDYGO trial setup. Simulating the full cavity rather than just half will also allow a full picture of the temperature distribution to be obtained.

A further improvement that could be made is to use separate thermal coefficients for white and grey matter, instead of the coefficients for average brain tissue that were used. While the values are close together[199] and unlikely affect the results too much, the result accuracy would be increased, especially in areas surrounding deeper tumours, where white matter is dominant.

5.6 Conclusion

A heat diffusion code was adapted to simulate the temperature changes during intraoperative PDT for GBM within a 3D brain model. Using the standard protocol from the INDYGO trial (chapter 4), the maximum tissue temperature reached by the end of the treatment time is 47 °C, 1 °C below the safety limit set at 48 °C. As a result, all protocols tested previously that increased the total light fluence delivered, such as doubling the treatment time and power, and removing fractionation breaks, resulted in the maximum safe temperature being exceeded.

Optimised protocols using either a 2 W or 4 W light source were developed that achieved a higher rate of cell kill while remaining within safe temperature limits. These optimised protocols improved cell kill by 5-6 % compared to the standard protocol, while the treatment time was increased by over 13 minutes. With further validation, this is a result that could provide clinical benefit, provided to protocol time increase is acceptable. It is possible that protocols that heat the tissue more, whilst staying below the maximum safe temperature, may enhance GBM cell kill due to hyperthermic effects. Overall, the standard INDYGO trial protocol seems to be the safest option, achieving a good percentage of cell kill in a short time, whilst keeping the tissue temperature at a safe level.

Chapter 6

Conclusion

This thesis has looked at applying Monte Carlo Radiative Transport techniques to model the path and interaction of light in biological tissue. The overreaching aim was to develop computational models that could be applied to contribute to clinical research.

6.1 Chapter summaries and next steps

6.1.1 Chapter 1

Chapter 1 discussed the main motivations for the thesis. Ultraviolet, visible and near infrared radiation were also introduced, focusing on their interactions with biological tissue and their medical applications. Finally, the concept of optical properties was discussed before introducing MCRT and the theory behind it.

6.1.2 Chapter 2

Chapter 2 looked at using MCRT to model the penetration depth of light into a skin model with Fitzpatrick skin photo-type I, over the wavelength range 200 nm - 1000 nm for both direct and diffuse light. The penetration depth of light for different stratum corneum thicknesses and source incident angles was also explored, as well as the lateral spread of light from a laser beam.

It is hoped that the results presented will help to increase understanding of light penetration into skin, information that is crucial for improving light based therapies and increasing the safely of light based devices such a germicidal UV lamps. The results showed that the parameters tested affect light penetration depth which highlights the importance and need for a personalised approach when planning light therapy treatments. This also highlights the potential for MCRT as a treatment planning tool and an aid for the development of new treatments. A web application was also developed to make the simulation results data

more accessible and allow the results to be used by clinicians and other researchers.

An important next step in this research would be to expand the skin model to simulate other skin photo-types. Unfortunately the majority of skin optical properties currently available in literature are based on skin that is Fitzpatrick type I and II. However, as melanin is a significant chromophore that will likely affect the penetration of light, it is imperative that its effect at different concentrations and distributions be included in these results.

6.1.3 Chapter 3

Chapter 3 focused on introducing PDT and its various applications within medicine. First the background, development and theory behind PDT was discussed. Following this, two algorithmic methods to model the dynamics of PDT were described. Each method was implemented into the MCRT code which is validated by reproducing previous PDT results. This highlights the importance of including oxygen dynamics when simulating PDT due to its importance in the treatments efficacy. It was therefore concluded that the Wang PDT algorithm that accounts for oxygen should be used in future PDT simulations.

While the PDT algorithm used is an approximation for an initial simulation, it needs further refinement before it can be used for clinical applications. A good next step would therefore be to refine the oxygen dynamic modelling. The Krogh cylinder model has limitations when modelling oxygen movement through complex networks like brain capillaries. Using a more complex representation such as a 3D vascular network model may improve the models accuracy.

Ideally the model, and each of its predicted PDT effects, should also be further validated against clinical measurements to ensure it reproduces the correct results for the specific scenario being modelled.

6.1.4 Chapter 4

The MCRT and PDT simulation was used to simulate the intraoperative PDT treatment of glioblastoma brain tumours in chapter 4. The simulation modelled the protocol of the recent INDYGO trial which used a laser-coupled inflatable balloon to deliver PDT treatment light into a glioblastoma resection cavity, with the aim of increasing the extent of tumour resection. The simulation was used to explore key treatment parameters like treatment time, light power and photosensitiser concentration and their effect on treatment efficacy.

The key findings showed that increasing the photosensitiser concentration increased tumour cell kill and increasing the light power and treatment time also resulted in some

cell kill improvement. Other findings showed that PDT related triplet oxygen depletion within brain tissues was minimal, possibly due to the fast rate of oxygen recovery, creating implications for the effectiveness of treatment light fractionation.

While this is a good first step, several assumptions and approximations were made that reduce the potential accuracy of the results. A good next step would be to further optimise the model by obtaining and using measured data that is specific to PpIX mediated PDT in glioblastoma tissue. These data could include PpIX uptake concentrations, singlet oxygen production values when using PpIX and the singlet oxygen concentration cell kill threshold in glioblastoma tissue when using PpIX.

6.1.5 Chapter 5

Finally, chapter 5 examined the thermal effects of the INDYGO trial protocol on the surrounding brain tissue. This was done by using a heat diffusion code coupled to the MCRT simulation. The effect of light power and irradiation time on the results was also explored. The model showed that while cell kill was found to increase with light power and irradiation time, the temperature of the brain tissue is also significantly increased, exceeding safe limits. Some optimised protocols were developed which use fractionation breaks to maximise cell kill whilst keeping the temperature within safe limits; however it was concluded that the current INDYGO trial protocol is likely the best balance between cell kill and overall treatment time.

A good next step for this work would be to further validate these results against measurements, ideally *in vivo*.

6.2 Conclusion

The Monte Carlo simulations developed in this thesis provide insights into both the penetration depth of light into skin and the treatment of glioblastoma brain tumours via PDT. The work produced for both of these topics has been shared with the wider research community in the form of published journal papers and conference presentations, allowing each piece of work to contribute to their respective fields. It is hoped that future work may develop on the progress made here, resulting in the continual improvement of phototherapy and ultimately enhancing outcomes for patients.

Bibliography

[1] Lara Marques, Bárbara Costa, Mariana Pereira, Abigail Silva, Joana Santos, Leonor Saldanha, Isabel Silva, Paulo Magalhães, Stephan Schmidt, and Nuno Vale. Advancing Precision Medicine: A Review of Innovative In Silico Approaches for Drug Development, Clinical Pharmacology and Personalized Healthcare. *Pharmaceutics*, 16(3):332, February 2024.

[2] Aldo Badano. In silico imaging clinical trials: cheaper, faster, better, safer, and more scalable. *Trials*, 22(1):64, 2021.

[3] José H. Correia, José A. Rodrigues, Sara Pimenta, Tao Dong, and Zhaochu Yang. Photodynamic Therapy Review: Principles, Photosensitizers, Applications, and Future Directions. *Pharmaceutics*, 13(9), 2021.

[4] I.R.M. Barnard, E. Eadie, L. McMillan, H. Moseley, T. Brown, K. Wood, and R. Dawe. Could psoralen plus ultraviolet A1 (' PUVA') work? Depth penetration achieved by phototherapy lamps. *British Journal of Dermatology*, 182(3):813–814, 2020.

[5] A. Mairani, T. T. Böhlen, A. Schiavi, T. Tessonnier, S. Molinelli, S. Brons, G. Battistoni, K. Parodi, and V. Patera. A Monte Carlo-based treatment planning tool for proton therapy. *Physics in medicine and biology*, 58(8):2471–2490, 2013.

[6] Frederic H. Fahey, Kira Grogg, and Georges El Fakhri. Use of Monte Carlo Techniques in Nuclear Medicine. *Journal of the American College of Radiology : JACR*, 15(3 Pt A):446, 2018.

[7] R. M. Valentine, K. Wood, C. T.A. Brown, S. H. Ibbotson, and H. Moseley. Monte Carlo simulations for optimal light delivery in photodynamic therapy of non-melanoma skin cancer. *Physics in Medicine & Biology*, 57(20):6327, 2012.

[8] C. L. Campbell, K. Wood, R. M. Valentine, C. T. A. Brown, and H. Moseley. Monte Carlo modelling of daylight activated photodynamic therapy. *Physics in Medicine and Biology*, 60(10):4059–4073, 2015.

[9] Tobias J. Beck, Friedrich W. Kreth, Wolfgang Beyer, Jan H. Mehrkens, Andreas Obermeier, Herbert Stepp, Walter Stummer, and Reinhold Baumgartner. Interstitial photodynamic therapy of nonresectable malignant glioma recurrences using 5-aminolevulinic acid induced protoporphyrin IX. *Lasers in Surgery and Medicine*, 39(5):386–393, 2007.

[10] Shuran Wang, Xiao Ying Dai, Shengxiang Ji, Tina Saeidi, Fynn Schwiegelshohn, Abdul-Amir Yassine, Lothar Lilge, and Vaughn Betz. Scalable and accessible personalized photodynamic therapy optimization with FullMonte and PDT-SPACE. *Journal of biomedical optics*, 27(8), 2022.

[11] Dorota Stefanicka-Wojtas and Donata Kurpas. Personalised Medicine—Implementation to the Healthcare System in Europe (Focus Group Discussions). *Journal of Personalized Medicine*, 13(3):380, 2023.

[12] Emanual Maverakis, Yoshinori Miyamura, Michael P. Bowen, Genevieve Correa, Yoko Ono, and Heidi Goodarzi. Light, Including Ultraviolet. *Journal of autoimmunity*, 34(3):J247–J257, May 2010.

[13] Ewan Eadie, Waseem Hiwar, Louise Fletcher, Emma Tidswell, Paul O'Mahoney, Manuela Buonanno, David Welch, Catherine S. Adamson, David J. Brenner, Catherine Noakes, and Kenneth Wood. Far-UVC (222 nm) efficiently inactivates an airborne pathogen in a room-sized chamber. *Scientific Reports*, 12:4373, 2022.

[14] Clysly Celine R. Ramos, Josemaria Lorenzo A. Roque, Diane B. Sarmiento, Luis Enrico G. Suarez, Janela Tanya P. Sunio, Kaezzy Ila B. Tabungar, Geraldine Susan C. Tengco, Phylis C. Rio, and Allan L. Hilario. Use of ultraviolet-C in environmental sterilization in hospitals: A systematic review on efficacy and safety. *International Journal of Health Sciences*, 14(6):52–65, 2020.

[15] John D'Orazio, Stuart Jarrett, Alexandra Amaro-Ortiz, and Timothy Scott. UV Radiation and the Skin. *International Journal of Molecular Sciences*, 14(6):12222–12248, 2013.

[16] Isla Rose Mary Barnard, Patrick Tierney, Catherine Louise Campbell, Lewis McMillan, Harry Moseley, Ewan Eadie, Christian Thomas Alcuin Brown, and Kenneth Wood. Quantifying Direct DNA Damage in the Basal Layer of Skin Exposed to UV Radiation from Sunbeds. *Photochemistry and Photobiology*, 94(5):1017–1025, 2018.

[17] Asta Juzeniene and Johan Moan. Beneficial effects of UV radiation other than via vitamin D production. *Dermato-endocrinology*, 4(2):109–117, 2012.

[18] Seok Hyun Yun and Sheldon J. J. Kwok. Light in diagnosis, therapy and surgery. *Nature biomedical engineering*, 1:0008, 2017.

[19] Linzhuang Xing, Bin Chen, Dong Li, Jun Ma, Wenjuan Wu, and Guoxiang Wang. Nd:YAG laser-induced morphology change and photothermal conversion of gold nanorods with potential application in the treatment of port-wine stain. *Lasers in Medical Science*, 32(3):629–640, April 2017.

[20] Steven L. Jacques. Optical properties of biological tissues: a review. *Physics in Medicine & Biology*, 58(11):R37, 2013.

[21] Tom Lister, Philip A. Wright, and Paul H. Chappell. Optical properties of human skin. *Journal of Biomedical Optics*, 17(9):090901, 2012.

[22] Julia L. Sandell and Timothy C. Zhu. A review of in-vivo optical properties of human tissues and its impact on PDT. *Journal of Biophotonics*, 4(11-12):773–787, 2011.

[23] T. Binzoni, T. S. Leung, A. H. Gandjbakhche, D. Rüfenacht, and D. T. Delpy. The use of the Henyey–Greenstein phase function in Monte Carlo simulations in biomedical optics. *Physics in Medicine & Biology*, 51(17):N313, 2006.

[24] Yuxuan Liang, Chuang Niu, Chen Wei, Shenghan Ren, Wenxiang Cong, and Ge Wang. Phase function estimation from a diffuse optical image via deep learning. *Physics in medicine and biology*, 67(7):10.1088/1361–6560/ac5b21, 2022.

[25] John W. Pickering, Scott A. Prahl, Niek van Wieringen, Johan F. Beek, Henricus J. C. M. Sterenborg, and Martin J. C. van Gemert. Double-integrating-sphere system for measuring the optical properties of tissue. *Applied Optics*, 32(4):399–410, 1993.

[26] Martin Hohmann, Benjamin Lengenfelder, Daniel Muhr, Moritz Späth, Maximilian Hauptkorn, Florian Klämpfl, and Michael Schmidt. Direct measurement of the scattering coefficient. *Biomedical Optics Express*, 12(1):320–335, 2020.

[27] Hua-Jiang Wei, Da Xing, Guo-Yong Wu, Ying Jin, and Huai-Min Gu. Optical properties of human normal small intestine tissue determined by Kubelka-Munk method in vitro. *World Journal of Gastroenterology*, 9(9):2068–2072, 2003.

[28] Kerry Setchfield, Alistair Gorman, A. Hamish R. W. Simpson, Michael G. Somekh, and Amanda J. Wright. Relevance and utility of the *in-vivo* and *ex-vivo* optical properties of the skin reported in the literature: a review [Invited]. *Biomedical Optics Express*, 14(7):3555–3583, 2023.

[29] K. Klier. ABSORPTION AND SCATTERING IN PLANE PARALLEL TURBID MEDIA. *J Opt Soc Am*, 62(7):882–885, 1972.

[30] Lihong Wang, Hsin-I Wu, and Barry Masters. Biomedical Optics: Principles and Imaging. *Journal of biomedical optics*, 13:049902, 2008.

[31] Gilwon Yoon, Scott A. Prahl, and Ashley J. Welch. Accuracies of the diffusion approximation and its similarity relations for laser irradiated biological media. *Applied Optics*, 28(12):2250–2255, 1989.

[32] Ronan M. Valentine, C. Tom A. Brown, Harry Moseley, Sally Ibbotson, and Kenny Wood. Monte Carlo modeling of in vivo protoporphyrin IX fluorescence and singlet oxygen production during photodynamic therapy for patients presenting with superficial basal cell carcinomas. *Journal of Biomedical Optics*, 16(4):048002, 2011.

[33] Catherine Louise Campbell. *Under the skin : Monte Carlo radiation transfer modelling of photodynamic therapy, http://hdl.handle.net/10023/9899*. PhD thesis, 2016.

[34] Elena Almaraz Luengo. A brief and understandable guide to pseudo-random number generators and specific models for security. *Statistics Surveys*, 16(none):137–181, 2022.

[35] William H. Press. *Numerical Recipes 3rd Edition: The Art of Scientific Computing*. Cambridge University Press, 2007. Google-Books-ID: 1aAOdzK3FegC.

[36] Miloš Babović and Vukota Babović. How needless are Buffon's needles? *European Journal of Physics*, 34(3):715, 2013.

[37] Robert L. Harrison. Introduction To Monte Carlo Simulation. *AIP conference proceedings*, 1204:17–21, 2010.

[38] Adrian Barbu and Song-Chun Zhu. Introduction to Monte Carlo Methods. In Adrian Barbu and Song-Chun Zhu, editors, *Monte Carlo Methods*, pages 1–17. Springer, Singapore, 2020.

[39] D W O Rogers. Fifty years of Monte Carlo simulations for medical physics. *Physics in Medicine & Biology*, 51(13):6441, 2006.

[40] Lewis McMillan, Paul O'Mahoney, Kairui Feng, Kanheng Zheng, Isla R. M. Barnard, Chunhui Li, Sally Ibbotson, Ewan Eadie, C. Tom A. Brown, and Kenneth Wood. Development of a Predictive Monte Carlo Radiative Transfer Model for Ablative Fractional Skin Lasers. *Lasers in Surgery and Medicine*, 53(5):731–740, 2021.

[41] Kenneth Wood and Ron Reynolds. A Model for the Scattered Light Contribution and Polarization of the Diffuse Hα Galactic Background. *The Astrophysical Journal*, 525(2):799–807, 1999.

[42] Louise Finlayson, Isla R.M. Barnard, Lewis McMillan, Sally H. Ibbotson, C. Tom A. Brown, Ewan Eadie, and Kenneth Wood. Depth Penetration of Light into Skin as a Function of Wavelength from 200 to 1000 nm. *Photochemistry and Photobiology*, 2021.

[43] K. Danielsen, A. O. Olsen, T. Wilsgaard, and A.-S. Furberg. Is the prevalence of psoriasis increasing? A 30-year follow-up of a population-based cohort. *The British Journal of Dermatology*, 168(6):1303–1310, 2013.

[44] Magdalena Ciażyńska, Grażyna Kamińska-Winciorek, Dariusz Lange, Bogumił Lewandowski, Adam Reich, Martyna Sławińska, Marta Pabianek, Katarzyna Szczepaniak, Adam Hankiewicz, Małgorzata Ułańska, Jan Morawiec, Maria Błasińska-Morawiec, Zbigniew Morawiec, Janusz Piekarski, Dariusz Nejc, Robert Brodowski, Anna Zaryczańska, Michał Sobjanek, Roman J. Nowicki, Witold Owczarek, Monika Słowińska, Katarzyna Wróbel, Andrzej Bieniek, Anna Woźniacka, Małgorzata Skibińska, Joanna Narbutt, Wojciech Niemczyk, Karol Ciażyński, and Aleksandra Lesiak. The incidence and clinical analysis of non-melanoma skin cancer. *Scientific Reports*, 11(1):4337, 2021.

[45] Asheesh Gupta, Gaurav K. Keshri, and Anju Yadav. Non-thermal Therapeutic Applications of Light. *Proceedings of the National Academy of Sciences India Section A - Physical Sciences*, 88(3):473–478, 2018.

[46] Ik Jun Moon, Jae Won Choi, Chang Jin Jung, Seok Hwan Kim, Eun Soo Park, and Chong Hyun Won. Efficacy and safety of a novel combined 1060-nm and 635-nm laser device for non-invasive reduction of abdominal and submental fat. *Lasers in Medical Science*, 2021.

[47] Pinar Avci, Asheesh Gupta, Magesh Sadasivam, Daniela Vecchio, Zeev Pam, Nadav Pam, and Michael R. Hamblin. Low-level laser (light) therapy (LLLT) in skin: Stimulating, healing, restoring. *Seminars in Cutaneous Medicine and Surgery*, 32(1):41–52, 2013.

[48] Omnia Hamdy and Ibrahim Abdelhalim. Diagnosing different types of skin carcinoma based on their optical properties: A Monte-Carlo implementation. *IOP Conference Series: Materials Science and Engineering*, 1046(1):012016, 2021.

[49] Michele M. Kim and Arash Darafsheh. Light Sources and Dosimetry Techniques for Photodynamic Therapy. *Photochemistry and Photobiology*, 96(2):280–294, 2020.

[50] Brian W. Pogue, Jonathan T. Elliott, Stephen C. Kanick, Scott C. Davis, Kimberley S. Samkoe, Edward V. Maytin, Stephen P. Pereira, and Tayyaba Hasan. Revisiting photodynamic therapy dosimetry: Reductionist & surrogate approaches to facilitate clinical success. *Physics in Medicine and Biology*, 61(7):R57–R89, 2016.

[51] Isla Rose Mary Barnard, Ewan Eadie, and Kenneth Wood. Further evidence that far-UVC for disinfection is unlikely to cause erythema or pre-mutagenic DNA lesions in skin. *Photodermatology, Photoimmunology & Photomedicine*, 36(6):476–477, 2020.

[52] Ewan Eadie, Paul O'Mahoney, Louise Finlayson, Isla Rose Mary Barnard, Sally Helen Ibbotson, and Kenneth Wood. Computer Modeling Indicates Dramatically Less DNA Damage from Far-UVC Krypton Chloride Lamps (222 nm) than from Sunlight Exposure. *Photochemistry and Photobiology*, 2021.

[53] Yunyao Zhang, Jingping Zhu, and Ning Zhang. Monte Carlo model of light transport in multi-layered tubular organs. In *International Conference on Optical and Photonics Engineering (icOPEN 2016)*, volume 10250, page 102500D. SPIE, 2017.

[54] P. R.J. North, J. A.B. Rosette, J. C. Suárez, and S. O. Los. A Monte Carlo radiative transfer model of satellite waveform LiDAR. *International Journal of Remote Sensing*, 31(5):1343–1358, 2010.

[55] Emmanuel Ruggiero, Silvia Alonso-De Castro, Abraha Habtemariam, and Luca Salassa. Upconverting nanoparticles for the near infrared photoactivation of transition metal complexes: New opportunities and challenges in medicinal inorganic photochemistry. *Dalton Transactions*, 45(33):13012–13020, 2016.

[56] Paul A. J. Kolarsick, Maria Ann Kolarsick, and Carolyn Goodwin. Anatomy and Physiology of the Skin. *Journal of the Dermatology Nurses' Association*, 3(4):203, 2011.

[57] Hani Yousef, Mandy Alhajj, and Sandeep Sharma. Anatomy, Skin (Integument), Epidermis. In *StatPearls*. StatPearls Publishing, Treasure Island (FL), 2023.

[58] Irena Pastar, Olivera Stojadinovic, Natalie C. Yin, Horacio Ramirez, Aron G. Nusbaum, Andrew Sawaya, Shailee B. Patel, Laiqua Khalid, Rivkah R. Isseroff, and Marjana Tomic-Canic. Epithelialization in Wound Healing: A Comprehensive Review. *Advances in Wound Care*, 3(7):445–464, 2014.

[59] H. G. Kuball, T. Höfer, and S. Kiesewalter. Chiroptical Spectroscopy, General Theory. In John C. Lindon, George E. Tranter, and David W. Koppenaal, editors, *Encyclopedia of Spectroscopy and Spectrometry (Third Edition)*, pages 217–231. Academic Press, Oxford, 2017.

[60] Daniel D. Bikle. Vitamin D and the skin: Physiology and pathophysiology. *Reviews in endocrine & metabolic disorders*, 13(1):3–19, 2012.

[61] Dipali G. Rathod, Hira Muneer, and Sadia Masood. Phototherapy. In *StatPearls [Internet]*. StatPearls Publishing, 2023.

[62] R. Vangipuram and S. R. Feldman. Ultraviolet phototherapy for cutaneous diseases: A concise review. *Oral Diseases*, 22(4):253–259, 2016.

[63] Leah Cohen, Merrick A. Brodsky, Raheel Zubair, Indermeet Kohli, Iltefat H. Hamzavi, and Mona Sadeghpour. Cutaneous interaction with visible light: What do we know? *Journal of the American Academy of Dermatology*, 89(3):560–568, 2023.

[64] P. Goon, C. Banfield, O. Bello, and N. J. Levell. Skin cancers in skin types IV–VI: Does the Fitzpatrick scale give a false sense of security? *Skin Health and Disease*, 1(3):e40, 2021.

[65] Jose A. Iglesias-Guitian, Carlos Aliaga, Adrian Jarabo, and Diego Gutierrez. A Biophysically-Based Model of the Optical Properties of Skin Aging. In *Computer Graphics Forum*, volume 34, pages 45–55, 2015.

[66] Kristian Nielsen, Lau Zhao, Jakob Stamnes, Knut Stamnes, and Johan Moan. The optics of human skin: Aspects important for human health. *Solar Radiation and Human Health*, 1:35–46, 2008.

[67] Wiel A. G. Bruls and Jan C. Van Der Leun. FORWARD SCATTERING PROPERTIES OF HUMAN EPIDERMAL LAYERS. *Photochemistry and Photobiology*, 40(2):231–242, 1984.

[68] M. J.C. Van Gemert, Steven L. Jacques, H. J.C.M. Sterenborg, and W. M. Star. Skin Optics. *IEEE Transactions on Biomedical Engineering*, 36(12):1146–1154, 1989.

[69] Mark Allen Everett, Edward Yeargers, Robert M. Sayre, and Robert L. Olson. PENETRATION OF EPIDERMIS BY ULTRAVIOLET RAYS. *Photochemistry and Photobiology*, 5(7):533–542, 1966.

[70] Igor V. Meglinski and Stephen J. Matcher. Quantitative assessment of skin layers absorption and skin reflectance spectra simulation in the visible and near-infrared spectral regions. *Physiological Measurement*, 23(4):741–753, 2002.

[71] S. L Jacques. Skin Optics. *Oregon Medical Laser Center News*, 1:1–9, 1998.

[72] A. N. Bashkatov, E. A. Genina, V. I. Kochubey, and V. V. Tuchin. Optical properties of human skin, subcutaneous and mucous tissues in the wavelength range from 400 to 2000 nm. *Journal of Physics D: Applied Physics*, 38(15):2543–2555, 2005.

[73] San Wan, R. Rox Anderson, and John A. Parrish. ANALYTICAL MODELING FOR THE OPTICAL PROPERTIES OF THE SKIN WITH IN VITRO AND IN VIVO APPLICATIONS. *Photochemistry and Photobiology*, 34(4):493–499, 1981.

[74] Aletta E. Karsten and Jacoba E. Smit. Modeling and Verification of Melanin Concentration on Human Skin Type. *Photochemistry and Photobiology*, 88(2):469–474, 2012.

[75] T. B. Fitzpatrick. The validity and practicality of sun-reactive skin types I through VI. *Archives of Dermatology*, 124(6):869–871, 1988.

[76] James Q. Del Rosso and Jacquelyn Levin. The clinical relevance of maintaining the functional integrity of the stratum corneum in both healthy and disease-affected skin. *Journal of Clinical and Aesthetic Dermatology*, 4(9):22, 2011.

[77] Jane Sandby-Møller, Thomas Poulsen, and Hans Christian Wulf. Epidermal Thickness at Different Body Sites: Relationship to Age, Gender, Pigmentation, Blood Content, Skin Type and Smoking Habits. *Acta Dermato-Venereologica*, 83(6):410–413, 2003.

[78] Elena Chirikhina, Andrey Chirikhin, Perry Xiao, Sabina Dewsbury-Ennis, and Francesco Bianconi. In Vivo Assessment of Water Content, Trans-Epidermial Water Loss and Thickness in Human Facial Skin. *Applied Sciences 2020, Vol. 10, Page 6139*, 10(17):6139, 2020.

[79] C. Mignon, D. J. Tobin, M. Zeitouny, and N. E. Uzunbajakava. Shedding light on the variability of optical skin properties: finding a path towards more accurate prediction of light propagation in human cutaneous compartments. *Biomedical Optics Express*, 9(2):852, 2018.

[80] J. Lock-Andersen, P. Therkildsen, F. De Fine Olivarius, M. Gniadecka, K. Dahlstrøm, T. Poulsen, and H. C. Wulf. Epidermal thickness, skin pigmentation and constitutive photosensitivity. *Photodermatology Photoimmunology and Photomedicine*, 13(4):153–158, 1997.

[81] Karen Waterston, Lisa Naysmith, and Jonathan L Rees. Variation in Skin Thickness May Explain Some of the Within-Person Variation in Ultraviolet Radiation-Induced Erythema at Different Body Sites. *Journal of Investigative Dermatology*, 124:1078, 2005.

[82] Merve Meinhardt, Ronald Krebs, Angelika Anders, Ulrike Heinrich, and Hagen Tronnier. Wavelength-dependent penetration depths of ultraviolet radiation in human skin. *Journal of Biomedical Optics*, 13(4):044030, 2008.

[83] Inês S. Martins, Hugo F. Silva, Ekaterina N. Lazareva, Nikita V. Chernomyrdin, Kirill I. Zaytsev, Luís M. Oliveira, and Valery V. Tuchin. Measurement of tissue optical properties in a wide spectral range: a review [Invited]. *Biomedical Optics Express*, 14(1):249–298, January 2023. Publisher: Optica Publishing Group.

[84] Liliana D'Alba and Matthew D. Shawkey. Melanosomes: Biogenesis, Properties, and Evolution of an Ancient Organelle. *Physiological Reviews*, 99(1):1–19, January 2019.

[85] Weiye Song, Lei Zhang, Steve Ness, and Ji Yi. Wavelength-dependent optical properties of melanosomes in retinal pigmented epithelium and their changes with melanin bleaching: a numerical study. *Biomedical Optics Express*, 8(9):3966, September 2017. Publisher: Optica Publishing Group.

[86] Chen S, Shu X, Yi J, Fawzi A, and Zhang Hf. Dual-band optical coherence tomography using a single supercontinuum laser source. *Journal of biomedical optics*, 21(6), June 2016. Publisher: J Biomed Opt.

[87] Caerwyn Ash, Michael Dubec, Kelvin Donne, and Tim Bashford. Effect of wavelength and beam width on penetration in light-tissue interaction using computational methods. *Lasers in Medical Science*, 32(8):1909–1918, 2017.

[88] Megan Wetzel, John Strickley, M. Tye Haeberle, and Timothy S. Brown. Depth of Invasion of Aggressive and Nonaggressive Basal Cell Carcinoma. *The Journal of Clinical and Aesthetic Dermatology*, 12(3):12–14, March 2019.

[89] Chaw-Ning Lee, Rosie Hsu, Hsuan Chen, and Tak-Wah Wong. Daylight Photodynamic Therapy: An Update. *Molecules*, 25(21):5195, November 2020.

[90] Bin Chen, Brian W. Pogue, P. Jack Hoopes, and Tayyaba Hasan. Combining vascular and cellular targeting regimens enhances the efficacy of photodynamic therapy. *International Journal of Radiation Oncology*Biology*Physics*, 61(4):1216–1226, March 2005.

[91] Yun Ou-Yang, Yaowu Zheng, and Kerry E. Mills. Photodynamic therapy for skin carcinomas: A systematic review and meta-analysis. *Frontiers in Medicine*, 10, 2023.

[92] Jeroen Meulemans, Pierre Delaere, and Vincent Vander Poorten. Photodynamic therapy in head and neck cancer: indications, outcomes, and future prospects. *Current opinion in otolaryngology & head and neck surgery*, 27(2):136–141, 2019.

[93] Tomasz Kubrak, Michał Karakuła, Marcin Czop, Aleksandra Kawczyk-Krupka, and David Aebisher. Advances in Management of Bladder Cancer—The Role of Photodynamic Therapy. *Molecules*, 27(3), 2022.

[94] Kai Wang, Boxin Yu, and Janak L. Pathak. An update in clinical utilization of photodynamic therapy for lung cancer. *Journal of Cancer*, 12(4):1154, 2021.

[95] Dorota Bartusik-Aebisher, Michał Osuchowski, Marta Adamczyk, Joanna Stopa, Grzegorz Cieślar, Aleksandra Kawczyk-Krupka, and David Aebisher. Advancements in photodynamic therapy of esophageal cancer. *Frontiers in oncology*, 12, 2022.

[96] Jiro Akimoto. Photodynamic Therapy for Malignant Brain Tumors. *Neurologia medico-chirurgica*, 56(4):151, 2016.

[97] Maximilien Vermandel, Clément Dupont, Fabienne Lecomte, Henri Arthur Leroy, Constantin Tuleasca, Serge Mordon, Constantinos G. Hadjipanayis, and Nicolas Reyns. Standardized intraoperative 5-ALA photodynamic therapy for newly diagnosed glioblastoma patients: a preliminary analysis of the INDYGO clinical trial. *Journal of neuro-oncology*, 152(3):501–514, 2021.

[98] Oscar Raab. Uber die Wirkung fluoreszierender Stoffe auf Infusorien. *Zeitschrift fur Biologie*, 39:524–546, 1900.

[99] Clément Dupont. Photodynamic therapies of high-grade gliomas: from theory to clinical perspectives,. *Physics, Université de Lille*, English, 2017.

[100] P J Muller and B C Wilson. Photodynamic therapy: cavitary photoillumination of malignant cerebral tumours using a laser coupled inflatable balloon. *The Canadian journal of neurological sciences. Le journal canadien des sciences neurologiques*, 12(4):371–3, 1985.

[101] Herbert Stepp and Walter Stummer. 5-ALA in the management of malignant glioma. *Lasers in Surgery and Medicine*, 50(5):399–419, 2018.

[102] Stephanie Schipmann, Michael Müther, Louise Stögbauer, Sebastian Zimmer, Benjamin Brokinkel, Markus Holling, Oliver Grauer, Eric Suero Molina, Nils Warneke, and Walter Stummer. Combination of ALA-induced fluorescence-guided resection and intraoperative open photodynamic therapy for recurrent glioblastoma: case series on a promising dual strategy for local tumor control. *Journal of Neurosurgery*, 134(2):426–436, 2020.

[103] Michael R. Detty, Scott L. Gibson, and Stephen J. Wagner. Current clinical and preclinical photosensitizers for use in photodynamic therapy. *Journal of Medicinal Chemistry*, 47(16):3897–3915, 2004.

[104] Samuel W. Cramer and Clark C. Chen. Photodynamic Therapy for the Treatment of Glioblastoma. *Frontiers in Surgery*, 6(81), 2020.

[105] Paul Baas, Inge van Mansom, Harm van Tinteren, Fiona A. Stewart, and Nico van Zandwijk. Effect of N-acetylcysteïne on photofrin-induced skin photosensitivity in patients. *Lasers in Surgery and Medicine*, 16(4):359–367, 1995.

[106] A. Orenstein, G. Kostenich, L. Roitman, Y. Shechtman, Y. Kopolovic, B. Ehrenberg, and Z. Malik. A comparative study of tissue distribution and photodynamic therapy selectivity of chlorin e6, Photofrin II and ALA-induced protoporphyrin IX in a colon carcinoma model. *British Journal of Cancer*, 73(8):937–944, 1996.

[107] Cherie Ann Kruger and Heidi Abrahamse. Utilisation of targeted nanoparticle photosensitiser drug delivery systems for the enhancement of photodynamic therapy. *Molecules*, 23(10), 2018.

[108] Yuan Chung Tsai, Priya Vijayaraghavan, Wen Hsuan Chiang, Hsin Hung Chen, Te I. Liu, Ming Yin Shen, Ayumu Omoto, Masao Kamimura, Kohei Soga, and Hsin Cheng Chiu. Targeted delivery of functionalized upconversion nanoparticles for externally triggered photothermal/photodynamic therapies of brain glioblastoma. *Theranostics*, 8(5):1435–1448, 2018.

[109] Brendan J. Quirk, Garth Brandal, Steven Donlon, Juan Carlos Vera, Thomas S. Mang, Andrew B. Foy, Sean M. Lew, Albert W. Girotti, Sachin Jogal, Peter S. LaViolette, Jennifer M. Connelly, and Harry T. Whelan. Photodynamic therapy (PDT) for malignant brain tumors - Where do we stand? *Photodiagnosis and Photodynamic Therapy*, 12(3):530–544, 2015.

[110] Ushasri Chilakamarthi and Lingamallu Giribabu. Photodynamic Therapy: Past, Present and Future. *Chemical Record*, 17(8):775–802, 2017.

[111] Ann Johansson, Gesa Palte, Oliver Schnell, Jörg Christian Tonn, Jochen Herms, and Herbert Stepp. 5-Aminolevulinic acid-induced protoporphyrin IX levels in tissue of human malignant brain tumors. *Photochemistry and photobiology*, 86(6):1373–1378, 2010.

[112] Schmidt Mh, Meyer Ga, Reichert Kw, Cheng J, Krouwer Hg, Ozker K, and Whelan Ht. Evaluation of photodynamic therapy near functional brain tissue in patients with recurrent brain tumors. *Journal of neuro-oncology*, 67(1-2), April 2004. Publisher: J Neurooncol.

[113] L. Alston, L. Mahieu-Williame, M. Hebert, P. Kantapareddy, D. Meyronet, D. Rousseau, J. Guyotat, and B. Montcel. Spectral complexity of 5-ALA induced PpIX fluorescence in guided surgery: a clinical study towards the discrimination of healthy tissue and margin boundaries in high and low grade gliomas. *Biomedical Optics Express*, 10(5):2478, 2019.

[114] Pietro Zeppa, Raffaele De Marco, Matteo Monticelli, Armando Massara, Andrea Bianconi, Giuseppe Di Perna, Stefania Greco Crasto, Fabio Cofano, Antonio Melcarne, Michele Maria Lanotte, and Diego Garbossa. Fluorescence-Guided Surgery in Glioblastoma: 5-ALA, SF or Both? Differences between Fluorescent Dyes in 99 Consecutive Cases. *Brain Sciences*, 12(5):555, 2022.

[115] Anthony Kim, Mathieu Roy, Farhan N. Dadani, and Brian C. Wilson. Topographic mapping of subsurface fluorescent structures in tissue using multiwavelength excitation. *Journal of Biomedical Optics*, 15(6):066026, 2010.

[116] Thomas J. Dougherty, Charles J. Gomer, Barbara W. Henderson, Giulio Jori, David Kessel, Mladen Korbelik, Johan Moan, and Qian Peng. Photodynamic Therapy. *Journal of the National Cancer Institute*, 90(12):889–905, 1998.

[117] Henry Hirschberg, Kristian Berg, and Qian Peng. Photodynamic therapy mediated immune therapy of brain tumors. *Neuroimmunology and Neuroinflammation*, 5(7):27, 2018.

[118] Karim Khan, Aakif Ullah Khan, Ghufran, Arif Khan, Moiz Khan, and Iftikhar Ahmad. Fractionated illumination improves the treatment outcomes of photodynamic therapy for high grade cutaneous leishmaniasis. *Photodiagnosis and Photodynamic Therapy*, 29:101622, 2020.

[119] Henriëtte S. de Bruijn, Adriana G. Casas, Gabriela Di Venosa, Lautato Gandara, Henricus J. C. M. Sterenborg, Alcira Batlle, and Dominic J. Robinson. Light fractionated ALA-PDT enhances therapeutic efficacy in vitro; the influence of PpIX concentration and illumination parameters. *Photochemical & Photobiological Sciences*, 12(2):241–245, 2013.

[120] J. van den Boogert, H.J. van Staveren, R.W.F. de Bruin, P.D. Siersema, and R. van Hillegersberg. Fractionated Illumination for Oesophageal ALA-PDT: Effect on Blood Flow and PpIX Formation. *Lasers in Medical Science*, 16(1):16–25, 2001.

[121] Henri-Arthur Leroy, Maximilien Vermandel, Anne-Sophie Vignion-Dewalle, Bertrand Leroux, Claude-Alain Maurage, Alain Duhamel, Serge Mordon, and Nicolas Reyns. Interstitial photodynamic therapy and glioblastoma: Light fractionation in a preclinical model. *Lasers in Surgery and Medicine*, 49(5):506–515, 2017.

[122] Ryan F. Donnelly, Paul A. McCarron, and A. David Woolfson. Drug Delivery of Aminolevulinic Acid from Topical Formulations Intended for Photodynamic Therapy¶. *Photochemistry and Photobiology*, 81(4):750–767, 2005.

[123] Xiaofen Wang, Ying Tian, Xiang Liao, Yuxia Tang, Qianqian Ni, Jing Sun, Ying Zhao, Junjie Zhang, Zhaogang Teng, and Guangming Lu. Enhancing selective photosensitizer accumulation and oxygen supply for high-efficacy photodynamic therapy toward glioma by 5-aminolevulinic acid loaded nanoplatform. *Journal of Colloid and Interface Science*, 565:483–493, 2020.

[124] Yintang Zhang, Yuanqiang Hao, Shu Chen, and Maotian Xu. Photodynamic Therapy of Cancers With Internal Light Sources: Chemiluminescence, Bioluminescence, and Cerenkov Radiation. *Frontiers in Chemistry*, 8, 2020.

[125] Jie Ji, Zhixia Fan, Feifan Zhou, Xiaojie Wang, Lei Shi, Haiyan Zhang, Peiru Wang, Degang Yang, Linglin Zhang, Wei R. Chen, and Xiuli Wang. Improvement of DC

vaccine with ALA-PDT induced immunogenic apoptotic cells for skin squamous cell carcinoma. *Oncotarget*, 6(19):17135–17146, 2015.

[126] Xu Sun, Ziyang Cao, Kuirong Mao, Chenxi Wu, Hongmei Chen, Jialiang Wang, Xin Wang, Xiuxiu Cong, Yong Li, Xianying Meng, Xianzhu Yang, Yong Guang Yang, and Tianmeng Sun. Photodynamic therapy produces enhanced efficacy of antitumor immunotherapy by simultaneously inducing intratumoral release of sorafenib. *Biomaterials*, 240, 2020.

[127] Steven L. Jacques, Rachel Joseph, and Gary Gofstein. How photobleaching affects dosimetry and fluorescence monitoring of PDT in turbid media. In *Optical Methods for Tumor Treatment and Detection: Mechanisms and Techniques in Photodynamic Therapy II*, volume 1881, pages 168–179. SPIE, June 1993.

[128] M. S. Patterson, B. C. Wilson, and R. Graff. In vivo tests of the concept of photodynamic threshold dose in normal rat liver photosensitized by aluminum chlorosulphonated phthalocyanine. *Photochemistry and Photobiology*, 51(3):343–349, March 1990.

[129] Jang Hyun Park and Heung Kyu Lee. Current Understanding of Hypoxia in Glioblastoma Multiforme and Its Response to Immunotherapy. *Cancers*, 14(5):1176, 2022.

[130] Debarati Bhanja, Hannah Wilding, Angel Baroz, Mara Trifoi, Ganesh Shenoy, Becky Slagle-Webb, Daniel Hayes, Yasaman Soudagar, James Connor, and Alireza Mansouri. Photodynamic Therapy for Glioblastoma: Illuminating the Path toward Clinical Applicability. *Cancers*, 15(13):3427, 2023.

[131] Ken Kang Hsin Wang, Jarod C. Finlay, Theresa M. Busch, Stephen M. Hahn, and Timothy C. Zhu. Explicit dosimetry for photodynamic therapy: macroscopic singlet oxygen modeling. *Journal of biophotonics*, 3(5-6):304, 2010.

[132] Daniel Goldman. Theoretical Models of Microvascular Oxygen Transport to Tissue. *Microcirculation (New York, N.Y. : 1994)*, 15(8):795–811, 2008.

[133] Timothy C. Zhu, Baochang Liu, and Rozhin Penjweini. Study of tissue oxygen supply rate in a macroscopic photodynamic therapy singlet oxygen model. *Journal of biomedical optics*, 20(3):038001, 2015.

[134] Rozhin Penjweini, Michele M. Kim, Jarod C. Finlay, and Timothy C. Zhu. Investigating the impact of oxygen concentration and blood flow variation on photodynamic therapy. *Proceedings of SPIE–the International Society for Optical Engineering*, 9694:96940L, 2016.

[135] Cameron Rink and Savita Khanna. Significance of Brain Tissue Oxygenation and the Arachidonic Acid Cascade in Stroke. *Antioxidants & Redox Signaling*, 14(10):1889, 2011.

[136] Louis Gagnon, Amy F. Smith, David A. Boas, Anna Devor, Timothy W. Secomb, and Sava Sakadžić. Modeling of Cerebral Oxygen Transport Based on In vivo Microscopic Imaging of Microvascular Network Structure, Blood Flow, and Oxygenation. *Frontiers in Computational Neuroscience*, 10, August 2016. Publisher: Frontiers.

[137] Louise Finlayson, Lewis McMillan, Szabolcs Suveges, Douglas Steele, Raluca Eftimie, Dumitru Trucu, Christian Thomas A. Brown, Ewan Eadie, Kismet Hossain-Ibrahim, and Kenneth Wood. Simulating photodynamic therapy for the treatment of glioblastoma using Monte Carlo radiative transport. *Journal of Biomedical Optics*, 29(2):025001, 2024.

[138] Cristina Birzu, Pim French, Mario Caccese, Giulia Cerretti, Ahmed Idbaih, Vittorina Zagonel, and Giuseppe Lombardi. Recurrent Glioblastoma: From Molecular Landscape to New Treatment Perspectives. *Cancers*, 13(1):1–29, 2021.

[139] Kenia A. Maldonado and Khalid Alsayouri. Physiology, Brain. In *StatPearls*. StatPearls Publishing, Treasure Island (FL), 2023.

[140] Sopiko Jimsheleishvili and Marine Dididze. Neuroanatomy, Cerebellum. In *StatPearls*. StatPearls Publishing, Treasure Island (FL), 2023.

[141] Hayden Basinger and Jeffery P. Hogg. Neuroanatomy, Brainstem. In *StatPearls*. StatPearls Publishing, Treasure Island (FL), 2023.

[142] P. A. McKinney. Brain tumours: incidence, survival, and aetiology. *Journal of Neurology, Neurosurgery & Psychiatry*, 75(suppl 2):ii12–ii17, 2004.

[143] David N Louis, Arie Perry, Pieter Wesseling, Daniel J Brat, Ian A Cree, Dominique Figarella-Branger, Cynthia Hawkins, H K Ng, Stefan M Pfister, Guido Reifenberger, Riccardo Soffietti, Andreas von Deimling, and David W Ellison. The 2021 WHO Classification of Tumors of the Central Nervous System: a summary. *Neuro-Oncology*, 23(8):1231–1251, 2021.

[144] Sumbal Rasheed, Kanwal Rehman, and Muhammad Sajid Hamid Akash. An insight into the risk factors of brain tumors and their therapeutic interventions. *Biomedicine & Pharmacotherapy*, 143:112119, 2021.

[145] Asayel A. Alruwaili and Orlando De Jesus. Meningioma. In *StatPearls*. StatPearls Publishing, Treasure Island (FL), 2023.

[146] Fassil B. Mesfin and Mohammed A. Al-Dhahir. Gliomas. In *StatPearls*. StatPearls Publishing, Treasure Island (FL), 2023.

[147] Tejaswi Kanderi and Vikas Gupta. Glioblastoma Multiforme. In *StatPearls*. StatPearls Publishing, Treasure Island (FL), 2023.

[148] Farina Hanif, Kanza Muzaffar, Kahkashan Perveen, Saima M Malhi, and Shabana U Simjee. Glioblastoma Multiforme: A Review of its Epidemiology and Pathogenesis through Clinical Presentation and Treatment. *Asian Pacific Journal of Cancer Prevention : APJCP*, 18(1):3–9, 2017.

[149] Roger Stupp, Warren P. Mason, Martin J. van den Bent, Michael Weller, Barbara Fisher, Martin J.B. Taphoorn, Karl Belanger, Alba A. Brandes, Christine Marosi, Ulrich Bogdahn, Jürgen Curschmann, Robert C. Janzer, Samuel K. Ludwin, Thierry Gorlia, Anouk Allgeier, Denis Lacombe, J. Gregory Cairncross, Elizabeth Eisenhauer, and René O. Mirimanoff. Radiotherapy plus concomitant and adjuvant temozolomide for glioblastoma. *The New England journal of medicine*, 352(10):987–996, 2005.

[150] Derek R. Johnson and Brian Patrick O'Neill. Glioblastoma survival in the United States before and during the temozolomide era. *Journal of Neuro-Oncology*, 107(2):359–364, 2012.

[151] Shideng Bao, Qiulian Wu, Roger E. McLendon, Yueling Hao, Qing Shi, Anita B. Hjelmeland, Mark W. Dewhirst, Darell D. Bigner, and Jeremy N. Rich. Glioma stem cells promote radioresistance by preferential activation of the DNA damage response. *Nature*, 444(7120):756–756, 2006.

[152] Lechner Rodríguez Aguilar, María Laura Vilchez, and Laura N. Milla Sanabria. Targeting glioblastoma stem cells: The first step of photodynamic therapy. *Photodiagnosis and Photodynamic Therapy*, 36:102585, 2021.

[153] Mariana Miretti, María Antonella González Graglia, Agustín I. Suárez, and César G. Prucca. Photodynamic therapy for glioblastoma: A light at the end of the tunnel. *Journal of Photochemistry and Photobiology*, 13:100161, 2023.

[154] Liang Rong, Ni Li, and Zhenzhen Zhang. Emerging therapies for glioblastoma: current state and future directions. *Journal of Experimental & Clinical Cancer Research 2022 41:1*, 41(1):1–18, 2022.

[155] Roger McLendon and et al. Comprehensive genomic characterization defines human glioblastoma genes and core pathways. *Nature*, 7216(455):1061–1068, 2008.

[156] Alexandre Carpentier, Michael Canney, Alexandre Vignot, Vincent Reina, Kevin Beccaria, Catherine Horodyckid, Carine Karachi, Delphine Leclercq, Cyril Lafon,

Jean Yves Chapelon, Laurent Capelle, Philippe Cornu, Marc Sanson, Khê Hoang-Xuan, Jean Yves Delattre, and Ahmed Idbaih. Clinical trial of blood-brain barrier disruption by pulsed ultrasound. *Science Translational Medicine*, 8(343):343re2–343re2, 2016.

[157] Ugur Sener, Michael W. Ruff, and Jian L. Campian. Immunotherapy in Glioblastoma: Current Approaches and Future Perspectives. *International journal of molecular sciences*, 23(13), 2022.

[158] Perria C, Capuzzo T, Cavagnaro G, Datti R, Francaviglia N, Rivano C, and Tercero VE. First attempts at the photodynamic treatment of human gliomas. *Journal of Neurosurgical Sciences*, 24(3-4):119–129, 1980.

[159] Nader Sanai and Mitchel S. Berger. Glioma extent of resection and its impact on patient outcome. *Neurosurgery*, 62(4):753–764, 2008.

[160] Walter Stummer, Jörg-Christian Tonn, Hubertus Maximilian Mehdorn, Ulf Nestler, Kea Franz, Claudia Goetz, Andrea Bink, Uwe Pichlmeier, and ALA-Glioma Study Group. Counterbalancing risks and gains from extended resections in malignant glioma surgery: a supplemental analysis from the randomized 5-aminolevulinic acid glioma resection study. Clinical article. *Journal of Neurosurgery*, 114(3):613–623, 2011.

[161] Henri Arthur Leroy, Laura Guérin, Fabienne Lecomte, Grégory Baert, Anne Sophie Vignion, Serge Mordon, and Nicolas Reyns. Is interstitial photodynamic therapy for brain tumors ready for clinical practice? A systematic review. *Photodiagnosis and Photodynamic Therapy*, 36:102492, 2021.

[162] Henri Arthur Leroy, Gregory Baert, Laura Guerin, Nadira Delhem, Serge Mordon, Nicolas Reyns, and Anne Sophie Vignion-Dewalle. Interstitial Photodynamic Therapy for Glioblastomas: A Standardized Procedure for Clinical Use. *Cancers*, 13(22), 2021.

[163] Herbert Stepp, Tobias Beck, Thomas Pongratz, Thomas Meinel, Friedrich-Wilhelm Kreth, Jorg Ch Tonn, and Walter Stummer. ALA and Malignant Glioma: Fluorescence-Guided Resection and Photodynamic Treatment. *Journal of Environmental Pathology, Toxicology and Oncology*, 26(2), 2007.

[164] Ann Johansson, Florian Faber, Gesa Kniebühler, Herbert Stepp, Ronald Sroka, Rupert Egensperger, Wolfgang Beyer, and Friedrich Wilhelm Kreth. Protoporphyrin IX fluorescence and photobleaching during interstitial photodynamic therapy of malignant gliomas for early treatment prognosis. *Lasers in Surgery and Medicine*, 45(4):225–234, 2013.

[165] Christoph Schwartz, Adrian Rühm, Jörg-Christian Tonn, Simone Kreth, and Friedrich-Wilhelm Kreth. SURG-25INTERSTITIAL PHOTODYNAMIC THERAPY OF DE-NOVO GLIOBLASTOMA MULTIFORME WHO IV. *Neuro-Oncology*, 17(Suppl 5):v219, 2015.

[166] Clément Dupont, Serge Mordon, Pascal Deleporte, Nicolas Reyns, and Maximilien Vermandel. A novel device for intraoperative photodynamic therapy dedicated to glioblastoma treatment. *Future oncology (London, England)*, 13(27):2441–2454, 2017.

[167] Clément Dupont, Maximilien Vermandel, Henri Arthur Leroy, Mathilde Quidet, Fabienne Lecomte, Nadira Delhem, Serge Mordon, and Nicolas Reyns. INtraoperative photoDYnamic Therapy for GliOblastomas (INDYGO): Study Protocol for a Phase i Clinical Trial. *Clinical Neurosurgery*, 84(6):E414–E419, 2019.

[168] Stephen J. Bagley, Shawn Kothari, Rifaquat Rahman, Eudocia Q. Lee, Gavin P. Dunn, Evanthia Galanis, Susan M. Chang, Louis Burt Nabors, Manmeet S. Ahluwalia, Roger Stupp, Minesh P. Mehta, David A. Reardon, Stuart A. Grossman, Erik P. Sulman, John H. Sampson, Simon Khagi, Michael Weller, Timothy F. Cloughesy, Patrick Y. Wen, and Mustafa Khasraw. Glioblastoma Clinical Trials: Current Landscape and Opportunities for Improvement. *Clinical cancer research : an official journal of the American Association for Cancer Research*, 28(4):594, 2022.

[169] Szabolcs Suveges, Kismet Hossain-Ibrahim, J. Douglas Steele, Raluca Eftimie, and Dumitru Trucu. Mathematical Modelling of Glioblastomas Invasion within the Brain: A 3D Multi-Scale Moving-Boundary Approach. *Mathematics 2021, Vol. 9, Page 2214*, 9(18):2214, 2021.

[170] Jonathan Shapey, Yijing Xie, Elham Nabavi, Michael Ebner, Shakeel R. Saeed, Neil Kitchen, Neil Dorward, Joan Grieve, Andrew W. McEvoy, Anna Miserocchi, Patrick Grover, Robert Bradford, Yau Mun Lim, Sebastien Ourselin, Sebastian Brandner, Zane Jaunmuktane, and Tom Vercauteren. Optical properties of human brain and tumour tissue: An ex vivo study spanning the visible range to beyond the second near-infrared window. *Journal of biophotonics*, 15(4), 2022.

[171] Clément Dupont, Gregory Baert, Serge Mordon, and Maximilien Vermandel. Parallelized Monte-Carlo dosimetry using graphics processing units to model cylindrical diffusers used in photodynamic therapy: From implementation to validation. *Photodiagnosis and Photodynamic Therapy*, 26:351–360, 2019.

[172] Rafael Garcia, Nuno Gracias, Tudor Nicosevici, Ricard Prados, Natalia Hurtos, Ricard Campos, Javier Escartin, Armagan Elibol, Ramon Hegedus, and Laszlo Neumann. Exploring the Seafloor with Underwater Robots. *Computer Vision in Vehicle Technology*, 1:75–99, 2017.

[173] A. Tran-Dinh, F. Depret, and B. Vigué. Pression tissulaire cérébrale en oxygène : pour quoi faire et pour qui ? *Annales Françaises d'Anesthésie et de Réanimation*, 31(6):e137–e143, 2012.

[174] Anika M.S. Hartz, Julia A. Schulz, Brent S. Sokola, Stephanie E. Edelmann, Andrew N. Shen, Ralf G. Rempe, Yu Zhong, Nader El Seblani, and Bjoern Bauer. Isolation of Cerebral Capillaries from Fresh Human Brain Tissue. *Journal of Visualized Experiments : JoVE*, 2018(139):57346, 2018.

[175] Mark A. Mintun, Brian N. Lundstrom, Abraham Z. Snyder, Andrei G. Vlassenko, Gordon L. Shulman, and Marcus E. Raichle. Blood flow and oxygen delivery to human brain during functional activity: Theoretical modeling and experimental data. *Proceedings of the National Academy of Sciences of the United States of America*, 98(12):6859–6864, 2001.

[176] Janish JJ. Patel. Chapter 23 : Cerebral Metabolism. In Brian Freeman and Jeffrey Berger, editors, *Anesthesiology Core Review: Part Two Advanced Exam*. McGraw Hill, 2016.

[177] N. Lopez, R. Mulet, and R. Rodríguez. Tumor reactive ringlet oxygen approach for Monte Carlo modeling of photodynamic therapy dosimetry. *Journal of photochemistry and photobiology. B, Biology*, 160:383–391, 2016.

[178] Timothy C. Zhu, Michele M. Kim, Xing Liang, Jarod C. Finlay, and Theresa M. Busch. In-vivo singlet oxygen threshold doses for PDT. *Photonics & lasers in medicine*, 4(1):59, 2015.

[179] P. J. Muller and B. C. Wilson. An update on the penetration depth of 630 nm light in normal and malignant human brain tissue in vivo. *Physics in Medicine & Biology*, 31(11):1295, 1986.

[180] I. Georgakoudi, M. G. Nichols, and T. H. Foster. The mechanism of Photofrin photobleaching and its consequences for photodynamic dosimetry. *Photochemistry and Photobiology*, 65(1):135–144, 1997.

[181] B. C. Wilson, M. S. Patterson, and L. Lilge. Implicit and explicit dosimetry in photodynamic therapy: a New paradigm. *Lasers in Medical Science*, 12(3):182–199, 1997.

[182] Jaroslava Joniová, Cyrus Kazemiraad, Emmanuel Gerelli, and Georges Wagnières. Stimulation and homogenization of the protoporphyrin IX endogenous production by photobiomodulation to increase the potency of photodynamic therapy. *Journal of Photochemistry and Photobiology B: Biology*, 225:112347, 2021.

[183] Matthew Mansi, Richard Howley, Sharayu Chandratre, and Bin Chen. Inhibition of ABCG2 transporter by lapatinib enhances 5-aminolevulinic acid-mediated protoporphyrin IX fluorescence and photodynamic therapy response in human glioma cell lines. *Biochemical pharmacology*, 200, 2022.

[184] Madina Sagatova, Oxana Semyachkina-Glushkovskaya, Edik Rafailov, Vanya Mantareva, Alexander Khorovodov, Nikita Navolokin, Olga Sindeeva, Maria Ulanova, Alexander Shirokov, Artem Gekalyuk, Sergei Sokolovski, Ekaterina Borisova, Anastasiya Bodrova, Jürgen Kurths, Natalia Shushunova, Ivan Angelov, and Ilana Agranivich. Photodynamic opening of blood-brain barrier. *Biomedical Optics Express, Vol. 8, Issue 11, pp. 5040-5048*, 8(11):5040–5048, 2017.

[185] L. Lilge and B. C. Wilson. Photodynamic therapy of intracranial tissues: a preclinical comparative study of four different photosensitizers. *Journal of Clinical Laser Medicine & Surgery*, 16(2):81–91, 1998.

[186] Maximilien Vermandel, Mathilde Quidet, Anne-Sophie Vignion-Dewalle, Henri-Arthur Leroy, Bertrand Leroux, Serge Mordon, and Nicolas Reyns. Comparison of different treatment schemes in 5-ALA interstitial photodynamic therapy for high-grade glioma in a preclinical model: An MRI study. *Photodiagnosis and Photodynamic Therapy*, 25:166–176, 2019.

[187] Lothar D. Lilge, Emily Ching, Michelle Portnoy, Andrea Molckovsky, and Brian C. Wilson. Photofrin mediated PDT in normal rat brain: assessment on apoptosis as a quantitative biological endpoint. In *Optical Methods for Tumor Treatment and Detection: Mechanisms and Techniques in Photodynamic Therapy IX*, volume 3909, pages 45–52. SPIE, 2000.

[188] L Lilge, M Portnoy, and B C Wilson. Apoptosis induced in vivo by photodynamic therapy in normal brain and intracranial tumour tissue. *British Journal of Cancer*, 83(8):1110–1117, 2000.

[189] A. B. Lumb. Why do patients need extra oxygen during a general anaesthetic? *BJA Education*, 19(2):37–39, 2019.

[190] Hongyu An, Weili Lin, Azim Celik, and Yueh Z. Lee. Quantitative measurements of cerebral metabolic rate of oxygen using MRI: a volunteer study. *NMR in biomedicine*, 14(0):441–447, 2001.

[191] Ashley A. Manzoor and Mark W. Dewhirst. Hyperthermia. In Manfred Schwab, editor, *Encyclopedia of Cancer*, pages 1462–1467. Springer, Berlin, Heidelberg, 2009.

[192] Seraphin A. Sullivan. Experimental Study of the Absorption in Distilled Water, Artificial Sea Water, and Heavy Water in the Visible Region of the Spectrum*. *JOSA*, 53(8):962–968, 1963.

[193] Huan Wang, Bonnie Wang, Kieran P. Normoyle, Kevin Jackson, Kevin Spitler, Matthew F. Sharrock, Claire M. Miller, Catherine Best, Daniel Llano, and Rose Du. Brain temperature and its fundamental properties: a review for clinical neuroscientists. *Frontiers in Neuroscience*, 8:307, 2014.

[194] Gerard C. van Rhoon, Theodoros Samaras, Pavel S. Yarmolenko, Mark W. Dewhirst, Esra Neufeld, and Niels Kuster. CEM43°C thermal dose thresholds: a potential guide for magnetic resonance radiofrequency exposure levels? *European radiology*, 23(8):2215–2227, 2013.

[195] SK Jha. Cerebral Edema and its Management. *Medical Journal, Armed Forces India*, 59(4):326–331, 2003.

[196] Connor L. West, Austin C.V. Doughty, Kaili Liu, and Wei R. Chen. Monitoring tissue temperature during photothermal therapy for cancer. *Journal of bio-X research*, 2(4):159–168, 2019.

[197] Umer Izhar, Lasitha Piyathilaka, and D. M. G. Preethichandra. Sensors for brain temperature measurement and monitoring – a review. *Neuroscience Informatics*, 2(4):100106, 2022.

[198] Lewis McMillan. *Advanced 3D Monte Carlo algorithms for biophotonic and medical applications*. Thesis, University of St Andrews, 2020.

[199] ITIS Foundation. Tissue Properties Database, Available at: https://itis.swiss/virtual-population/tissue-properties/database/ (Accessed: 19/07/2023).

[200] Henry Hirschberg, Chung-Ho Sun, Bruce J. Tromberg, Alvin T. Yeh, and Steen J. Madsen. Enhanced cytotoxic effects of 5-aminolevulinic acid-mediated photodynamic therapy by concurrent hyperthermia in glioma spheroids. *Journal of neuro-oncology*, 70(3):289–299, 2004.

[201] Asta Juzeniene, Petras Juzenas, Irena Bronshtein, Alexander Vorobey, and Johan Moan. The influence of temperature on photodynamic cell killing in vitro with 5-aminolevulinic acid. *Journal of Photochemistry and Photobiology B: Biology*, 84(2):161–166, 2006.

[202] Pavel S. Yarmolenko, Eui Jung Moon, Chelsea Landon, Ashley Manzoor, Daryl W. Hochman, Benjamin L. Viglianti, and Mark W. Dewhirst. Thresholds for thermal damage to normal tissues: An update. *International journal of hyperthermia : the official journal of European Society for Hyperthermic Oncology, North American Hyperthermia Group*, 27(4):320–343, 2011.